MULTIFRACTAL ANALYSIS AND MODELING OF TIME SERIES FOR CHARACTERIZING NONHOMOGENEOUS TURBULENCE IN SPACE PHYSICS

Neelakshi Joshi

Doctorate Thesis of the Graduate Course in Applied Computing, guided by Drs. Reinaldo Roberto Rosa e Stephan Stephany, approved in April 22, 2020.

URL of the original document:
<http://urlib.net/8JMKD3MGP3W34R/42BG88H>

MULTIFRACTAL ANALYSIS AND MODELING OF TIME SERIES FOR CHARACTERIZING NONHOMOGENEOUS TURBULENCE IN SPACE PHYSICS

Neelakshi Joshi

Doctorate Thesis of the Graduate Course in Applied Computing, guided by Drs. Reinaldo Roberto Rosa e Stephan Stephany, approved in April 22, 2020.

URL of the original document:
<http://urlib.net/8JMKD3MGP3W34R/42BG88H>

INPE

São José dos Campos

2020

INSTITUTO NACIONAL DE PESQUISAS ESPACIAIS

DEFESA FINAL DE TESE DE NEELAKSHI JOSHI
BANCA Nº 090/2020, REG 133035/2015

No dia 22 de abril de 2020, as 13 horas, na sala A da Rotunda, o(a) aluno(a) mencionado(a) acima defendeu seu trabalho final (apresentação oral seguida de arguição) perante uma Banca Examinadora, cujos membros estão listados abaixo. O(A) aluno(a) foi APROVADO(A) pela Banca Examinadora, por unanimidade, em cumprimento ao requisito exigido para obtenção do Título de Doutor em Computação Aplicada. O trabalho precisa da incorporação das correções sugeridas pela Banca Examinadora e revisão final pelo(s) orientador(es).

Título: ""MULTIFRACTAL ANALYSIS AND MODELING OF TIME SERIES FOR CHARACTERIZING NONHOMOGENEOUS TURBULENCE IN SPACE PHYSICS"

Eu, Haroldo Fraga de Campos Velho, como Presidente da Banca Examinadora, assino esta ATA em nome de todos os membros, com o consentimento dos mesmos.

Membros da banca:

Dr. Haroldo Fraga de Campos Velho - Presidente - INPE
Dr. Reinaldo Roberto Rosa - Orientador – INPE
Dr. Stephan Stephany - Orientador – INPE
Dr. Francisco Carlos Rocha Fernandes - Membro Externo – UNIVAP
Dr. Juan Alejandro Valdivia - Membro Externo – UCHILE

यस्तु संचरते देशान् तस्तु सेवेत पण्डितान् ।
तस्य विस्तारिता बुद्धिस्तैलबिन्दुरिवाम्भसि ॥

सुभाषिता मंजिरी (11.89)

The intelligence of a person who travels in different countries and associates with scholars expands, just as a drop of oil expands in water.

Dedicated to my dear husband Jayant and our lovely daughter Prajakta who become my energy and inspiration; with their support I am accomplishing my dream to be in scientific research.

Dedicatoria

ACKNOWLEDGEMENTS

ABSTRACT

Many dynamic processes in space physics can be investigated from the study of nonlinear fluctuations observed from instruments with high temporal and spectral resolution. In this thesis, it is presented, for the first time, the characterization of inhomogeneous turbulence as a possible cause of the spectral deviations found for the variables associated with the instability of the ionospheric and solar plasma. Algorithms based on formalisms for the analysis of monofractal and multifractal detrended fluctuation (DFA-MFDFA) were implemented. To validate the results obtained from the multifractal analysis, the theoretical framework for the energy cascade, based on two–scale Cantor set, a formalism known as the p model, was also implemented, tested and used. The multiplicity of intermittent behavior of plasma irregularities in the Type I solar emissions, the ionospheric F region and the E-F valley region were characterized by the MFDFA, including the respective validations through the p model spectra. The multifractal spectra are presented for the three case studies in space physics. In all three cases, the hypothesis of a non–homogeneous multiplicative cascade process for the distribution of turbulent energy is confirmed by the spectra. Also, the same analytical computational procedure has been discussed for applications in complex systems in general, considering, for example, the modelling of armed conflict time series.

Keywords: DFA. MFDFA. p model. Space plasma irregularities. Solar type I noise storm.

ANÁLISE DO MULTIFRACTAL E CASCADE P MODEL PARA CARACTERIZAR NÃO HOMOGÊNIO TURBULÊNCIA NA FÍSICA ESPACIAL

RESUMO

Muitos processos dinâmicos em física espacial podem ser investigados a partir do estudo de flutuações não-lineares observadas a partir de instrumentos com alta resolução temporal e espectral. Nesta tese, é apresentada, pela primeira vez, a caracterização de turbulência não homogênea como possível causa dos desvios espectrais encontrados para as variáveis associadas à instabilidade do plasma ionosférico e solar. Algoritmos baseados nos formalismos para a análise de flutuação destendenciada monofractal e multifractal (DFA-MFDFA) foram implementados. Para validar os resultados obtidos da análise multifractal, o framework teórico baseado no conjunto de Cantor de duas escalas, formalismo conhecido como cascata p model, também foi implementado, testado e utilizado para validar dos resultados espectrais. A multiplicidade de comportamentos intermitentes das irregularidades no plasma das emissões solares do Tipo I, da região F ionosférica e da região do vale E-F foram caracterizadas por análise de flutuação destendenciada multifractal, incluindo as respectivas validações através do espectros do p model. Os espectros multifractais são apresentados para os três casos de estudo em física espacial. Nos três casos, a hipótese de existência de processo de cascata multiplicativa não homogênea para a distribuição de energia turbulenta é confirmada pelos espectros. Também discutimos o mesmo procedimento computacional analítico para aplicações em sistemas complexos em geral, considerando, por exemplo, a modelagem de séries temporais de conflitos armados.

Palavras-chave: DFA. MFDFA. p model. irregularidades plasma espacial. emissão solar de tempestade de ruído do tipo I.

LIST OF FIGURES

LIST OF TABLES

LIST OF ABBREVIATIONS

K41   –   Kolmogorov 1941 hypothesis

PSD   –   Power Spectral Density

DFA   –   Detrended Fluctuation Analysis

MFDFA   –   Multifractal Detrended Fluctuation Analysis

ESF   –   Equatorial Spread F

CALLISTO   –   Compact Astronomical Low–cost Low–frequency Instrument
or Callisto   –   for Spectroscopy and Transportable Observatory

RNS   –   Radio Noise Storm

LIST OF SYMBOLS

ϵ –   rate of dissipation of energy

k –   wavenumber

μ –   kinematic viscosity

R –   Reynold's number

H –   Hurst exponent

α –   DFA exponent

$h(q)$ –   the generalized Hurst exponent

$\tau(q)$ –   scaling exponent

α & $f(\alpha)$ –   multifractal or singularity spectrum

$\Delta\alpha$ –   degree of multifractality or multifractal spectrum width

A –   measure of asymmetry

CONTENTS

1 INTRODUCTION

Nonlinear methods based on fractal formalism and multiplicative cascade processes have emerged as an unprecedented tool in the understanding of scaling structure of a complex system. Unfolding the nonlinear characteristics present in an empirical data, these tools have advanced our understanding of many facets of a complex system that usually had defied the conventional wisdom. The robustness of these methods has found their wide applications in numerous fields, thus undergoing continuous improvements and increased usability. In this thesis, the usability of the numerical approaches of the fractal formalism, complemented with the canonical approaches of multiplicative cascade in describing the scaling properties of the turbulent systems in space plasma are explored.

In the emerging ionosphere-space-weather paradigm, investigating the dynamical properties of ionospheric plasma irregularities using advanced computational non-linear algorithms is providing new insights into their turbulent–like nature, for instance, the evidence of energy distribution via a multiplicative cascade. Over the past few decades, observations of space plasma irregularities have provided information on their dynamics. Power spectra of plasma irregularities have shown presence of more than one spectral exponents which is attributed to interplay of different mechanisms. The theoretical model for understanding the power spectra of these regions draws a parallel with the homogeneous fluid turbulence model proposed by Kolmogorov, wherein the proper description and modeling of the statistical and scaling properties of the field of turbulent energy dissipation are vital in understanding the nature of the turbulence in these sites. However, there is a marked deviation in spectral index from the predictions of homogeneous turbulence. One of the plausible reason may the non–homogeneous turbulence. The main objective of this work is to explore this plausibility in the case of space plasma irregularities.

Objective

The central theme of this work is to address the cause behind the spectral deviation from homogeneous turbulence model and to investigate their structural properties using *fractal–multifractal* methods and *multiplicative cascade model*. The data utilized for realizing the proposed objective include: (1) *in situ* data of ionospheric plasma fluctuations obtained from two different rocket experiments carried over Brazil; and (2) spectrometer data of type I solar noise storm. Since fractal nature is ubiquitous and the tools are robust, a case study from socio–sphere, an armed conflict data is explored.

Contribution of the thesis

In this thesis, nonlinear computational algorithms viz, multifractal analysis (MFDFA) and multiplicative cascade model (p model), to analyze Space Physics data, have been implemented and following are the main contributions:

- this thesis presents the first evidence of characterizing the non–homogeneity in ionospheric and solar plasma irregularities using the fractal framework supplemented with the multiplicative cascade model.

- the work demonstrates the usability of the MFDFA in deciphering the morphology of the ionospheric F region irregularities.

- maps the multifractal measures to the density variation, showing the transition in the influence of smaller to larger fluctuations from the lower E-F valley region towards the base of F region.

- demonstrates that solar noise storm data is multifractal, intermittent in nature, and follows a non–homogeneous energy cascade process.

Organization of the thesis

The thesis is organized as follows: Chapter 2 gives an overview of the ionosphere and turbulence in the context of Kolmogorov homogeneous turbulence spectrum. Chapter 3 describes the methods used, viz., (1) detrended fluctuation analysis (DFA) and its implementation and the concept of crossover is explained; and its multifractal variant (2) multifractal detrended fluctuation analysis (MFDFA), along with its implementation, followed by a description on how to understand the results is presented. Chapter 4 describes some of the methods of multiplicative cascade model and their implementation. Among them, the p model is used in this analysis. Chapter 5 presents application of the DFA on *in situ* ionospheric data; and of the MFDFA on *in situ* ionospheric data and type I solar noise storm data. Also non-physical application of $p$model is presented. Chapter 6 summarizes important results and provide insight into the future work.

Appendix A presents time complexity and flowcharts for the DFA, MFDFA and p model. Also includes the error calculation. Appendix B includes the DFA result on ionospheric time series. Annexes presents two articles published in peer reviewed journals — *Advances in Space Research* describing the results of the DFA of iono-

spheric data, and *Annales Geophysicae* describing the multifractal characterization of ionospheric plasma irregularities.

2 REVIEW: SPACE PLASMA IRREGULARITIES

This chapter provides a brief review on the equatorial ionospheric irregularities studies and type I solar noise storm. Kolmogorov energy spectrum is introduced in the section 2.3. Chapter concludes with presenting problem addressed in this thesis.

2.1 Ionosphere studies

Ionosphere is a region in the Earth's atmosphere where photoionization due to solar radiation and high energy particles result in formation of a plasma. Free electrons and ions in the plasma undergo recombination, diffusion and transport processes due to electric and magnetic fields, and neutral winds. Layers in the ionosphere are characterized by the number density of plasma (KELLEY, 2009). Maximum plasma density region is referred to as a F layer and attains peak value near noon as photoionization is dominant during the day time. At night time, depending on the ionospheric region and altitude, plasma density drops up to two orders of magnitude. Ionospheric plasma densities show diurnal, seasonal variations and also vary with solar and geomagnetic activity.

An interesting feature of the equatorial low latitude ionosphere is the generation and spatio–temporal evolution of plasma irregularities that refer to an enhancement or depletion in the densities. Various rocket experiments and numerical simulations have been performed and contributed to our understanding of the generation and development of ionospheric irregularities. Post–sunset ionospheric irregularities in the equatorial F region were first observed by Booker and Wells (1938) using ionosondes. This phenomenon is known as equatorial spread F (ESF). During ESF, the equatorial ionosphere becomes unstable and it is attributed to the Rayleigh–Taylor instability where large scale (upto tens of km) plasma 'bubbles' can develop and rise to high altitudes (1000 km or greater at times) (KELLEY, 2009; HYSELL et al., 1999; HYSELL, 2002).

Costa and Kelley (1978) showed that the Rayleigh–Taylor instability that initiates in the bottomside equatorial F region can nonlinearly develop very sharp gradients leading to the formation of steepened structures responsible for the power–law spectra observed by a rocket experiment in Natal, Brazil. Shock waves were observed in the numerical simulation performed by Zargham and Seyler (1987) of the generalized Rayleigh–Taylor instability at the bottomside and topside F region equatorial ionosphere, which was confirmed by rocket and satellite *in situ* data reported by Kelley et al. (1987). Hysell et al. (1994a), Hysell et al. (1994b) proposed a model

of plasma steepening, evolving from plasma advection that occurs on the vertical leading edges of plasma depletion wedges, to interpret shock waves detected in the equatorial ionosphere by rockets launched from Kwajalein Atoll, Republic of the Marshall Islands. Jahn and LaBelle (1998) measured shock–like structures characterized by the density waveforms at the bottomside and topside F region of the equatorial ionosphere in a rocket experiment in Alcântara, Brazil.

Figure 2.1 presents a schematic of a rocket experiment carried out in the ionosphere.

Figure 2.1 - Schematic of a rocket experiment carried out in the ionosphere. The rocket is shown to pass through the irregularities of various scales. Please note, bubbles are not to scale.
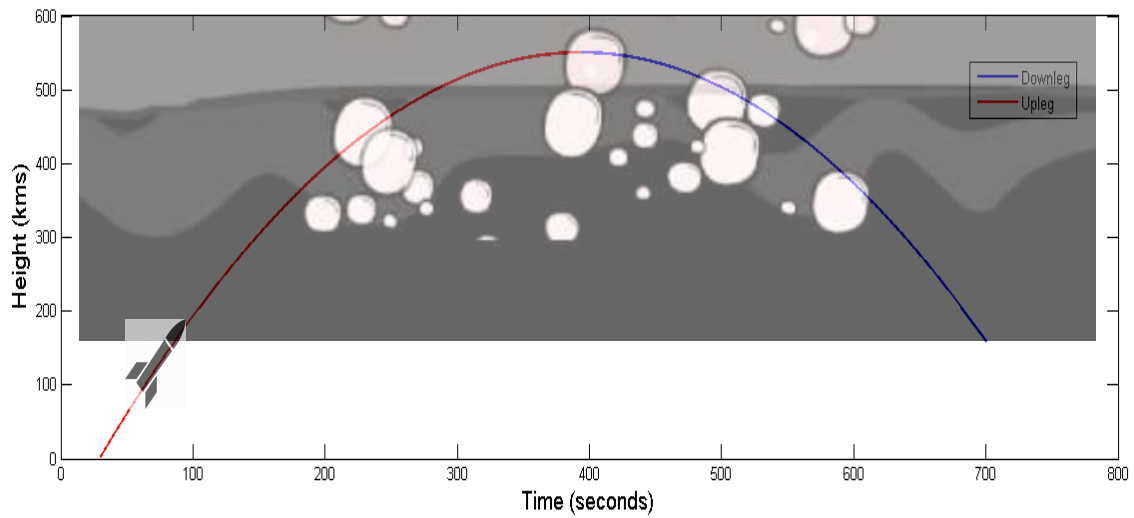
Source: produced by author.

The E-F valley (hereafter, valley) region is located between the top of the E region and the base of F region. The valley region, specifically the equatorial ones, hosts a variety of plasma irregularities both during the day, the so–called 150 km echoes (KUDEKI; FAWCETT, 1993; RODRIGUES et al., 2011), and at dusk-nighttime (CHAU; HYSELL, 2004). This region is still a less explored area of research compared to the F region given the technical limitations in observing it. It can be studied by using powerful incoherent and coherent scatter radar and *in situ* experiments. The first observation of valley region dates to 1950s when using rocket experiment, Jackson (1954), Jackson and Seddon (1958) recorded the electron density depletion in be-

tween the ionospheric E and F regions. Since then numerous radar and rocket based experiments were performed and it was established that the valley region electron density profile is regulated by solar and geomagnetic activities and show diurnal variations (WAKAI; SAWADA, 1964; WAKAI, 1967; MAEDA, 1969). Various studies have been reported on the correlation between the valley region irregularities and the equatorial plasma instabilities in the F region:

- Radar observations revealed that (i) the valley region irregularities are often found when the ESF occurred after the sunset and that their spatial structures and temporal variations have resemblance with the ESF, and (ii) the valley region irregularities are a result of the coupling between the unstable equatorial F region and the underlying low latitude valley and the E region (VICKREY; KELLEY, 1982; VICKREY et al., 1984; PATRA, 2008; YOKOYAMA et al., 2005; LI et al., 2011; KHERANI et al., 2012).

- Studies based on in situ data found that electric field and gravity waves may play a key role in the generation of these structures (in the valley regions) and that the structures are produced by the generalized Rayleigh–Taylor instability mechanism at the base of the F region (VICKREY et al., 1984; PRAKASH, 1999; SINHA et al., 1999; MURALIKRISHNA et al., 2003; ODRIOZOLA et al., 2017). Odriozola et al. (2017) reported the presence of wave–like structures in valley region based on a rocket experiment carried over Brazil.

- Xie et al. (2018) presented correlation between valley irregularities and the ESF by carrying statistical study based on very high frequency radar observations.

A conventional method in analyzing plasma irregularities has been the power spectral density (PSD) analysis (DYSON et al., 1974; KELLEY et al., 1982; KELLEY; HYSELL, 1991; KELLEY et al., 2009; PÉCSELI, 2015). A common feature observed in the PSD analysis of irregularities in the valley and F region is the presence of more than one slope which is attributed to interplay of different mechanisms. The reported PSD indices of electron density fluctuations from rocket experiments from different sites found to vary between -1.1 to -5, and some of them are listed in Table 2 in Neelakshi et al. (2019) and indices for electric field fluctuations are listed in Table 1 in Fornari et al. (2016). Owing to their irregular nature, the behavior of these structures can be described in analogy to fluid turbulence model and information regarding generation mechanism may be obtained (KINTNER; SEYLER, 1985).

2.2 Type I solar noise storm

Solar plasma from the photosphere to the outer heliosphere is in the fully developed turbulence state. It is an exquisite example of nonlinear dynamical dissipative system where the energy dissipation field is highly non–homogeneous, intermittent and follows a power law (ABRAMENKO; YURCHYSHYN, 2010).

The radio emission provide information on shocks, energetic electrons and their acceleration and these emissions show distinct spectrum and temporal behavior, based on which Wild and McCready (1950) categorized these emissions in different types (BENZ et al., 2005; BENZ et al., 2009).

These different types of solar emissions have been studied and found to be highly non–homogeneous, intermittent and following a power law. For example, Rosa et al. (2008) characterized decimetric solar radio burst variability pattern as intermittent and by applying gradient pattern analysis suggested that these bursts may be characterized as strong MHD turbulences. Veronese et al. (2011) characterized solar radio burst evolution, associated with X–class flares, using DFA. Cintra (2018) has applied gradient pattern analysis (GPA) on the type I noise storm registered on July 30, 2011 and concluded that plasma dynamics might be the underlying mechanism for this noise storm.

Among different types of solar emissions, type I bursts compose of a continuum and burst components of short duration, $0.1 - 3$ s and generally, range between $100 - -400$ MHz. Type I noise storm or radio noise storm (RNS) is the first astronomical event recorded at metric wavelengths comprising of thousands of type I bursts that associates with non–thermal solar radio emissions and can last for several hours to days.

Various studies have proposed the dynamic process and corresponding emission mechanism but it still remain elusive. RNS are strongly correlated with sunspots and has a good correlation with the magnetic activities and can last for several hours to days (KAI et al., 1985; SPICER et al., 1982). This long duration is the main characteristic that distinguish noise storm from other types of solar radio emission (KAI et al., 1985).

Spicer et al. (1982) suggested that RNS are driven by newly emerging magnetic flux. Sodré et al. (2015) studied morphological characteristics of 255 chains of RNS recorded by e-Callisto during 30 July to 9 August 2011 and figured out the physical

parameters for the event. Sodré et al. (2019) analyzed RNS recorded on August 12, 2012 using magnetic power spectra. Authors found that type I emission is probably the plasma emission and also shown that the source is the reorganization of the magnetic field of the active region. RNS are observed during quite times hence, these are associated to a non–flare event but are also observed in active regions hence, these are associated with coronal mass ejections (CMEs), flares and eruptive prominence, groups of sunspots and intense magnetic field (LI et al., 2017).

Li et al. (2017) have done a combined analysis of extreme ultraviolet (EUV), radio and photospheric magnetic field data of type I noise storm occurred on July 30, 2011. Authors identify a good correlation between the radio bursts and the co–spatial EUV and magnetic activities and agree to the proposal of Bentley et al. (2000) that the observed type I noise storm and the EUV brightening activities are the consequence of small–scale magnetic reconnection driven by multiple moving magnetic features (MMFs). Type I storm are often initiated (or driven) by the emergence of new magnetic structures in regions with pre–existing coronal magnetic fields and each burst may be accounted to an acceleration of suprathermal electrons. (SODRÉ et al., 2015).

2.3 Kolmogorov energy spectrum

Space plasma irregularities embed interactions of diverse scale lengths. This nonlinear environment has been a natural testing ground for validating theories of fluid turbulence. However, the natural environment is too complex for a direct application of the Kolmogorov (cascade) theory (K41). Kintner and Seyler (1985) argue that when a system exhibits scale invariance, i.e., follows a power law over few order of wavenumbers then such a system can be modeled by applying K41 theory to explore its scaling properties. Basic assumptions underlying K41 theory are (i) a homogeneous and isotropic turbulence, (ii) nonlinear interactions in the inertial range being independent of the energy entering and leaving the system, and (iii) constant rate of energy cascade through localized nonlinear interactions. These assumptions are prerequisites for scale invariance and observed for very large Reynolds numbers $R \equiv uL/\mu$ where u is characteristic velocity of the flow, L is the characteristic length and μ is the kinematic viscosity. In the Fourier space, $R \equiv u/\mu k$, where k is the wavenumber. In the inertial range, where viscosity is negligible, energy $(|u(k)|^2)$ is conserved. When $(|u(k)|^2)$ is conserved locally, the rate of cascade of energy, ϵ, is constant. Therefore, the energy power spectrum in the inertial range is determined

on dimensional basis using

$$E(k) = 4\pi k^2 < |u(k)|^2 > \tag{2.1}$$

up to a universal dimensionless constant, C, called Kolmogorov constant, yielding the final form (FRISCH, 1995; POPE, 2000)

$$E(k) = C\epsilon^{2/3}k^{-5/3}. \tag{2.2}$$

The Kolmogorov $-5/3$ spectrum result though applicable only in the inertial range, it is so intuitive and universal that various studies reported an agreement with it (FRISCH, 1995; BURLAGA, 1991; MENEVEAU; SREENIVASAN, 1991). Figure 2.2 presents schematic diagram of Richardson's energy cascade model for turbulence. A model starts with large eddies of energy ϵ. Larger eddies break down into smaller eddies carrying a fraction of energy recursively but conserving the total energy until it reaches the length where dissipation starts. Richardson's energy cascade process is the basis for the celebrated Kolmogorov's turbulent energy spectrum. The energy cascade begins with the kinetic energy entering the turbulent medium at the largest scales of motion, which is then transferred, conserving the energy, to smaller and smaller scales until viscous forces come into play dissipating the energy. Kolmogorov quantified the smallest scales at which dissipation occurs.

Figure 2.2 - Richardson's energy cascade model for turbulence.
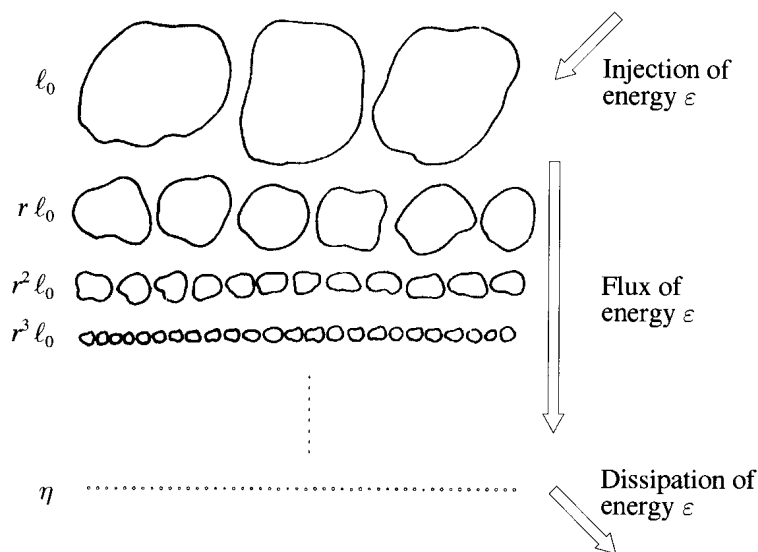
Source: Frisch (1995).

2.4 Spectral exponents and K41 spectrum

Energy dissipation is found to be an underlying process for the occurrence of electron density or electric field fluctuations in ionospheric plasma irregularities (JAHN; LABELLE, 1998; KELLEY; HYSELL, 1991). Various different approaches had been explored to understand nonlinear characteristics, self–affine nature and intermittency in ionospheric irregularities, like structure function analysis (DYRUD et al., 2008; SPICHER et al., 2015), fractal and multifractal analysis (WERNIK et al., 2003; ALIMOV et al., 2008; BOLZAN et al., 2013; TANNA; PATHAK, 2014; MIRIYALA et al., 2015; CHANDRASEKHAR et al., 2016; FORNARI et al., 2016; SIVAVARAPRASAD et al., 2018; NEELAKSHI et al., 2019), and multispectral optical imaging (CHIAN et al., 2018). Structure function analysis performed on ionospheric high latitude *in situ* data have revealed the intermittent nature of ionospheric irregularities owing to the large deviations from the K41 universal power law index proposed for neutral fluid turbulence (SPICHER et al., 2015).

Earlier solar studies quantified scaling index as a potential parameter for forecasting solar flares. Their PSD indices are found to be different than the PSD index for Kolmogorov's homogeneous turbulence, $-5/3$, and indicated the energy transfer possibility from small to large structures, as possible responsible mechanism for maintaining the long-term emissions of the storm (ABRAMENKO; YURCHYSHYN, 2010; SEN, 2007; MCATEER et al., 2010; VERONESE et al., 2011; SODRÉ et al., 2015). Also, the energy cascading process is evident in the solar and interplanetary environment as well as in the laboratory using Kolmogorov's formalism as the basis (BURLAGA, 1991; GRAUER et al., 1994; CARBONE et al., 1995; ABRAMENKO et al., 2002; BURLAGA et al., 2003; MACEK, 2007; ABRAMENKO; YURCHYSHYN, 2010; WAWRZASZEK; MACEK, 2010; CHIAN; MUÑOZ, 2011; MIRANDA et al., 2013; WAWRZASZEK et al., 2019).

In all the above mentioned studies, the main feature which gets highlighted is that the power spectra point to large deviations from the homogeneous turbulence described by the Kolmogorov spectrum ($-5/3$). Also, higher order statistics like structure function analysis confirmed the deviation from the Kolmogorov spectrum, thus affirming the non–homogeneity and intermittency in space plasma irregularities. Fornari et al. (2016) has shown that a wide variation in spectral indices is neither due to a limitation of any statistical method nor a limitation imposed by the quality of the data when analyzed by statistical techniques that depend on samples with many measurement points to guarantee robust spectra in the logarithmic domain. Once ruled out that the large spectral variation observed could be due to

11

the low statistical data quality, what other reasons could be raised? Some of them are the following: (i) presence of more than one slope value due to the role of the magnetic field for magnetohydrodynamic turbulence; (ii) dimensional nature of the ionospheric turbulence (2D or 3D), since rocket experiments are 2D tracers in a 3D environment and, each experiment, in general, presents measurements of a particular plane depending on where it was launched; (iii) the turbulent process does not follow a homogeneous cascade of the energy distribution between the scales involved in the dissipative process.

In this thesis, the third possibility is explored namely, "is non–homogeneity, which can be characterized by multifractal spectra, the cause for the large deviations from the universality class?" To answer this question, the monofractal and multifractal detrended fluctuation analysis (DFA & MFDFA) along with multiplicative cascade model (p model) are implemented on the space plasma irregularity data.

3 METHODS: DFA AND MFDFA

The word fractal is based on the Latin adjective fractus, which means irregular and fragmented. The term fractal was coined by Mandelbrot for the geometric shape (like rocky coastline, clouds) that can not be well described by Euclidean geometry and is a replica of itself at smaller scales. In other words, fractal is self–similar and is characterized by a single fractal dimension. Mandelbrot's central idea behind fractal is that the size of an object can be defined by its scales using a power law relation, rather than by its shape (MANDELBROT, 1998; MALAMUD; TURCOTTE, 1999; KANTELHARDT, 2009). Mandelbrot demonstrated the ubiquitous nature of fractals and quantified its roughness with fractal geometry.

Self–similar fractal is isotropic; i.e., its scaling is identical in all directions. Fractal can be less strict self similar, that is, statistically self–similar known as self–affine fractal with anisotropic scaling (e.g., fern leaf). When the behavior of a quantity $F(s)$ like, fluctuations, spectral power etc., varies as the power H of some parameter s like, time, frequency, it is said to be scale–invariant and follows a power law relation expressed as $F(s) \approx s^H$ (MANDELBROT, 1998; MALAMUD; TURCOTTE, 1999; EKE et al., 2002; KANTELHARDT, 2009). In self–affine fractal, the parameter s is rescaled by a factor a and the relation is expressed as $F(s) \approx a^H F(as)$. The power exponent H is known as the Hurst exponent and it infers the correlation within the quantity. On a log–log scale, self–similar fractal lie along the regression slope while self–affine fractal is scattered around it (EKE et al., 2002).

Fractal analysis of a time series gives the scaling of fluctuations with time and is described by the power exponent H. Knowing H, one can classify time series and gain some insight into its dynamics.

3.1 Detrended fluctuation analysis

Various methods exist to perform fractal analysis. Some of them include box counting method, moving average method, autocorrelation analysis, rescaled range analysis, standard fluctuation analysis, detrending moving average, backward detrending moving average, detrended fluctuation analysis. Among these methods, detrended fluctuation analysis (DFA) (PENG et al., 1994) can handle nonstationary and highly heterogeneous data to find long–range correlation. Various authors have compared several fractal methods and their variants in time domain (e.g., DFA, scaled windowed variance method (SWV)) and frequency domain (e.g., spectral and autocorrelation analysis), and also, proposed new methods or variants (EKE et al., 2002;

DELIGNIÉRES et al., 2005; SHAO et al., 2012; HÖLL et al., 2019; SIKORA et al., 2020; HARTMANN et al., 2013; PILGRIM; TAYLOR, 2018).

- Deligniéres et al. (2006) analyzed short time series of fractional Gaussian noise and fractional Brownian motion with various fractal methods and the DFA is found to be robust to analyze fractional Gaussian noise.

- Hartmann et al. (2013) chose the DFA over its variant based on efficient optimization of the resources. Authors developed a real–time DFA method to meet fast processing demand. The real–time DFA can process signal at real-time and does not need entire series in the starting of the analysis.

- Recently Höll et al. (2019) studied two different fractal methods and observed that the DFA handle statistical properties of large time lags data efficiently and authors suggested to consider weighting kernel with mean-squared displacement calculation while obtaining the fluctuation function.

- Sikora et al. (2020) studied probabilistic properties of the DFA for Gaussian process.

- Shao et al. (2012) compared various fractal variant analyses to determine the Hurst exponent from time series and found the DFA as one of the preferable method.

- Pilgrim and Taylor (2018) discuss the inherent challenges in quantifying fractality from the data set.

- Souza and Assireu (2016) implemented 2-d DFA to characterize $1/f$ noise and shown the corresponding equivalence relation with the power spectral index.

3.1.1 Features of DFA

Among several algorithms of fractal analysis, detrended fluctuation analysis (DFA) proposed by Peng et al. (1994) has been a proven method in finding power law correlation and monofractal scaling in noisy, nonstationary data. Peng et al. (1994) used the DFA to remove nonstationary trends and to detect long–range correlations in DNA sequences.

The robustness of DFA can be attributed to some of its interesting features. For instance,

- Coronado and Carpena (CORONADO; CARPENA, 2005) investigated the influence of the length of a time series in quantifying the correlation behavior using techniques like autocorrelation analysis, Hurst exponent, and DFA. The comparison study revealed that the DFA is practically unaffected by the length of time series, contrary to that observed from the results of Hurst analysis or autocorrelation analysis.

- Another interesting feature has been reported by Chen et al. (CHEN et al., 2002) who altered time series by excluding parts of it, stitching the rest and subjecting it to the DFA. The study revealed that even with the removal of 50% of the time series, the scaling behavior of positively correlated signals is unaltered, implying that time series need not be continuous.

- Heneghan and McDarby (HENEGHAN; MCDARBY, 2000) established an equivalence relation between the PSD exponent, β, and the DFA exponent, α, given by

$$\beta \equiv 2\alpha - 1 \tag{3.1}$$

- Kiyono (KIYONO, 2015) showed that this relationship is valid for the higher order DFA subject to the constraint $0 < \alpha < m + 1$, where m is the order of detrending polynomial in the DFA.

3.1.2 Applications of DFA

The DFA is widely used in many branches of science, like medicine, physics, finance and social sciences, to understand the complexity of systems through its scaling exponent that characterizes fractal dynamics of the system (KANTELHARDT, 2009). Few applications are listed below.

- The DFA is found to be useful to reveal variations in genetic, neuronal systems and physiological signals. Different scaling behavior allow to distinguish normal and abnormal development. (EKE et al., 2000; EKE et al., 2002; YAMAMOTO et al., 2010; EKE et al., 2012; HARDSTONE et al., 2012).

- Veronese et al. (2011) presented the first study of solar radio burst using the DFA. Santhanam et al. (2006) explored self–affine nature of quantum spectrum using the DFA.

- Saouma et al. (1990) demonstrated that fracture surfaces of concrete are fractals. Parga et al. (2016) explored the problem of computing a minimal

separating automaton for regular languages using the DFA.

- Grech and Mazur (2004) applied the DFA to study volatility of the stock market. Liu et al. (1997) analyzed the S&P500 financial index over 13 years period using the DFA and found crossover with two different correlations. Ding et al. (1993) studied long memory property of stock market returns with the DFA.

- In linguistics Berners-Lee and Kagal (2008) explored langauge structures with the DFA. In arts, fractality and scaling properties of luminance pattern is analyzed using the DFA (ALVAREZ-RAMIREZ et al., 2008).

In this thesis the DFA method is used for the analysis.

3.1.3 Implementation of DFA

Let x be a finite one–dimensional series with a length N and mean $\bar{x}$. Compute the profile $Y(i)$ by taking the cumulative sum of the mean subtracted time series.

$$Y(i) \equiv \sum_{k=1}^{i} (x_k - \bar{x}), \quad i = 1, 2, ..., N. \tag{3.2}$$

The profile $Y(i)$ is divided into N_s non–overlapping and equidistant segments v, of s elements, referred to as scales. The length of the series may not necessarily be an integral multiple of the scales. In such a case, to account for the left out part, the same procedure is repeated in the reverse direction. As a result, a total of $2N_s$ segments are obtained.

The segments are detrended using linear least squares. A polynomial fit $y_v(i)$ is obtained on a segment v. The variance is calculated over all segments.

$$F^2(s, v) = \frac{1}{s} \sum_{i=1}^{s} [Y[(v-1)s + i] - y_v(i)]^2 \tag{3.3}$$

for each segment v, $v = 1, 2, ..., N_s$ and

$$F^2(s, v) = \frac{1}{s} \sum_{i=1}^{s} [Y[N - (v - N_s)s + i] - y_v(i)]^2 \tag{3.4}$$

for each segment v, $v = N_s + 1, ..., 2N_s$.

Detrending the segments with different order (m) of polynomial removes trends

of the corresponding orders. For example, second order polynomial fit removes quadratic trend, third order polynomial fit removes the cubic trend, etc., present in the segments. Depending on the polynomial order used in detrending procedure, corresponding DFA method is known as DFA1, DFA2, DFA3 and so on.

Finally, compute the fluctuation profile by taking the average over all segments.

$$F(s) = \sqrt{\frac{1}{2N_s} \sum_{v=1}^{2N_s} [F^2(s, v)]}. \tag{3.5}$$

Plot the fluctuation function profile on a log–log scale, and a linear fit to it yields the DFA exponent, α.

$$F(s) \propto s^\alpha. \tag{3.6}$$

a) $\alpha = 0.5$

α close to 0.5 indicate that there is no correlation between the current observation and future observation. Prediction of future value, higher or lower than the current observation value is equally likely.

b) $0 < \alpha < 0.5$

α less than 0.5 indicates long–range anti–persistent behavior of time series where an increase in observation value will most likely followed by a decrease or vice–versa.(i.e., values will tend to revert to the mean).

c) $0.5 < \alpha$

α greater than 0.5 indicates long–range strong persistent behavior where an increase in values will most likely be followed by an increase in the short term, and a decrease in values will most likely be followed by another decrease in the short term. Larger α indicates more stronger correlation in the data.

For optimal results, scales should be varied from $m + 2 < s < N/4$ where m is the order of detrending polynomial, to avoid statistical error and over–estimation of the exponent α (KANTELHARDT et al., 2001; KANTELHARDT, 2009).

A flowchart depicting the implementation of the DFA is presented in the appendix A (Figure A.1).

A single exponent value of α characterizes the long–term statistical self–similar

correlation over all temporal scales. In a time series, when correlation properties vary between two different temporal scales, the fluctuation profile is characterized by two different scaling exponents. The change of correlation properties over different scales is known as a crossover. The DFA can capture the crossover in the time series. It is to note that, if time series is not detrended properly, it may also exhibit a crossover. In order to be sure that the obtained crossover is intrinsic to the time series and not an artifact, the higher order DFAm must be applied. If the crossover is not intrinsic, crossover exhibits similar characteristic length with identical scaling (KANTELHARDT et al., 2001).

3.2 Multifractal DFA

When correlation properties change over various scales, it is described by a multitude of scaling exponents, in other words, by superposition of monofractals, and such data has multifractal nature. In such a case, a generalized version of the DFA, i.e., multi–fractal DFA (MFDFA) proposed by Kantelhardt et al. (2002) is a useful tool to characterize multiple scaling behavior in data.

Since its inception, the MFDFA finds numerous application across diverse fields, viz. from physical sciences to social sciences, arts and music to socio–economic behaviors, to understand the complexity and dynamics of a system through its scaling exponents and measures (KANTELHARDT, 2009; KIMIAGAR et al., 2009; MANDAL et al., 2017; TELESCA; LOVALLO, 2011; DUTTA et al., 2013; LU et al., 2016; GRECH, 2016; SALAT et al., 2018; LÓPEZ et al., 2014; TANNA; PATHAK, 2014; MIRIYALA et al., 2015; MUKLI et al., 2015; CHANDRASEKHAR et al., 2016; FRANÇA et al., 2018; KNOWLES et al., 2018; ORAL; UNAL, 2019; JOSHI et al., 2020).

Salat et al. (2017) reviewed four multifractal methods, among which the MFDFA is found to be appropriate to study binomial cascade and its random realization, giving its local complexity and non–homogeneity. And, authors have advised paying close attention to multifractal measures to understand how dynamics evolve than obtaining numerical proof.

3.2.1 Implementation and comprehension of MFDFA

The preliminary step described by Kantelhardt et al. (2002) is to transform the time series to obtain profile $Y(i)$, by computing the cumulative sum of the mean subtracted time series. Based on the DFA exponent, Ihlen (2012) enlist criteria to compute profile for biomedical time series with an objective to convert the time

series into a random–walk like series. This criterion holds true for ionospheric plasma density fluctuation data also. For the chosen time series, the DFA exponents are in the range of $1.2 - 1.8$ and thus the profile, $Y(i)$ is computed by differencing the time series, x, of length N, i.e, $Y(i) = x(i+1) - x(i)$ for $i = 1, 2, ..., N$. Please note that to reduce the effect of nonstationarity, differencing method is suggested before analyzing the series (EKE et al., 2000; EKE et al., 2002). The second step is to compute the qth order local root mean square (RMS) fluctuation function using $Y(i)$. The next two steps, i.e., obtaining the segments and detrending them followed by computing the variance are the same as described in the DFA procedure (equations 3.3 & 3.4). Averaging over all segments, the qth order fluctuation function, $F_q(s)$ is computed.

$$F_q(s) = \left[\frac{1}{2N_s} \sum_{v=1}^{2N_s} [F^2(s,v)]^{q/2} \right]^{1/q} \qquad for \ q \neq 0 \qquad (3.7)$$

when $q = 0$, logarithmic averaging should be used to calculate the fluctuation function.

$$F_0(s) = exp \left[\frac{1}{2N_s} \sum_{v=1}^{2N_s} [ln(F^2(s,v))] \right]. \qquad (3.8)$$

A linear fit to the fluctuation function profile on a log-log scale yields the generalized Hurst exponent, $h(q)$, for each moment q as

$$F_q(s) \propto s^{h(q)}. \qquad (3.9)$$

The presence of multifractality in a time series is inferred from the convergence of fluctuation profile for different q's, which for monofractal series exhibit parallel behavior, being insensitive to scale sizes. For $q = 2$, the generalized Hurst exponent is the DFA exponent.

The generalized Hurst exponent determines scaling behavior with respect to q, i.e., for a given q how smaller to larger fluctuations in segments are scaled in the fluctuation function. For monofractal time series, $h(q)$ is independent of q and for multifractal time series $h(q)$ shows a linear dependence on q as smaller to larger fluctuations scale differently. In a segment, negative q characterize fluctuations smaller than average, while positive q characterize fluctuations larger than average. For $q = 0$, the behavior is neutral. $h(q)$ for positive q illustrate the scaling behavior of segments (scales) influenced by large fluctuations and is described by smaller scaling exponent value. Similarly, $h(q)$ for negative q illustrate the scaling behavior of segments (scales) influenced by small fluctuations and is described by larger scaling exponent value.

It is to note that rapid variations in fluctuations are identified with smaller scales, while slow variations with large scales. Therefore, to characterize all types of fluctuations, scales should be varied across all size range i.e., from small to large sizes. In the present analysis, scales are varied up to $1/10^{th}$ of the total length of the time series and an optimal linear fit to the $F_q(s)$ is then obtained. The moments, q, are varied in the range of -5 to $+5$, given the short length of the analyzed series.

The variations in $h(q)$ with respect to q is then examined to determine the influence of fluctuations in a given time series. When time series is influenced by smaller fluctuations, $h(q)$ will vary faster with q, resulting in a steeper slope for negative q's and vice–versa (KANTELHARDT et al., 2002; IHLEN, 2012). To summarize, $h(q)$ vs q profile quantifies the scaling properties of segments influenced by fluctuations larger (smaller) than average and are described by smaller (larger) scaling exponent values of $h(q)$ for positive (negative) q.

Scaling exponent, $\tau(q)$, can be obtained through the partition function based multifractal analysis and can be related to the scaling exponent $h(q)$ obtained through the MFDFA by,

$$\tau(q) = qh(q) - 1 \tag{3.10}$$

The nonlinear dependence of $\tau(q)$ upon q indicates multifractality in the data.

Another way to depict the multifractality in the series is to examine multifractal spectrum $(\alpha, f(\alpha))$ which is calculated using $h(q)$ as

$$\alpha = h(q) + qh'(q) \tag{3.11}$$

$$f(\alpha) = q(\alpha - h(q)) + 1 \tag{3.12}$$

where α[1] represents multifractal strength (local exponent) and $f(\alpha)$ represents set of multifractal dimensions.

Also multifractal spectrum can be computed using scaling exponent $\tau(q)$ as:

$$\alpha = \tau'(q) \tag{3.13}$$

$$f(\alpha) = q\alpha - \tau(q) \tag{3.14}$$

The spectrum reveals the local fractal dimension for q, with α illustrating the range

---

[1]Please note, this MFDFA–α is different than the DFA–α described in the DFA section.

of scaling exponents present in the time series, and $f(\alpha)$ discloses its dimension informing, how scaling indices are distributed. The multifractal spectrum reflects the characteristics of the $h(q)$ profile. In the spectrum, contrary to the $h(q)$ profile, the left side is characterized by positive values of q, and the right side is characterized by negative values of q. When the $h(q)$ profile show steeper variations on the left side corresponding to negative q's, it reflects on the right side of the spectrum showing faster variations comparing to its left side.

A flowchart depicting the implementation of the MFDFA is presented in the appendix A (Figure A.2).

Shape and width of the multifractal spectrum are also important measures to quantify the nature of multifractality present in the time series. Figure 3.1 presents a model diagram of multifractal spectrum inferring multifractal measures.

Figure 3.1 - Multifractal spectrum model.
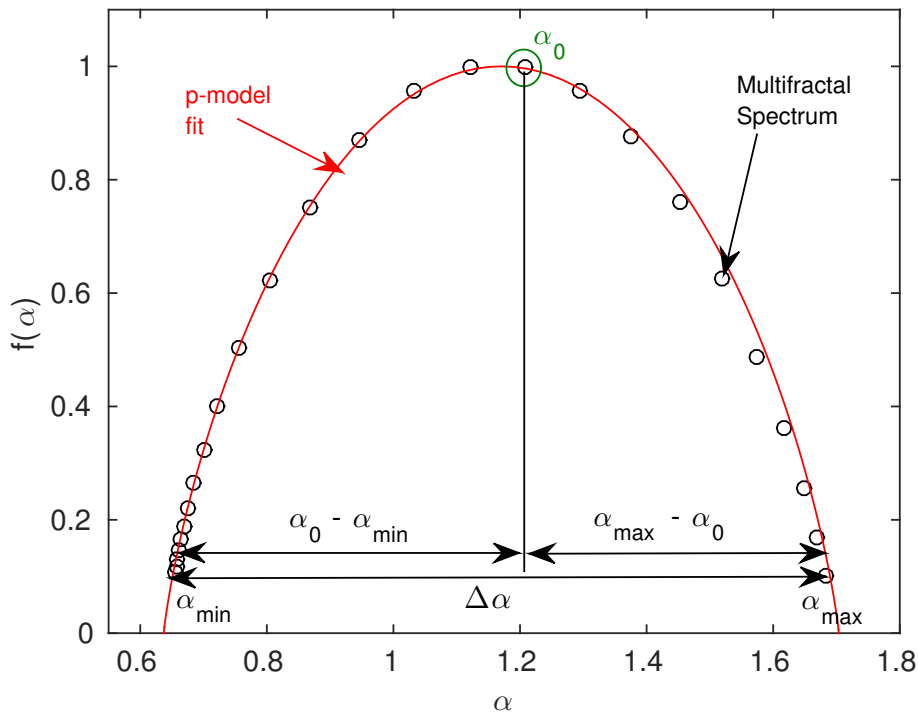
Source: produced by author.

Two extreme values of α have indicated as α_{min} which is minimum value of α and α_{max} which is maximum value of α. Difference between these two values infer a

21

multifractal measure, namely, multifractal spectrum width or degree of multifractality. The multifractal spectrum width or degree of multifractality ($\Delta\alpha$) indicates the range of fractal exponents between maximum and minimum dimension, illustrating how segments with small and large fluctuations deviate from the average fractal structure.

$$\Delta\alpha = \alpha_{max} - \alpha_{min}. \tag{3.15}$$

Larger (smaller) value of $\Delta\alpha$ infers stronger (weaker) multifractality via a broader (narrower) set of monofractals in the time series (ABRAMENKO, 2005). Multifractal width quantifies the richness of scaling and directly relates to the parameters corresponding to the multiplicative cascade process (explained in chapter 4). For multifractals, self–similarity is scale dependent and intermittency can be defined as a deviation from the strict self–similarity (MACEK, 2007; CHENG, 2014). The intermittency in a turbulent system is analogous to the multifractality in the fractal theory (FRISCH, 1995; ABRAMENKO et al., 2002). Hence, $\Delta\alpha$ quantifies the intermittency in the time series.

To obtain second multifractal measure, one must first find the value of α_0 corresponds to the maximum value of $f(\alpha)$ for $q = 0$. In Figure 3.1, it is marked by green circle. Considering α_0 as a reference, divide the spectrum in two parts and calculate the width. Left part width can be obtained as $\alpha_0 - \alpha_{min}$ and right part width can be obtained as $\alpha_{max} - \alpha_0$. Now, second multifractal measure, namely, the measure of asymmetry, A, is quantified by calculating the ratio of left width and right width of the spectrum. The measure of asymmetry is given by

$$A = \frac{\alpha_0 - \alpha_{min}}{\alpha_{max} - \alpha_0}. \tag{3.16}$$

When ratio is equal, i.e., when $A = 1$, spectrum is symmetric, and thus a series is influenced equally by larger as well as smaller fluctuations than the average. When numerator is larger than denominator, i.e., when $A > 1$, the left width of the spectrum is larger and the spectrum is called left–skewed. The left part of spectrum characterized by positive values of q, hence the left–skewed spectrum indicates influence of the larger fluctuations than the average. When denominator is larger than numerator, i.e., when $A < 1$, the right width of the spectrum is larger and the spectrum is called right–skewed. The right part of spectrum characterized by negative values of q, hence the right–skewed spectrum indicates influence of the smaller fluctuations than the average. This is summarized in a Table 3.1.

Table 3.1 - Measure of asymmetry.

range	skewness	implies
$A < 1$	right–skewed	influence of smaller fluctuations
$A = 1$	symmetric	equal influence of smaller and larger fluctuations
$A > 1$	left–skewed	influence of larger fluctuations

A lower value of α_0 indicates more correlated and regular structures, whereas larger value indicates the presence of irregular structures in time series. In Figure 3.1, red line fitted to the multifractal spectrum (circle marker) is the singularity spectrum obtained using the p model, which is explained in the next chapter in section 4.2.

Kantelhardt et al. (2002) suggested a method to identify two possible sources behind the multifractality present in the series, viz. due to long–range correlations and a broad probability density function. Suggested method is to apply the MFDFA method on shuffled time series and then compare results with original time series. Shuffling of time series destroys all possible correlations. If shuffled series exhibit monofractality then multifractality is attributed to long–range correlations. If shuffled series retains its multifractality then it is attributed to the broad probability density function. However, if the shuffled time series exhibits weaker multifractality compared to the original time series, then both types of multifractality are present.

4 METHODS: MULTIPLICATIVE CASCADE MODELS

The underlying theoretical formalism for the multiplicative cascade processes (MCP) is the Richardson's energy cascade model (Figure 2.2) for the dissipation of eddies in a turbulent field. The process envisages the top–down approach of the energy cascade model where large eddies break down into small ones recursively, carrying a fraction of kinetic energy at each step until Kolmogorov scale is attained where dissipation occurs effectively.

The early simple model to mimic MCP was given by Kolmogorov in 1941 which only considered the isotropic distribution of the mean flux of energy ϵ from large to small scales. The 1941 theory of Kolmogorov did not account for intermittency. Later, Kolmogorov proposed the log–normal model for ϵ by invoking some statistical independence in the cascading process. The log–normal model suffered a setback with not representing for the higher order (>3) moments (MANDELBROT, 1972; MENEVEAU; SREENIVASAN, 1987; MENEVEAU; SREENIVASAN, 1991). Mandelbrot introduced fractal model, known as β model, where the flux of energy is transferred to only a fixed fraction β of the eddies of subsequent generation. For the log–normal and β model, ϵ was not scale invariant, i.e., the mean and variance of ϵ were changing in each cascade step.

Meneveau and Sreenivasan (1987) proposed the p model which is an intermediate to the Kolmogorov's 1941 model and β model and is based on binomial or two–scale Cantor model to account for non–homogeneities during the cascade process (MENEVEAU; SREENIVASAN, 1991).

4.1 Binomial multifractal model

A binomial measure μ, also called the Bernoulli or Besicovich measure demonstrate exact self–similar measures. A recursively iterating measure, μ, allows to construct the MCP which yields binomial multifractal series (KANTELHARDT et al., 2002; PEITGEN et al., 1992; FEDER, 1988).

One starts (first generation, $n = 0$) with a uniformly distributed unit of energy on the unit interval $I = I_0 = [0, 1]$. In the next iteration ($n = 1$), divide the unit interval uniformly into two halves - $I_L = [0, \frac{1}{2}]$ with a measure $\mu(I_L) = a$ and $I_R = [\frac{1}{2}, 1]$ with a measure $\mu(I_R) = 1 - a$. At this stage, note that the measure μ is conserved as $\mu(I) = \mu(I_L) + \mu(I_R) = a + (1 - a) = 1$, and is a probability measure.

In the second iteration ($n = 2$), the subintervals I_{LL} and I_{LR} follows the same cascade

procedure. It will result in 4 subintervals: $I_{LL} = [0, \frac{1}{4}]$; $I_{LR} = [\frac{1}{4}, \frac{1}{2}]$; $I_{RL} = [\frac{1}{2}, \frac{3}{4}]$; $I_{RR} = [\frac{3}{4}, 1]$ of size 2^{-n}. The measure will be $\mu(I) = \mu(I_{LL}) + \mu(I_{LR}) + \mu(I_{RL}) + \mu(I_{RR}) = a.a + a.(1-a) + (1-a).a + (1-a).(1-a) = 1$. Hence the measure is continued to be conserved. At the nth generation i.e., $n = n_{max}$, one obtains the multifractal time series x_k of length $N = 2^{n_{max}}$ with $k = 1, 2, ..., N$ as

$$x_k = a^{n(k-1)}(1-a)^{n_{max}-n(k-1)} \tag{4.1}$$

where a takes value between $(0.5,1)$ and $n(k)$ is a number of $1's$ appearing in the binary representation of index k. Using binomial model, the scaling exponent $\tau(q)$ and multifractal width $\Delta\alpha$ can be computed as:

$$\tau(q) = [-ln(a^q + (1-a)^q)]/ln(2) \tag{4.2}$$

$$\Delta\alpha = [ln(a) - ln(1-a)]/ln(2). \tag{4.3}$$

Figure 4.1 - Scaling exponent generated by the binomial model compared with the scaling exponent computed by the MFDFA for the time series of the mean height of 263.47 km from the valley region. (a) time series generated with binomial cascade for $\Delta\alpha = 0.47$; (b) corresponding scaling exponent obtained from binomial cascade (x) and scaling exponent computed from the MFDFA (○).
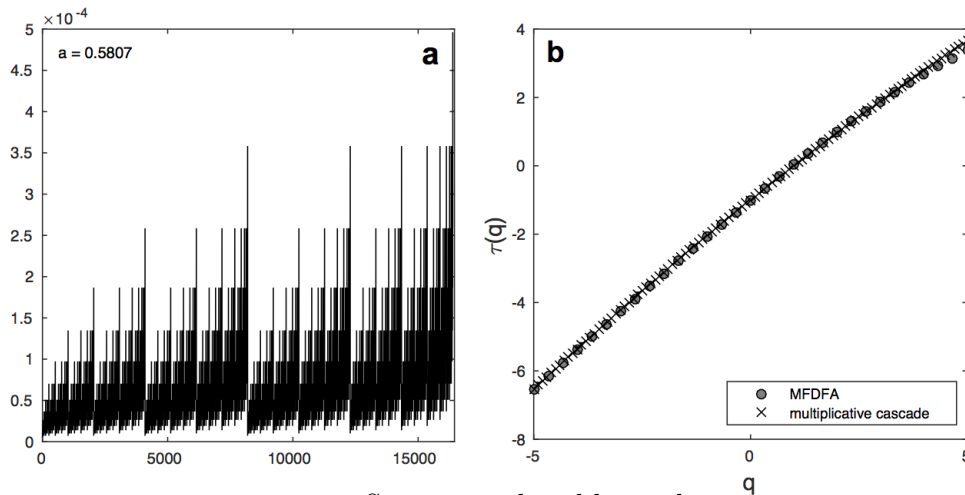
Source: produced by author.

Taking bottom–up approach, one can compute a using the Equation 4.3 where $\Delta\alpha$ is obtained from the empirical time series subjected to the MFDFA. Once a is

computed, multifractal time series x_k can be modeled using Equation 4.1 and $\tau(q)$ can be computed using Equation 4.2. The computed $\tau(q)$ can be compared with the $\tau(q)$ obtained from the MFDFA. When generated time series x_k is subjected to the MFDFA, it gives approximately similar results as the empirical time series.

Figure 4.1 shows an example of the modeled time series using the binomial multifractal model described above. The measure a is computed from $\Delta\alpha = 0.47$ in one of the case study presented in this thesis (please refer chapter 5). The case study refers to the ionospheric electron density fluctuation time series corresponding to the mean height of 263.47 km from the valley region 5.3, analyzed using the MFDFA method. Equation 4.3 gives $a = 0.5807$ which is substituted in Equation 4.1 to obtain the time series shown in the left panel (Figure 4.1a). $\tau(q)$ is computed using Equation 4.2 which is shown in the right panel (Figure 4.1b) and for the comparison, $\tau(q)$ for the case study obtained from the MFDFA is also shown. It can be seen that the $\tau(q)$ for the modeled time series lies close to the one obtained in the case study thus demonstrating the practicality of using the analytical formulation and validating it with the numerical results from the MFDFA.

Figure 4.2 - Time series generated by binomial model shown in Figure 4.1 is subjected to the MFDFA. (a) scaling exponent computed by the binomial model (+) along with scaling exponent obtained from the MFDFA (○); (b) singularity spectrum computed by the binomial model (+) along with multifractal spectrum obtained from the MFDFA (○).
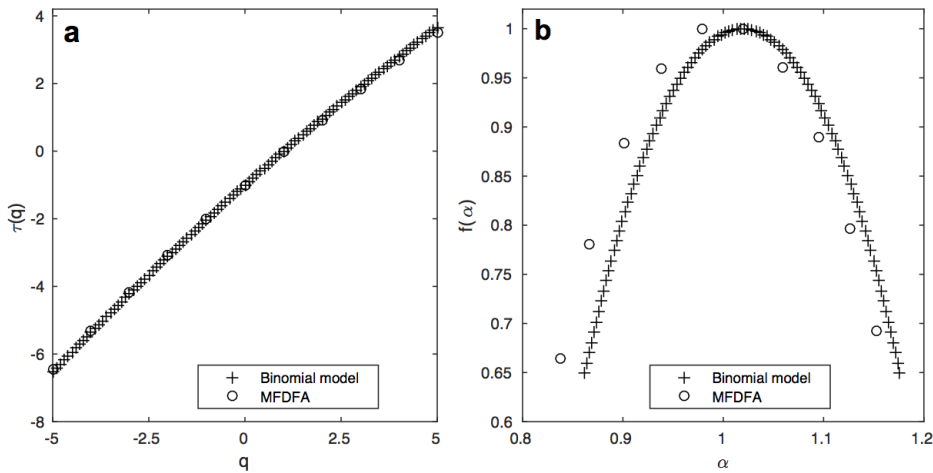
Source: produced by author.

The time series obtained from the binomial model using $\Delta\alpha = 0.47$ (shown in Figure

27

4.1) is subjected to the MFDFA. Figure 4.2 shows the comparison of the scaling exponent $\tau(q)$ (Figure 4.2a) and singularity spectrum (Figure 4.2b) obtained from the binomial model and from the MFDFA. Singularity spectrum is calculated from scaling exponent obtained from binomial model using Equations 3.13 and 3.14.

4.2 The p model

Meneveau and Sreenivasan (1987) proposed the p model which is based on the generalized two–scale Cantor set to mimic the possible energy transfer in the turbulent cascade process. In this work, this p model is opted to compute the best possible fit parameters to the multifractal spectrum. The p model depicts the energy cascading process in the inertial range of a fully developed turbulence for the dissipation field, which is based on the generalized two–scale Cantor set. The model comprises of unit structure with energy E_L. Energy distribution occurs at each subsequent level (referred to as a generation) through binary fragmentation with probabilities p_1 and p_2 among the fragments of length l_1 and l_2. In the cascading process, n denotes the number of generations. In each generation, the segment size is given by $l_1^m l_2^{n-m}$ where m denotes the number of left side fragments and $n-m$ represents right side fragments in a segment (HALSEY et al., 1986). Figure 4.3 present a schematic for the p model.

Figure 4.3 - Schematic representation of the p model.
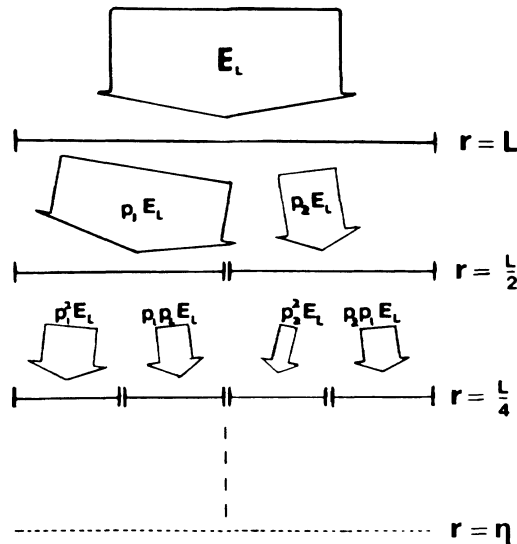
Source: Meneveau and Sreenivasan (1987).

An analytical formulation to determine the generalized multifractal dimensions, strength (α) and its distribution ($f(\alpha)$), which represent the singularity spectrum, based on the generalized two–scale Cantor set is given by (HALSEY et al., 1986)

$$\alpha = \frac{lnp_1 + (n/m - 1)lnp_2}{lnl_1 + (n/m - 1)lnl_2} \tag{4.4}$$

$$f(\alpha) = \frac{(n/m - 1)ln(n/m - 1) - (n/m)ln(n/m)}{lnl_1 + (n/m - 1)lnl_2}, \tag{4.5}$$

where ratio n/m can be calculated as p_2/p_1 ((HALSEY et al., 1986; HILBORN, 2000).

The p model is based on the above formulation given by Halsey et al. (1986). The p model considers equal lengths, $l_1 = l_2$ and with unequal weights ($p_1 \neq p_2$ and $p_1 + p_2 \leq 1$). When $p_1 + p_2 \leq 1$, loss in p parameter is given by $dp = 1 - p_1 - p_2$, accounts for the direct energy dissipation in the energy cascading process in the inertial range. With $p_1 + p_2 = 1$ parameters, the p model always gives symmetric multifractal spectrum unless the dissipation parameter, dp is introduced. Multifractality ceases to exist for $p = 0.5$, recovering the homogeneous energy multiplicative cascade pattern, which is monofractal. The p model always describes cascading processes in the multifractal time series (MENEVEAU; SREENIVASAN, 1987). Using Equations 4.4 and 4.5, the fit parameters are estimated to obtain optimal fit to the multifractal spectrum from the MFDFA, thus, confirming the multifractality of the time series and as well unveil the scaling of the time series with possible probabilities. The usefulness of this fit is that with the attained fit parameters, one can approximate the energy cascading process to model the multifractal time series (MENEVEAU; SREENIVASAN, 1987; KANTELHARDT, 2009).

Following the procedure described above for generating binomial multifractal time series, one can model the time series using p model parameters. To construct the time series, consider an initial length L with height ϵ_L. Divide it into two equal segments ($L/2$) with probabilities p_1 and p_2 (with $p_1 + p_2 = 1$) assigning randomly to the left or right part. Assign height as $2p_1\epsilon_L$ and $2p_2\epsilon_L$. Iterate this step for desired n^{th} generation to obtain time series. As probability p_1 is assigned randomly to the segments in each generation, different realization of the time series can be obtained in each run.

Figure 4.4 presents time series generated by p model cascade at 1st, 5th and 12th iteration in panel a, b, and c respectively with $p_1 = 0.7$. Panel d shows the time series generated with $p_1 = 0.418$ which is obtained from the p model fit to the ionospheric

electron density fluctuation time series corresponding to the mean height of 263.47 km from the valley region.

Figure 4.4 - The p model time series: (a) first stage (b) fifth stage (c) twelfth stage (d) twelfth stage construction of time series with $p_1 = 0.418$.
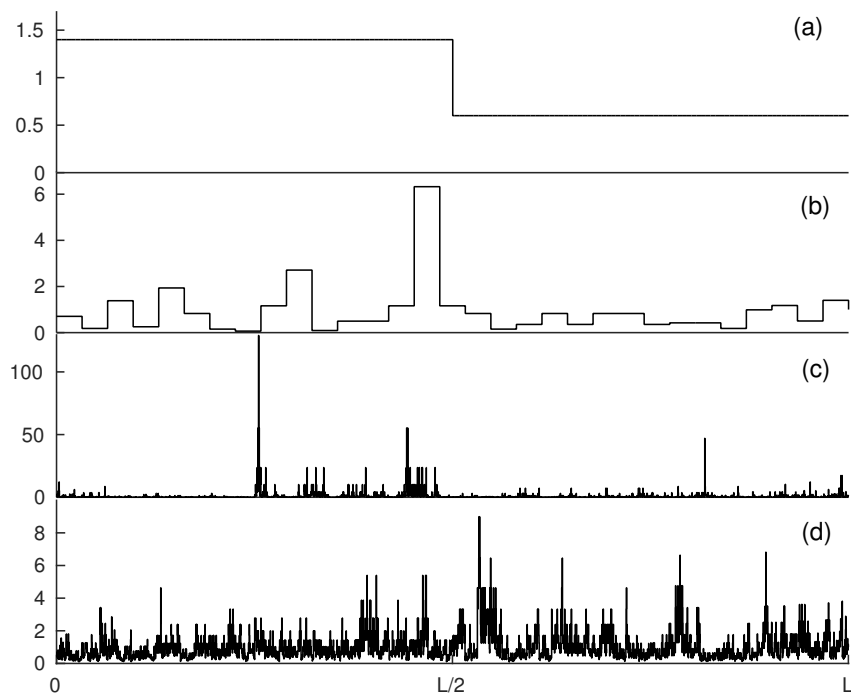
Source: produced by author.

4.3 Direct model for singularity spectrum

Chhabra and Jensen (1989) provided a direct method to determine singularity spectrum α–$f(\alpha)$ accurately without a need of Legendre transform or without neglecting logarithmic corrections and without any poor statistical sampling. Also, this method allow to compute singularity spectrum with multiplicative cascade using different base, since correct base of the multiplicative process for empirical data is mostly unknown.

Method starts with considering the base, say $a = 2$. Consider a unit interval and two unequal probabilities, p_1 and p_2, where $p_1 + p_2 = 1$. Divide the unit interval into two equal segments with respective probabilities. Repeat this process for n generations such that there will be $N = a^n$ segments at n^{th} level with equal length $L = a^{-n}$

with probabilities $P_i(L) = p_1^{n-k} p_2^k$ where $k = 0, ..., n$. Next step is to construct a one–parameter family of normalised measures for the segments as

$$\mu_i(q, L) = \frac{[P_i(L)]^q}{\sum_j [P_j(L)]^q}, \tag{4.6}$$

where q are moments varying from negative to positive values.

$$\alpha(q) = -\lim_{L\to 0} \frac{\sum_i \mu_i(q, L) log[P_i(L)]}{log L} \tag{4.7}$$

$$f(q) = -\lim_{L\to 0} \frac{\sum_i \mu_i(q, L) log[_i(q, L)]}{log L}. \tag{4.8}$$

For each q, calculate numerators of Equations 4.7 and 4.8. On log–log scale, plot the numerators calculated above against $log(L)$. The slope derived from the respective plots gives the singularity spectrum (α and $f(\alpha)$).

Figure 4.5 shows the singularity spectrum obtained from the direct determination method for the base 2 and it is compared with the singularity spectrum obtained using the p model with probability $p_1 = 0.7$.

Figure 4.5 - Singularity spectrum generated using direct determination method with $p_1 = 0.7$ and with base 2 (+). It is compared with singularity spectrum obtained using the p model with $p_1 = 0.7$ (○).

Source: produced by author.

31
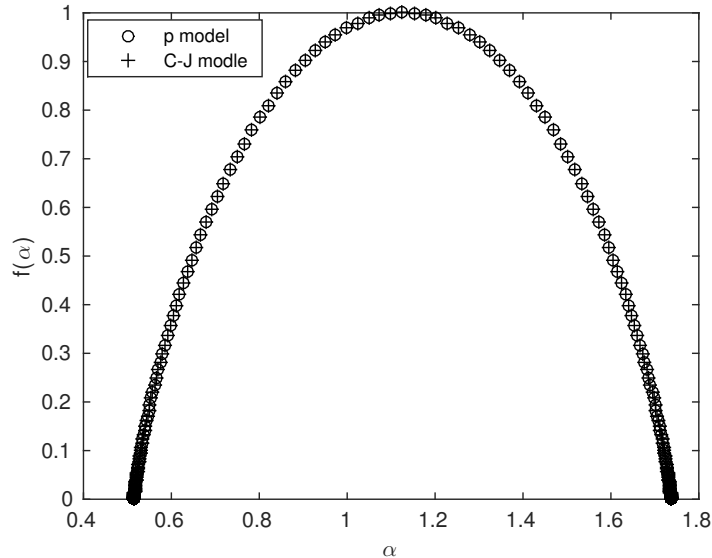
MCP plays an important role in quantifying the intermittency in nonlinear processes. Also, helps to reconstruct he time series from the singularity spectrum. Rosa et al. (2008), Rosa et al. (2010) analyzed decimetric solar bursts using multifractal and p model methods. Authors characterized solar emissions as intermittent, non–homogeneous plasma turbulence. Rosa et al. (2019) modeled armed conflict data using p model and is presented in section 5.4.

The two–scale Cantor set and p model has been applied to quantify multifractality (LEE et al., 2006; MACEK, 2007; BOLZAN et al., 2009; PASCHALIS et al., 2012; BOLZAN et al., 2013). Applications of MCP can be found in Barabási and Vicsek (1991), Carbone (1993), Burlaga et al. (2003), Kantelhardt et al. (2002), Kantelhardt (2009), Koscielny-Bunde et al. (2016). Different methods and review can be found in Redner (1989), Greiner et al. (1998), Xiong et al. (2014), Xiong et al. (2016), Dubrulle (2019).

5 APPLICATIONS AND RESULTS

This chapter presents the fractal and multifractal analysis of equatorial ionospheric irregularities in the first section. Second section presents multifractal analysis of the type I noise storm series and in the third section, how endogenous and exogenous time series can be modeled is described.

5.1 Analysis of the valley region irregularities

5.1.1 Data

A two–stage VS-30 Orion sounding rocket was launched from the equatorial rocket launching station Alcântara $(2.31°S; 44.4°W)$ at 19:00 LT, on December 8, 2012, under favorable conditions for strong spread F. During the ~ 11 min flight, the rocket traversed through the E-F valley region with an apogee ~ 428 km and ranging ~ 384 km horizontally. In the downleg trajectory, a wide base for the F region has been identified above 300 km with some small scale fluctuations and the valley region as $130 - 300$ km. Various small and medium plasma irregularities were observed in the valley region. The ground equipment, a digisonde, was operated from equatorial station and reported fast uplift of the base of F region, thus indicating the possibility of the pre–reversal enhancement of the F region vertical drift (SAVIO et al., 2016; ODRIOZOLA et al., 2017; ODRIOZOLA, 2017).

The vertical profile of electron density was obtained from the conical Langmuir probe (CLP) on board the rocket, which worked in swept and constant bias modes. CLP sensor potential was swept from -1V to +2.5V linearly in about 1.5 s, during which electron kinetic temperature was inferred using the collected probe current (SAVIO et al., 2016). Then the potential was maintained at +2.5V (constant bias mode) for 1 s, during which collected probe current was used to estimate electron density and its fluctuations, in each experiment cycle. During constant bias mode, data were sampled with low as well as high sampling frequency. Low frequency sampled data is used to show electron density profile plot whereas high frequency sampled data of electron density fluctuations is used for the analyses.

This work utilizes the electron density fluctuation data obtained from the CLP. Figure 5.1 shows variations of the vertically distributed electron densities in the downleg (descent of the rocket) trajectory of the flight. In downleg trajectory, a wide base for the F region has been identified above 300 km and the valley region around $130 - 300$ km. Various small and medium plasma irregularities were reported

in the valley region (ODRIOZOLA et al., 2017).

Figure 5.1 - (a) Rocket flight trajectory (b) Upleg profile with one sample time series (c) Downleg profile with one sample time series.
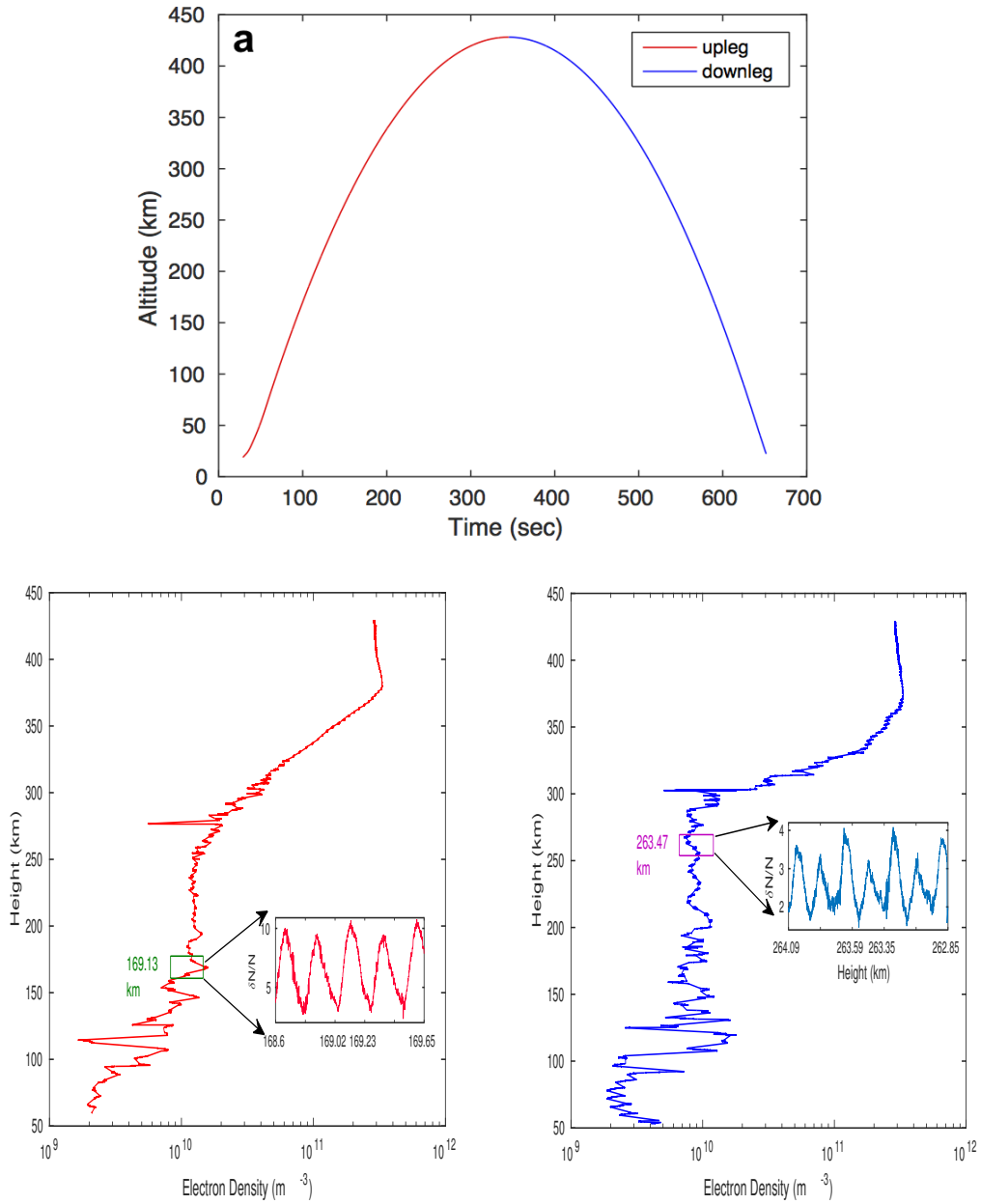
Figure 5.1a show the rocket trajectory for the duration of 651.52 s. Lower panel shows variations of the vertically distributed electron densities in the upleg (Figure

5.1b) as well as in the downleg (Figure 5.1c) trajectory of the flight. These upleg and downleg profiles are sampled with low frequency. A time series is shown in the inset which is obtained through high frequency sampling.

For detailed explanation of *in situ* experiment please refer Odriozola (2017).

5.1.2 DFA of the valley region data

This is the first analysis reported on the application of DFA to *in situ* the valley region irregularities. Implementation procedure is described in chapter 3, section 3.1.2. Appendix presents detailed analysis using four time series from the downleg profile in the form of a published article (NEELAKSHI et al., 2019). The DFA analysis for four time series corresponding to the mean height of 152.56, 169.13, 263.69 and 316.9 km from upleg profile is presented in the appendix B (Figure B.1).

Long–range correlation with crossover
In this section, the DFA analysis is demonstrated for a time series corresponding to mean height of 169.13 km from the upleg profile, and a time series corresponding to 143.03 km from downleg profile.

These time series are subjected to DFA analysis. Scales are varied from 4 to $n/4$ in steps of $2^{\frac{1}{8}}$, where n is the length of time series (GOLDBERGER et al., 2000). DFA exponents are obtained from the fit to the fluctuation function profile. The exponents for the smaller scales are denoted by $\alpha 1$ and that for larger scales by $\alpha 2$. The chosen time series exhibit long–range correlation and also shows a crossover.

To find whether obtained crossover is inherent to the data or an artifact, time series have been detrended using different polynomial orders $1^{st} - 5^{th}$ and plotted on a log–log scale. All the chosen time series exhibit crossover behavior. Crossover scale and corresponding scaling exponents have been noted for all orders. Crossover scale differs with respect to detrending order and also value of scaling exponents vary with different detrending order. This analysis for upleg time series for mean height of 169.13 km is presented for DFA 1st order to 5th order in Figure 5.2a and corresponding values are listed in Table 5.1. Figure 5.2b presents the analysis for downleg time series corresponding to the mean height of 143.03 km with DFA of 1st to 5th order. The crossover exponents are listed in Table 5.1. It can be observed that as the order of detrending increases, crossover point moves towards larger scales and have different scaling exponents. This investigation confirms that the obtained crossover is an intrinsic property of electron density fluctuation data in the valley

region.

Figure 5.2 - (a) DFA1 to DFA5 for upleg time series of the mean height of 169.13 km and (b) DFA1 to DFA5 for downleg time series of the mean height of 263.47 km.
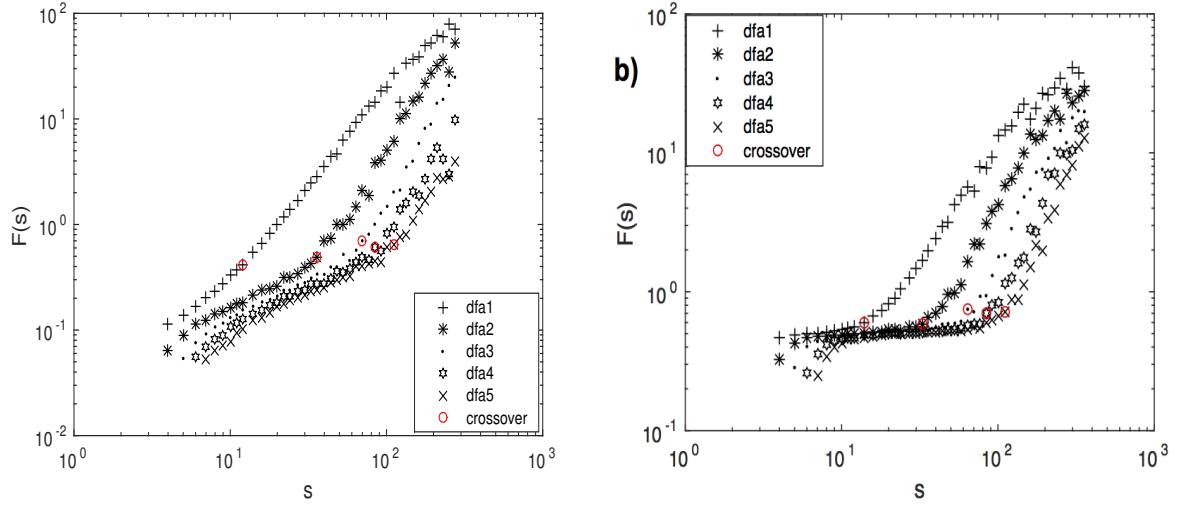
Source: produced by author.

Table 5.1 - Crossover scaling exponents for detrending order 1 to 5 (DFA1 to DFA5) for upleg time series at mean height of 169.13 km and downleg time series at mean height of 143.03 km.

time series (km)	exponent	DFA1	DFA2	DFA3	DFA4	DFA5
upleg <169.13>	$\alpha1$	1.21	0.83	0.82	0.80	0.82
	$\alpha2$	1.73	2.36	2.74	2.13	2.04
	crossover at scale	12	36	70	84	111
downleg <143.03>	$\alpha1$	0.39	0.15	0.12	0.10	0.13
	$\alpha2$	1.50	1.93	2.08	2.26	2.53
	crossover at scale	16	33	53	70	101

In the analysis, for upleg series, $\alpha1$ varies in the range 0.80 to 1.21 and $\alpha2$ in 1.73 to 2.74. For downleg series, the analysis reveals $\alpha1$ to be in the range 0.10 to 0.39 and $\alpha2$ in the range 1.50 to 2.53. For mean heights corresponding to 169.13 and 143.03 km, $\alpha1$ is smaller than $\alpha2$. The scales at which crossover occurs are listed in Table 5.1.

Numerous studies using PSD have been reported earlier. PSD indices reported earlier using *in situ* electron density fluctuations for altitudes near the range of valley region $(130 - 300$ km$)$ are examined for the deviation from K41 universality class $(-5/3)$. For the current data, the DFA exponent α is converted to PSD index β using the equivalence relation (equation 3.1), and the standard deviation σ_m (in %) is determined. The computed DFA exponents in this analysis show a wide range of β from -0.98 to -2.14 with $\sigma_m = 58\%$. Table 5.2 summarizes the variations in the β exponent obtained from the previous equivalent studies (RINO et al., 1981; KELLEY et al., 1982; MURALIKRISHNA; VIEIRA, 2007; SINHA et al., 2010; SINHA et al., 2011) and compares with the present work. It is observed that the computed standard deviation $\sigma_m \gg 50\%$. Figure 5.3 shows DFA exponents for four time series from upleg and downleg profile each and these exponents vary from $-5/3$.

Figure 5.3 - DFA exponent α vs. mean height for four time series each from upleg (red diamonds) and downleg (blue circles). Solid line in the shaded area indicates the exponent value for homogeneous turbulence $(\beta = -1.66,$ i.e., $\alpha = 1.33)$; shaded area shows the range of alpha value deviation $\pm 2\%$.
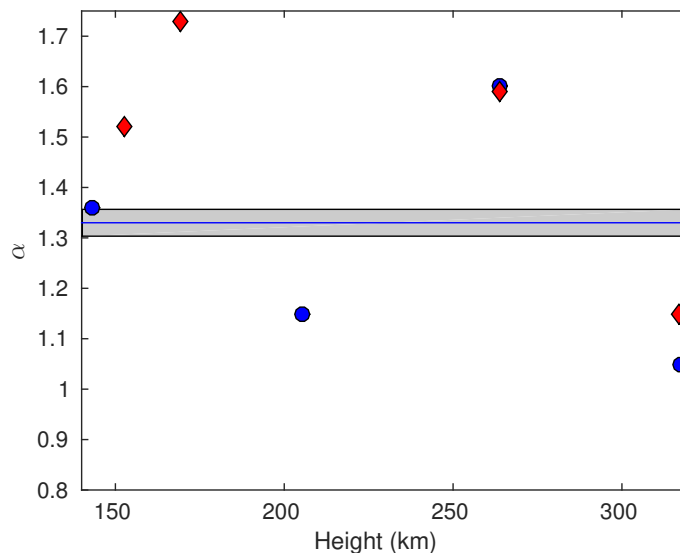
Source: produced by author.

These deviation endorse the previous finding (FORNARI et al., 2016) that the mechanism responsible for ionospheric irregularities is different than the K41 theory for

Table 5.2 - Comparison of PSD spectral indices (β) found in previous equivalent studies and β obtained here from DFA. All results measured using rockets are related to electronic density measurements during the experiment.

Date and Time	Spacecraft	Altitude (km)	β range	$\langle\beta\rangle$	σ_m	References
17/07/1979, 12:31:30 UT	Rocket	250 to 370	-1.20 to -3.4	-2.3	110%	Rino et al. (1981)
17/07/1979, 12:31:30 UT	Rocket	250 to 285	-2.00 to -3.4	-2.7	70%	Kelley et al. (1982)
11/12/1985, 00:30 UT	Rocket	210 to 306	-1.34 to -3.3	-2.32	98%	Muralikrishna and Vieira (2007)
31/10/1986, 03:00 UT	Rocket	100 to 220	-1.54 to -3.30	-2.42	88%	Muralikrishna and Vieira (2007)
15/01/2007, 16:43 UT	Rocket	- to 127	-1.60 to -2.70	-2.15	55%	Sinha et al. (2010)
29/01/2008, 15:49 UT	Rocket	- to 117	-2.00 to -3.50	-2.75	75%	Sinha et al. (2011)
08/12/2012, 22:00 UT	Rocket	- to 317	-0.98 to -2.14	-1.56	58%	This work

homogeneous turbulence cascade as its permitted deviation is $\sigma_m \leq 2\%$ (FRISCH, 1995). Hence, this wide variation affirms that ionospheric irregularities from the valley region are non–homogeneous.

Figure 5.3 shows the DFA scaling exponents plotted as a function of height for time series from both upleg and downleg profile. For this plot a single linear fit for the valley region data have used. The shaded horizontal bar in the plot represents the exponent value, $\alpha = 1.33 \pm 2\%$, for the homogeneous turbulence described by the K41 theory. Wide variation in the scaling exponents from the K41 theory is apparent.

5.1.3 MFDFA of the valley region data

From the DFA, it is inferred that the valley region data exhibit long–range correlation with crossover. It is interesting to explore, does this data exhibit correlation across various scales. Hence, the multifractal analysis is performed to detect multifractal signature. This is the first analysis reported on the application of MFDFA to *in situ* valley region irregularities. Implementation procedure is described in chapter 3, section 3.2. For the analyses, eight time series of electron density fluctuations are chosen at mean heights of 194.58, 214.64, 219.19, 237.61, 259.34, 263.47, 275.67 and 283.95 km.

Figure 5.4 presents detailed multifractal analysis performed on a time series of the mean height of 263.47 km.

Figure 5.4 - MFDFA for mean height of 263.47 km: (a) normalized time series (upper panel) along with differenced time series (lower panel), (b) fluctuation profile for different q with their respective linear fit, (c) $h(q)$ vs q profile (d) $\tau(q)$ vs q profile where dashed line represent linear relationship between $\tau(q)$ and q, (e) multifractal spectrum (circles with error bars) fitted with p model (continuous line), and multiplicative cascade (dashed line); and (f) multifractal spectra obtained by shuffling the time series (square marker) along with original time series (circle marker).
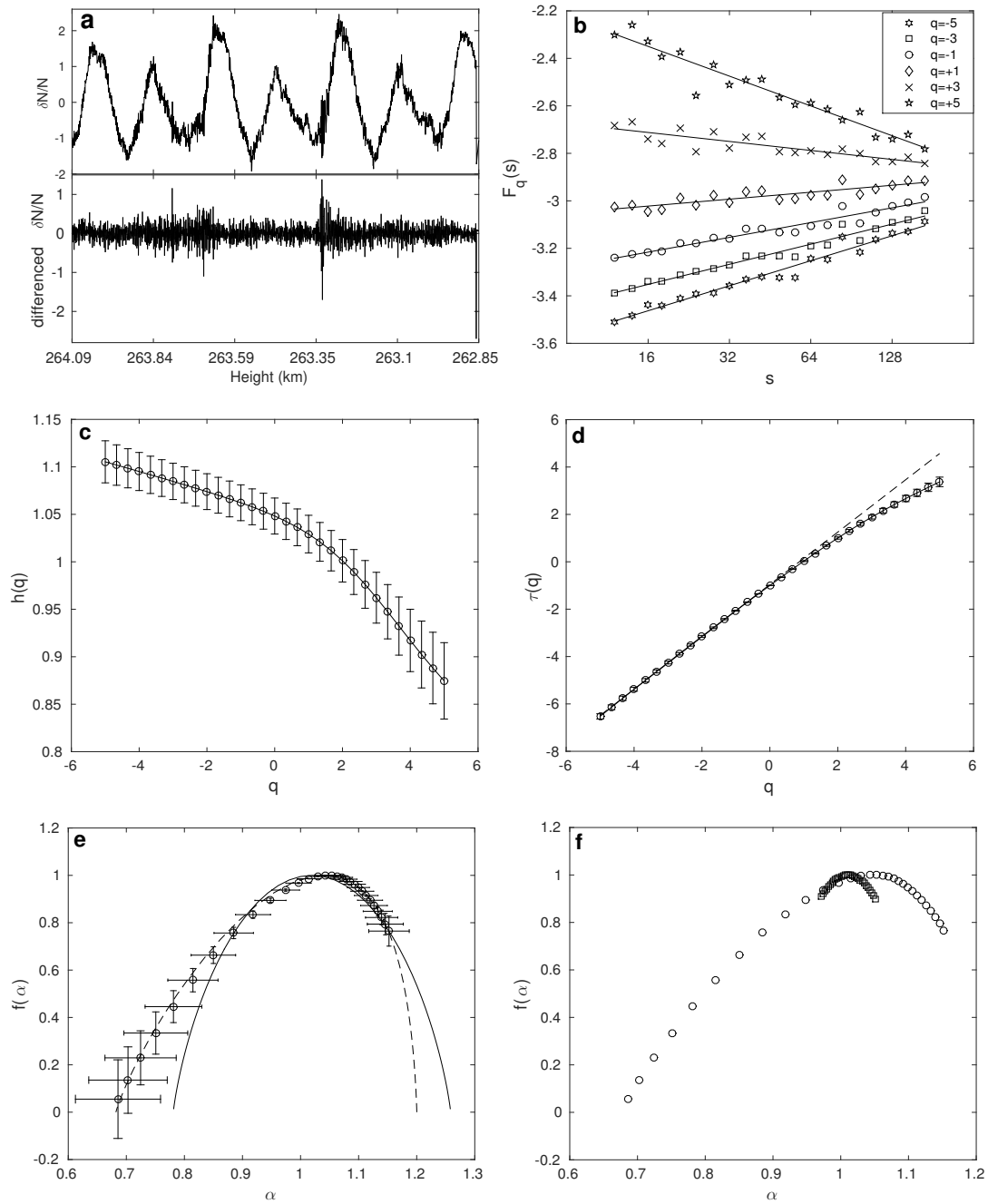
Source: produced by author.

Figure 5.4a shows the normalized time series (upper panel) along with differenced time series (lower panel). The differenced time series is the profile $Y(i)$. The differenced time series exhibits intermittent behavior as it shows sudden bursts, i.e., high intensity fluctuations surrounded by large number of small intensity fluctuations (MONIN; YAGLOM, 1975). The fluctuation profile for different q with their respective linear fit is presented in Figure 5.4b. The fit is shown only for $q = -5, -3, -1, +1, +3, +5$, where the slope of the fit yields $h(q)$ for corresponding q's. It can be seen that the fluctuation profile for different q's converges at higher scales, which asserts the presence of multifractality in the time series. Please note that crossover is not observed with the MFDFA method, though it is observed with the DFA method.

Figure 5.4c shows $h(q)$ vs q profile. $h(q)$ decreases with q, reaffirming the presence of multifractality. For positive q, the slope is much steeper compared to negative q, which indicates $h(q)$ characterizes larger fluctuations than average. This is evident in the multifractal spectrum too which is described shortly. Figure 5.4d shows $\tau(q)$ vs q profile where dashed line represents a linear relationship between $\tau(q)$ and q. Variation of $\tau(q)$ with respect to q shows marked deviation from linearity, again confirming the multifractal nature.

Figure 5.4e shows the multifractal spectrum (circles with error bars) fitted with p model (continuous line), and with variant of p model (dashed line) where lengths are also unequal. Visual inspection shows asymmetric nature. To fit p model (continuous line), equal scales $l_1 = l_2 = 0.5$, and unequal probabilities, $p_1 + p_2 + dp = 1$ have considered. The p model fit parameters are $p_1 = 0.418, dp = 0.0$. These parameters give cascading probabilities and quantifies scaling of the multifractal spectrum. Value of p_1 and p_2 different than 0.5 substantiate the presence of the multifractality. In addition to the p model fit, its variant (dashed line) is obtained using the same formulations (equations 4.4 and 4.5) but with unequal scales, i.e, $l_1 \neq l_2$ and $l_1 + l_2 = 1$. The entire spectrum is fitted well with parameters $p_1 = 0.0785, l_1 = 0.12, dp = 0.005$. It is to note that with p model, the asymmetric spectrum is fitted only for the right part of the spectrum, i.e., for negative q, as the spectrum is so much left–skewed to not account for the dissipation factor. While its variant fits well with $dp > 0$ pointing to the intermittency in the series.

In addition to the visual inspection reported above, multifractal measures, $\Delta\alpha$ and A, computed using equations 3.15 and 3.16 are found to be 0.47 and 3.25 respectively. A high value of A ($A > 1$) indicates the spectrum to be left–skewed and reaffirms

the influence of larger fluctuations, agreeing with the $h(q)$ profile. The computed measures along with fit parameters are listed in Table 5.3. Considering the difference between the fit and fluctuation values, errors are calculated and shown for $h(q)$ and $\tau(q)$ profile, and for the multifractal spectrum.

Figure 5.4f shows multifractal spectra obtained by shuffling the time series (square marker) along with the original time series (circle marker). For shuffled time series, $h(q) = 1 \pm (0.03)$ infers long–range correlation and spectrum shows weak multifractality. The spectral width, $\Delta\alpha$, is found to be in the range $[0.05, 0.15]$ with average $h(q) \sim 1 \pm (0.052)$.

It is evident from the above discussion that the multifractal spectrum alone is sufficient to assess the multifractal nature, henceforth only multifractal spectrum is presented for the remaining seven heights in Figure 5.5.

- The multifractal spectrum corresponding to the mean height of 194.58 km (Figure 5.5a) is right–skewed with $A = 0.54$. It indicates the influence of negative moments, q, which characterize smaller fluctuations than the average. The width, $\Delta\alpha = 0.61$ is the highest among the analyzed series. The optimal p model fit is obtained by considering the dissipation factor which suggests intermittent behavior.

- The spectrum corresponding to the mean height of 214.64 km (Figure 5.5b) is slightly right–skewed with $A = 0.91$, which indicates the influence of negative moments, q, that infer the influence of smaller fluctuations than the average. An optimal p model fit is obtained accounting for dissipation factor which suggests intermittent behavior.

- The spectrum corresponding to the mean height of 219.19 km (Figure 5.5c) is slightly left–skewed with $A = 1.05$, which indicates the influence of positive moments, q, characterizing larger fluctuations than the average. An optimal p model fit is obtained considering the dissipation factor which suggests intermittent behavior.

- The spectrum corresponding to the mean height of 237.61 km (Figure 5.5d) is slightly right–skewed with $A = 0.94$. It indicates the influence of negative q, that infer the influence of fluctuations smaller than average. An optimal p model fit is obtained accounting for dissipation factor which suggests intermittent behavior.

- The spectrum corresponding to the mean height of 259.34 km (Figure 5.5e) is the most skewed on left among all the analyzed series, with $A = 5.51$. It indicates the influence of positive q, which characterizes larger fluctuations than the average. Spectrum is well fitted for negative q. The spectrum is so much left–skewed to not account for the dissipation factor.

- The spectrum corresponding to the mean height of 275.67 km (Figure 5.5f) is left–skewed with $A = 2.98$. It indicates the influence of positive q, which characterizes larger fluctuations than the average. An optimal p model fit is obtained accounting for dissipation factor which suggests intermittent behavior.

- Finally, the lower panel shows the multifractal spectrum corresponding to the mean height of 283.95 km (Figure 5.5g) is left–skewed with $A = 4.46$. It indicates the influence of positive q, infers the influence of larger fluctuations than the average. Spectrum is well fitted for negative q. The spectrum is so much left–skewed to not account for the dissipation factor.

All selected time series are shuffled randomly without repetition and subjected to the MFDFA. All shuffled series exhibit weaker multifractality. Thus, possible type of multifractality may be due to long–range correlations as well as to the broad probability density function. As an example, shuffled series and its corresponding multifractal spectrum for mean height 259.34 km is presented in appendix B (Figure B.2.

For all the chosen heights, range of $h(q)$ is found to be $0.83 < h(q) < 1.28$, which indicate a long–range correlation with persistent temporal fluctuations. Also, $h(q)$ profile decreases with respect to q, and $\tau(q)$ shows deviation from linearity confirming the multifractality in all the series. Deviation of $\tau(q)$ from linearity can be attributed to the nonlinear interactions among the scales (BISKAMP, 1993) and non–homogenous nature (MONIN; YAGLOM, 1975; FRISCH, 1995). Width of the multifractal spectra varies from 0.27 to 0.61, showing weaker to stronger multifractality. Higher values of α_0 (> 1) indicate the underlying process to be irregular (GHOSH et al., 2012; TANNA; PATHAK, 2014; MANDAL et al., 2017). The p model fit is obtained with parameter p other than 0.5. The p model fit parameter $0.36 < p < 0.44$ represents the energy transfer probability of the multiplicative cascade process with nonzero dissipation factor. Thus, these results confirm the presence of multifractality and intermittency in all the analyzed time series.

Figure 5.5 - MFDFA spectra: multifractal spectrum (circle marker with error bars) with p model fit (continuous line) for the mean heights of 194.58 (a), 214.64 (b), 219.19 (c), 237.61 (d), 259.34 (e), 275.67 (f), and 283.95 (e) km.

43
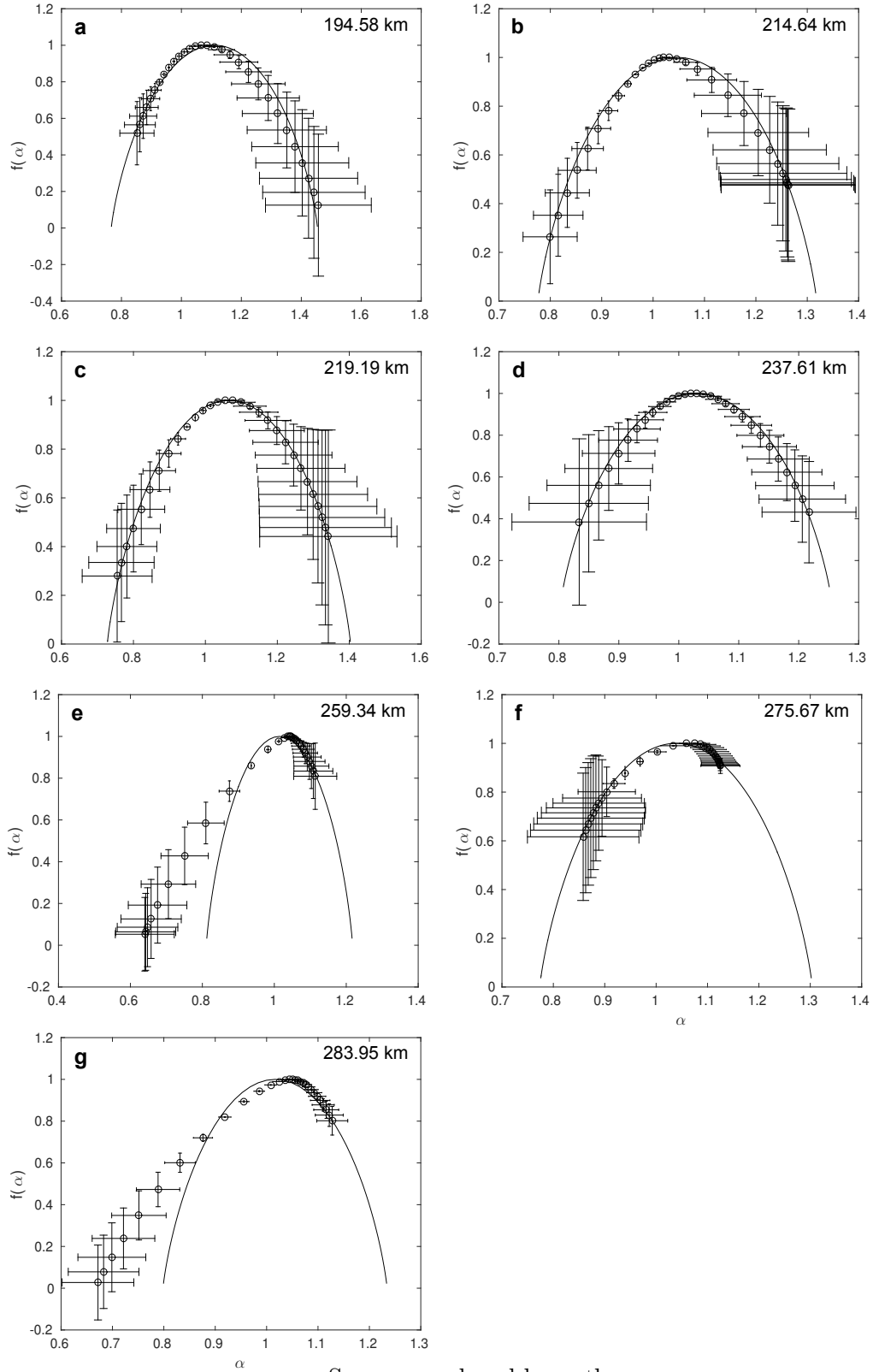
Table 5.3 - Multifractal analysis measures: For eight time series, mean heights are listed in first column, second column shows degree of multifractality ($\Delta\alpha$), third column gives the measure of asymmetry (A). Columns 4 to 6 lists the p model fit parameters, p_1, l_1, dp respectively. Seventh row is representing the p model fit parameters for time series of mean height of 263.47 km, considering the case when $l_1 \neq l_2$, $l_1 + l_2 = 1$ and $p_1 + p_2 + dp = 1$. The fit for this case is shown in Figure 5.4e.

$< height >$ (km)	degree of multifractality	measure of asymmetry	p model fit parameters		
	$\Delta\alpha$	A	p_1	l_1	dp
194.58	0.61	0.54	0.3650	0.5	0.0500
214.64	0.46	0.91	0.4010	0.5	0.0150
219.19	0.59	1.05	0.3780	0.5	0.0180
237.61	0.38	0.94	0.4190	0.5	0.0080
259.34	0.47	5.51	0.4300	0.5	0.0000
263.47	0.47	3.25	0.4180	0.5	0.0000
			0.0785	0.12	0.005
275.67	0.27	2.98	0.4050	0.5	0.0100
283.95	0.46	4.46	0.4250	0.5	0.0000

An interesting pattern in the asymmetry measure (Table 5.3) is observed in the present analysis. For the lowest height analyzed, 194.58 km, the spectrum is right–skewed with $A = 0.54$. For the next three analyzed heights 214.64, 219.19, and 237.61 km, those lying around the middle part of the valley region, the spectrum is very close to being symmetrical with $A = [0.91, 1.05]$. In the upper part of the region i.e., for the heights 259.34, 263.47, 275.67, and 283.95 km, the spectrum is highly left–skewed with $A = [2.98, 5.51]$ which quantify the intense fluctuations to be larger than average, and is evident of more non–homogeneous nature of electron density fluctuations. This transition of the spectrum from being symmetric to highly left–skewed, i.e., transition of the influence from smaller scales to larger scales, is intriguing given that the upper heights considered lie close to the base of the F region.

Figure 5.6 - Variation of the mean density and the degree of multifractality for the selected eight time series. The density is shown in dark grey color bars on the left and $\Delta\alpha$ in light grey colored bars on the right. The mean heights corresponding to the selected eight time series are shown next to the bars.
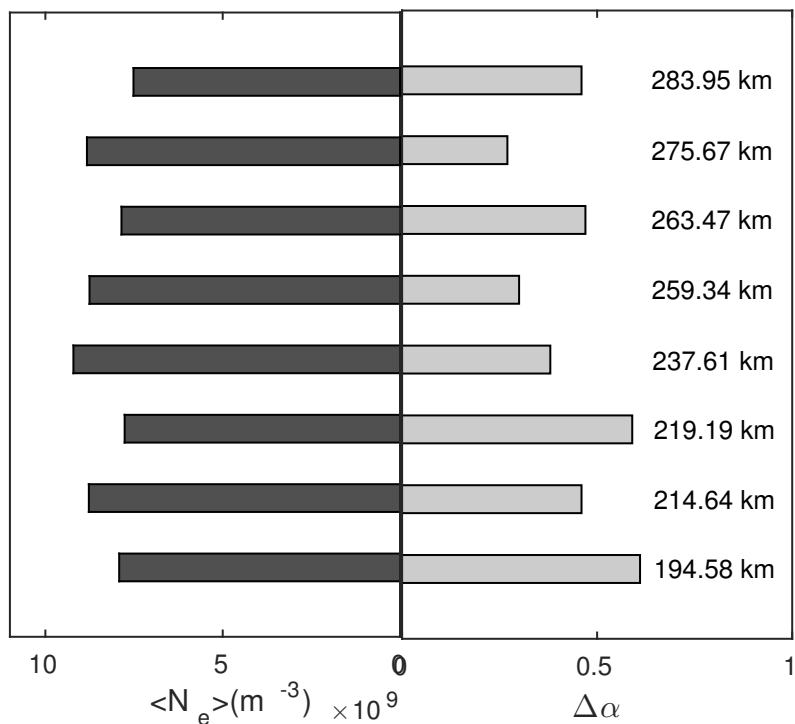
Source: produced by author.

Finally, a relation is reported between the density and a multifractal measure for the analyzed time series. Figure 5.6 shows the relation between the variation of mean density (left) and multifractal width, $\Delta\alpha$, (right). It can be observed that for variation in density, the corresponding $\Delta\alpha$ show an inverse relation except for the time series at a mean height of 259.34 km. Low density resembles with more complex behavior in terms of larger multifractal width. This inverse relation between mean density and multifractal width is consequential and evident that a more complex structure shows more richness of scaling. Multifractal analysis of medium–to–large irregularities in the low latitude equatorial F region (mean height of 264 to 430 km) obtained from another rocket experiment from the same station (presented in the next section) has shown similar inverse relation between mean density and multifractal width (JOSHI et al., 2020). This reported reciprocity in the *insitu* data is obtained from an equatorial low latitude station. More data has to be analyzed

from different latitudes and altitudes to consolidate this relation and to comment on any physical approach.

Figure 5.7 - The model predicting the variations in the mean density with respect to $\Delta\alpha$ for this rocket experiment. Variation of mean density is shown in the left part and of $\Delta\alpha$ in the right part as a curve line. Bands along the central curve represent the standard deviation for all points in the model.
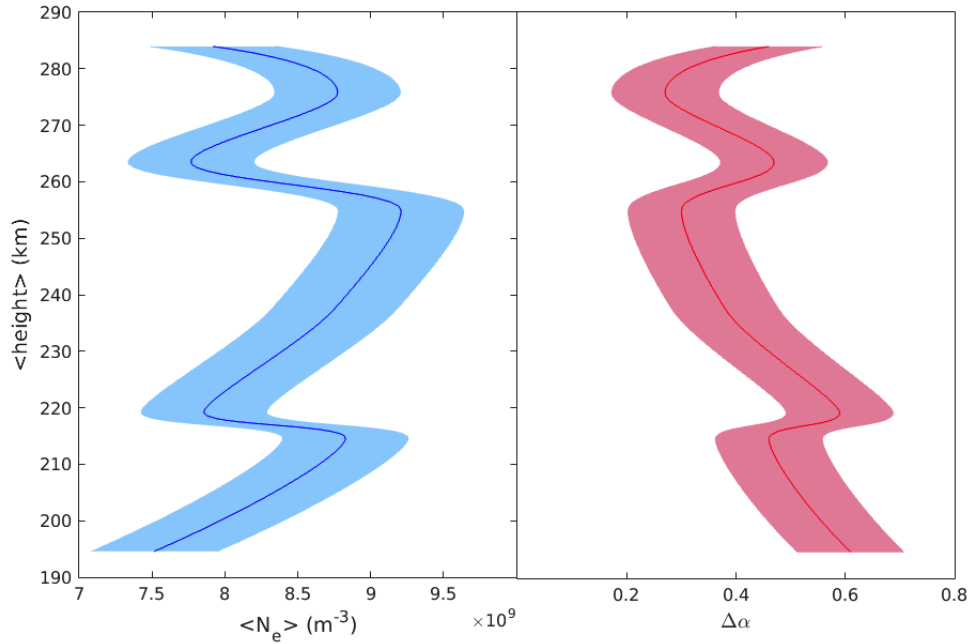
After presenting a variation between the mean density and the multifractal width in the Figure 5.6, this study is extended to derive a model by interpolating these data (mean density and $\Delta\alpha$) with piecewise cubic Hermite interpolating polynomial (PCHIP) to get smooth appearance and it is presented in the Figure 5.7. Variation of mean density is shown in the left part and of $\Delta\alpha$ in the right part as a curve line. Bands along the central curve represent the standard deviation for all points in the model. The derived model predicts the variations in the mean density with respect to $\Delta\alpha$ for this rocket experiment performed. It is valid in a scenario if continuous values of mean density and its fluctuations would have been obtained.

5.2 Analysis of the F region irregularities

5.2.1 Data

A Brazilian made SONDA III rocket was launched from the equatorial rocket launching station Alcântara $(2.31°S; 44.4°W)$ on December 18th, 1995 at 2117 h (LT) as a part of the IONEX II operation. The objective of this rocket launch was to study the behavior of night time F region under conditions favorable for the development of the plasma bubbles and to explore the characteristic features of plasma density fluctuations associated with them (MURALIKRISHNA et al., 2003; MURALIKRISHNA; ABDU, 2006). The rocket reached an apogee at altitude ~ 557 km covering a horizontal range of 589 km during ~ 11 min flight. In the upleg profile (ascent of the rocket), the F region base is clearly observed around 300 km, but without any large scale depletion or bubble. On the other hand, several plasma bubbles of medium–large scale were observed in the downleg profile (descent of the rocket), around the base of F region and also topside of it, but without any sharp indication of the F region base from altitude above 240 km. Rocket traversed through regions of different altitudes, separated by a few hundred of kilometers during upleg and downleg, so this might elucidate the large differences observed in ascent and descent of the rocket (MURALIKRISHNA et al., 2003; MURALIKRISHNA; ABDU, 2006; MURALIKRISHNA; VIEIRA, 2007).

The rocket carried on board electric field double probe and Langmuir Probe (LP) which provided simultaneous measurements of the height variations of electric field and electron density (MURALIKRISHNA et al., 2003). Low frequency sampled data from LP is used to show electron density profile plot. A detailed explanation of *in situ* experiment is found in Muralikrishna et al. (2003), Muralikrishna and Abdu (2006), Muralikrishna and Vieira (2007), Fornari (2016).

5.2.2 MFDFA of the F region data

Muralikrishna et al. (2003) have analyzed this *in situ* data using PSD method. Some of the key results are: (1) the initiation of a cascade process, owing to Rayleigh–Taylor instability mechanism, near the base of F region resulted in the development of the plasma bubbles or large scale irregularities, and (2) subsequently, when energy was advected to higher altitudes, smaller scale irregularities were observed, owing to cross–field instability mechanism (MURALIKRISHNA et al., 2003; MURALIKRISHNA; ABDU, 2006; MURALIKRISHNA; VIEIRA, 2007). In this scenario, it will be interesting to investigate the scaling properties of the F region irregularities with the MFDFA

and validating with the p model. Hence, six time series of electric field fluctuations from the F region are selected corresponding to the mean heights of 264.58, 270.22, 292.37, 324.00, 358.56, and 429.65 km from the downleg trajectory of the rocket.

Figure 5.8 - Comprehensive MFDFA result: (a) the time series at mean height 324.00 km (b) $h(q)$ vs q profile. (c) $\tau(q)$ vs q profile along with dashed line which represents a linear relationship between $\tau(q)$ and q (d) the multifractal spectrum (circle marker with error bars) fitted with the p model (continuous line).
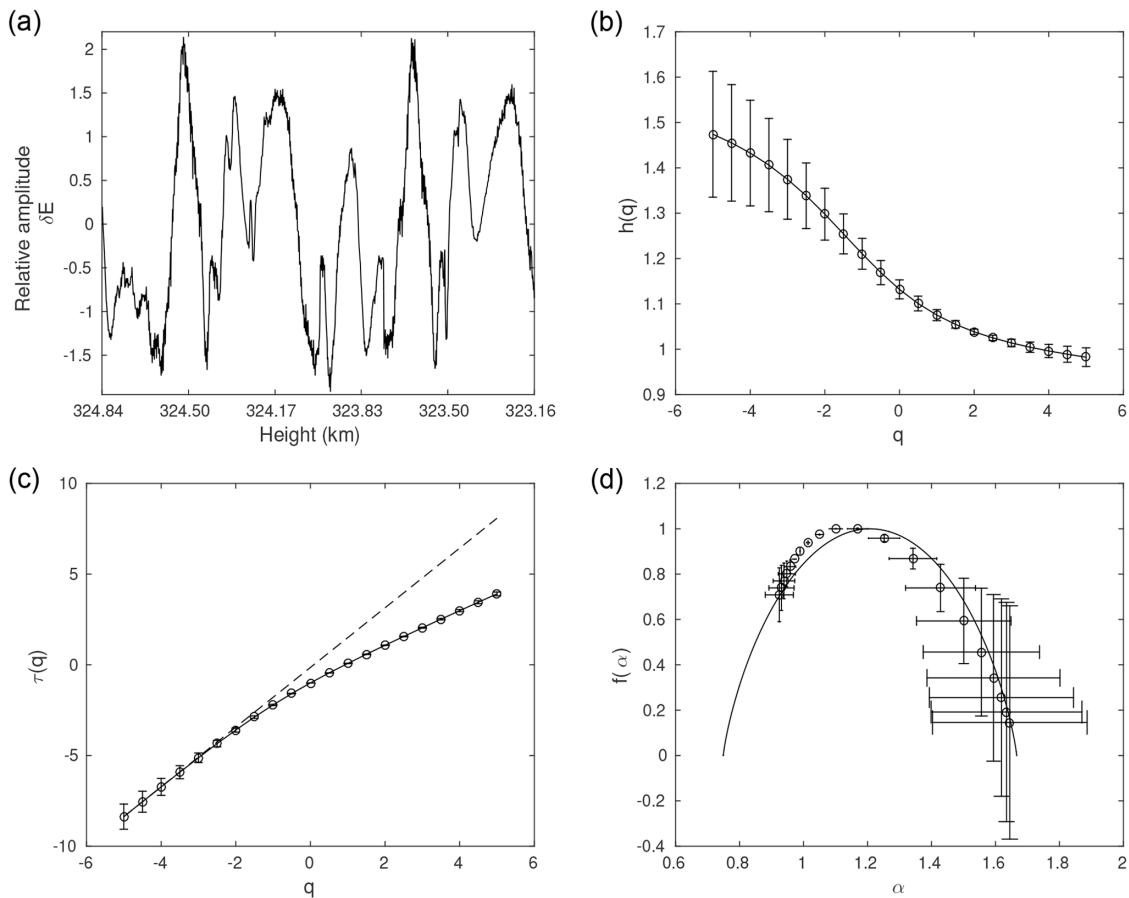
Source: produced by author.

Figure 5.8 shows a detailed multifractal analysis of a time series corresponding to the mean height of 324.00 km (5.8a). Figure 5.8b presents the $h(q)$ profile and Figure 5.8c presents $\tau(q)$ profile. The corresponding multifractal spectrum is shown in the Figure 5.8d. The spectrum is right–skewed, indicating the influence of the negative values of q on the time series. It is evident as well from the $h(q)$ profile as

48

the variation of $h(q)$ for negative q is observed to be comparatively steep. The plot for $\tau(q)$ versus q shows marked deviation from linearity, asserting presence of the multifractality in time series for the chosen height.

In addition to the derived inferences from the visual analysis of the multifractal spectrum reported above, multifractal measures, $\Delta\alpha$ and A can be quantified (equations 3.15 and 3.16). Measure $A = 0.32$ quantifies the skewness while $\Delta\alpha = 0.72$ infers the strength of multifractality. These two measures are listed in Table 5.4. Lastly, the multifractal spectrum is fitted with the p model (shown with a continuous line), where the fragment lengths are equal i.e., $l_1 = l_2 = 0.5$ and the weights, p_1 and p_2, are varied such that $p_1 + p_2 \leq 1$. Nevertheless, loss in p parameter had to be accounted to obtain an optimal fit. The loss factor, dp, signifies nonconservative energy distribution i.e., a dissipative energy cascading process in the inertial range. The p model fit parameters are $p_1 = 0.315$ and $dp = 0.090$ and are listed in Table 5.4.

It is seen from the above discussion that the multifractal spectrum is sufficient to assess the multifractal nature, henceforth the time series and the corresponding multifractal spectrum have shown for the remaining chosen heights. Figure 5.9 shows the time series selected from the F region in the left panel and the corresponding multifractal spectrum in the right panel.

- For the time series corresponding to the mean height of 264.58 km, the multifractal spectrum is slightly right–skewed, which can be inferred from measure $A = 0.82$. It indicates the influence of negative moments, q, which characterizes the influence of smaller fluctuations than the average. Degree of multifractality, $\Delta\alpha = 0.53$. The optimal p model fit is obtained with parameters $p_1 = 0.364$ and $dp = 0.059$.

- For the time series corresponding to the mean height of 270.22 km, the multifractal spectrum is slightly left–skewed, which can be inferred from measure $A = 1.11$. It indicates the influence of positive moments, q, which characterize intense larger fluctuations than the average. Degree of multifractality, $\Delta\alpha = 0.82$. The optimal p model fit is obtained with parameters $p_1 = 0.34$ and $dp = 0.065$.

- For the time series corresponding to the mean height of 292.37 km, the multifractal spectrum is left–skewed, reflected from the measure $A = 2.99$. It indicates the influence of positive moments, q, which characterize intense

larger fluctuations than the average. Degree of multifractality, $\Delta\alpha = 0.93$. The optimal p model fit obtained with parameters $p_1 = 0.339$ and $dp = 0.02$. The spectrum is fitted for the positive values of q.

- For the time series corresponding to the mean height of 358.56 km, the multifractal spectrum is right–skewed, reflected from the measure $A = 0.37$. It indicates the influence of negative moments, q, which characterize the influence of smaller fluctuations than the average. Degree of multifractality, $\Delta\alpha = 0.52$. The optimal p model fit obtained with parameters $p_1 = 0.36$ and $dp = 0.07$.

- For the time series corresponding to the mean height of 429.65 km, the multifractal spectrum is right–skewed, also reflected from the measure $A = 0.51$. It indicates the influence of negative moments, q, which characterize the influence of smaller fluctuations than the average. Degree of multifractality is $\Delta\alpha = 0.28$. The optimal p model fit obtained with parameters $p_1 = 0.399$ and $dp = 0.0355$.

All selected time series are shuffled randomly without repetition and subjected to the MFDFA. All shuffled series exhibit weaker multifractality. Thus, possible type of multifractality may be due to long–range correlations as well as to the broad probability density function. As an example, shuffled series and its corresponding multifractal spectrum for mean height 292.37 km is presented in appendix B (Figure B.3.

Table 5.4 - Multifractal analysis measures: For the time series at mean heights listed in the first column, the second column shows the degree of multifractality ($\Delta\alpha$), the third column gives measure of asymmetry (A). Columns 4 to 6 lists the p model fit parameters, l_1, p_1, dp respectively.

$< height >$ (km)	degree of multifractality $\Delta\alpha$	measure of asymmetry A	p model fit parameters		
			l_1	p_1	dp
264.58	0.53	0.82	0.5	0.364	0.059
270.22	0.82	1.11	0.5	0.340	0.065
292.37	0.93	2.99	0.5	0.339	0.02
324.00	0.72	0.32	0.5	0.315	0.090
358.56	0.52	0.37	0.5	0.360	0.070
429.65	0.28	0.51	0.5	0.399	0.0355

Figure 5.9 - MFDFA for the first experiment: top to bottom panel shows the time series and its corresponding multifractal spectrum with the p model fit (continuous line) for the mean heights of $264.58, 270.22, 292.37, 358.56$ and 429.65 km respectively.
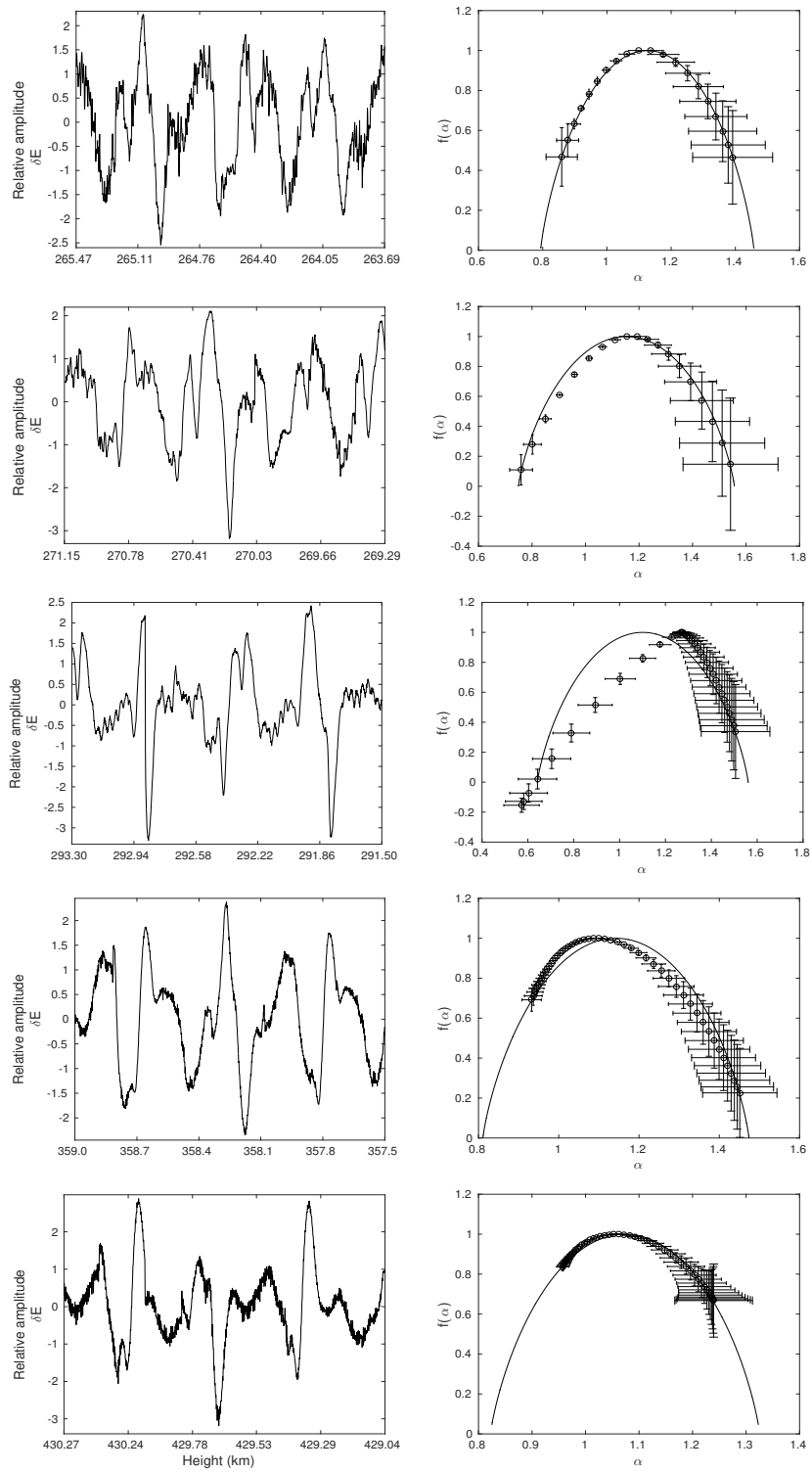
Source: produced by author.

Figure 5.10 - Variation of the mean density and the degree of multifractality with the mean height for the six selected time series from the first experiment in a 3-D plane. In the inset, these variations are shown in a 2-D plane of the mean density (left) and the degree of multifractality (right).
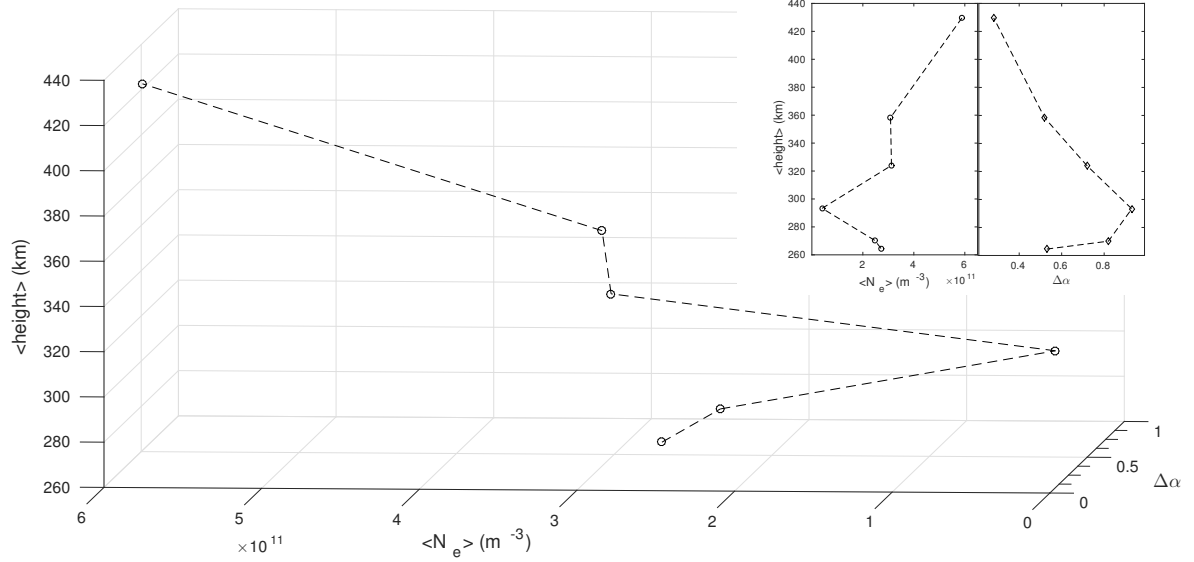
Source: produced by author.

Figure 5.10 shows a variation of mean density and multifractal width, $\Delta\alpha$ with mean heights for the selected six time series on a 3-dimensional plane. The presence of a plasma bubble characterized by large scale irregularities, which in turn is reflected in the low density, is observed around a mean height of 292.37 km. Contrarily, stronger multifractality is observed at this height. This inverse variation is in agreement with the turbulent like multiplicative cascade process. On the other hand, as the rocket traversed higher altitudes, the mean density increased while the multifractality became weaker. This suggests that the cascading process resulted in smaller scale irregularities by dissipating energy. Two dimensional plots showing the variation of mean density and $\Delta\alpha$ with mean heights are shown in the inset of Figure 5.10.

5.3 Type I solar noise storm analysis

This section presents multifractal analysis of solar type I noise storm data obtained from the e-Callisto radio spectrometer, using the MFDFA and multicascade p model to characterize their intermittent multitude behavior.

5.3.1 E-Callisto radio spectrometer

E-Callisto is the network of the compact astronomical low–cost low–frequency instrument for spectroscopy and transportable observatory (CALLISTO) type radio spectrometers to monitor the solar activity in metric wavelength band, which is distributed at various locations around the globe. The Callisto provides high resolution spectrum as it can work in 45 to 870 MHz frequency range with step of 62.5 kHz. The Callisto instrument can be operated and controlled remotely. Collected and calibrated data pertaining to solar radio event are stored into a structured archive in a central data base which can be accessed freely at `http://www.e-callisto.org/Data/data.html`. Data for 15 min observation is available in Flexible Image Transport System (FITS) file format. Corresponding spectrogram is available in Portable Network Graphics (PNG) file format. Intense emissions to no emissions are represented by bright to black color (BENZ et al., 2009). The e-Callisto system is acknowledged by world–wide researchers as its high resolution data unveil substantial new information to study solar activity and space weather, for example: (BENZ et al., 2009; SODRÉ et al., 2015; ZAVVARI et al., 2016; LI et al., 2017; HAMIDI; SHARIFF, 2018; SODRÉ et al., 2019).

5.3.2 Data

BLEN7M spectrograph is located in Switzerland, integrated with the e-Callisto network and operates in the range 110–870 MHz. Out of 200 channels, data is selected based on maximum intensity, canonical pattern for type I burst and noise, and space weather report generated by NOAA, confirming the occurrence of radio noise storm events. This selection analysis is done by Cintra (2018). Eight time series of frequency 263.3 MHz, of solar emissions associated with type I noise storm, recorded on July 30, 2011, by the BLEN7M spectrograph of the e-Callisto network. All time series are of 15 minutes duration.

An event occurred between 04:58 UT and 07:32 UT, corresponding 5 data files are recorded between 05:45 to 7:00 UT. For another event occurred between 09:51 and 12:24 UT, corresponding 3 data files are recorded at 10:00, 11:00 and 11:45 UT

respectively. Time series is shown as intensity in dB on ordinate and time in UT on abscissa in Figure 5.12.

5.3.3 Results

Analysis using the MFDFA are presented in the Figures 5.11, 5.12, & 5.13 and summarized in the Table 5.5.

Figure 5.11 - Comprehensive MFDFA result for the time series recorded between 6:30 and 6:45 UT: (a) fluctuation profile with linear fit for $q = [-5, -3, -1, +1, +3, +5]$ (b) $h(q)$ vs q profile. (c) $\tau(q)$ vs q profile along with dashed line which represents a linear relationship between $\tau(q)$ and q (d) the multifractal spectrum (circle marker with error bars) fitted with the p model (continuous line).
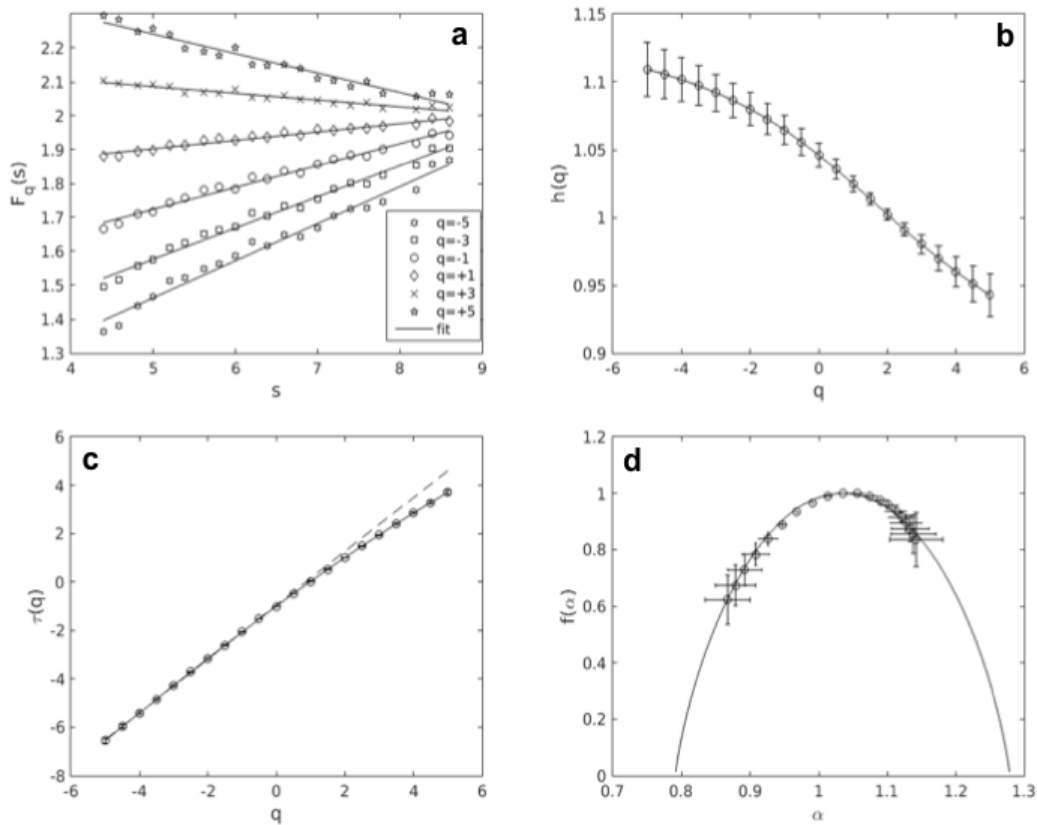
Source: produced by author.

Figure 5.11 shows a detailed multifractal analysis of a time series recorded between

54

6:30 and 6:45 UT (shown in Figure 5.12). Panel a shows the fluctuation profile with linear fit for $q = [-5, -3, -1, +1, +3, +5]$. The fluctuation profile shows spread at lower scales and converges at higher scales, thus affirming the multifractality in the series. Panel b presents the $h(q)$ profile which decreases with q, thus affirming the multifractality in the series. Panel c presents $\tau(q)$ profile along with dashed line which represents a linear relationship between $\tau(q)$ and q. This plot shows marked deviation from linearity, asserting presence of the multifractality in time series. The corresponding multifractal spectrum is shown in the panel d. The spectrum is left–skewed, indicating the influence of the positive values of q on the time series. It is evident as well from the $h(q)$ profile as the variation of $h(q)$ for positive q is observed to be comparatively steep.

In addition to the derived inferences from the visual analysis of the multifractal spectrum reported above, multifractal measures, $\Delta\alpha$ and A are quantified (equations 3.15 and 3.16) and support the inferences from visual analysis. Measure $\Delta\alpha = 0.28$ infers the strength of multifractality while $A = 1.70$ quantifies the skewness. These two measures are listed in Table 5.5. Lastly, the multifractal spectrum is fitted with the p model (shown with a continuous line), where the fragment lengths are equal i.e., $l_1 = l_2 = 0.5$ and the weights, p_1 and p_2, are varied such that $p_1 + p_2 \leq 1$. Nevertheless, loss in p parameter had to be accounted to obtain an optimal fit. The loss factor, dp, signifies nonconservative energy distribution i.e., a dissipative energy cascading process in the inertial range. The p model fit parameters are $p_1 = 0.412$ and $dp = 0.001$. The p model fit parameters are listed in Table 5.5.

To find the source of multifractality, all the series are shuffled and subjected to the MFDFA. Shuffled series exhibit multifractality. Thus, possible type of multifractality may be due to a broad probability density function. As an example, shuffled series and its corresponding multifractal spectrum for series recorded between 06:45 and 07:00 UT is presented in appendix B (Figure B.4.

It is seen from the above discussion that the multifractal spectrum is sufficient to assess the multifractal nature, henceforth the time series and the corresponding multifractal spectrum have shown for the remaining chosen series. In Figure 5.12, the left side (1st and 3rd columns) show time series and corresponding multifractal spectrum on the right side (2nd and 4th columns). The p model fit is shown by continuous line.

For time series recorded at 5:45 UT, multifractal spectrum is symmetrical as $A = 1$, which indicates equal influence of high and low fractal exponents. Its degree of

multifractality is $\Delta\alpha = 0.18$. Left–skewed spectrum is observed for the time series recorded at 6:00, 6:15, 6:30, 6:45, and 10:00 UT with $A = 1.31$, $A = 1.33$, $A = 1.70$, $A = 2.00$ and $A = 1.75$ respectively, indicating the influence of high fractal exponents. Degree of multifractality obtained as $\Delta\alpha = 0.38$, $\Delta\alpha = 0.21$, $\Delta\alpha = 0.28$, $\Delta\alpha = 0.30$, and $\Delta\alpha = 0.33$ respectively. For the last two series recorded at 11:00 and 11:45 UT spectrum is right–skewed with $A = 0.50$ and $A = 0.41$ which indicates influence of low fractal exponents. Degree of multifractality is obtained as $\Delta\alpha = 0.25$ and $\Delta\alpha = 0.53$ respectively.

E-Callisto network records data for every 15 minutes. First five time series, corresponding to the first event are continuous in time, thus merging these first five times series recorded between 05:45 and 7:00 UT is analysed and result is presented in Figure 5.13. Multifractal spectrum is left–skewed with $A = 1.73$, indicating the influence of larger fluctuations. Degree of multifractality obtained as $\Delta\alpha = 0.33$. The spectrum is so left skewed that optimal p model fit is obtained only for negative q with parameters $p_1 = 0.434$ and $l_1 = 0.5$. These values along with multifractal measures are listed in a Table 5.5.

Figure 5.13 - Left side shows a time series recorded between 05:45 and 07:00 UT (data 1 to data 5). Right side shows corresponding multifractal spectrum ($\circ$) and p model fit (continuous line).
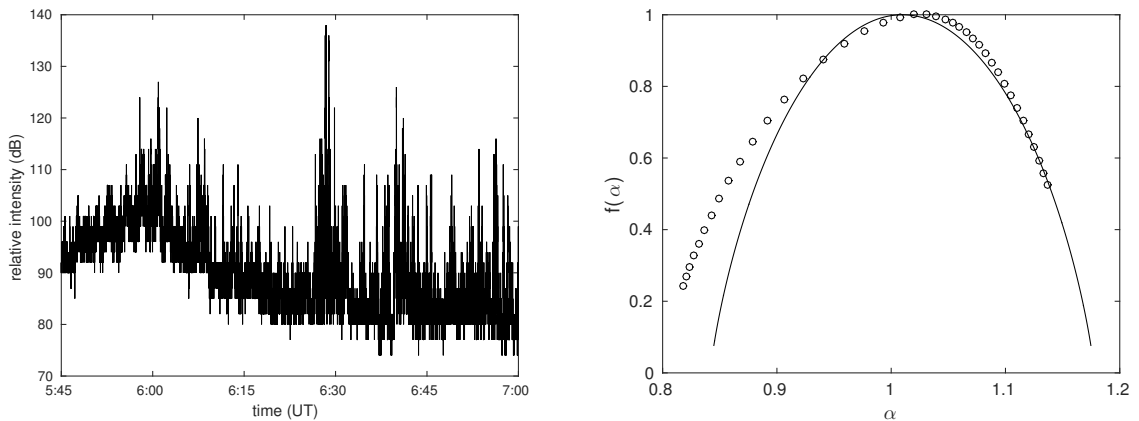
Source: produced by author.

All time series show multifractality and is confirmed, as the p model fit probability

Figure 5.12 - MFDFA and p model fit for eight time series of type I noise storm. Left
side (1st and 3rd columns) show time series and corresponding multifractal
spectrum on the right side (2nd and 4th columns) with circle marker with
error bars. The p model fit is shown by continuous line.

57
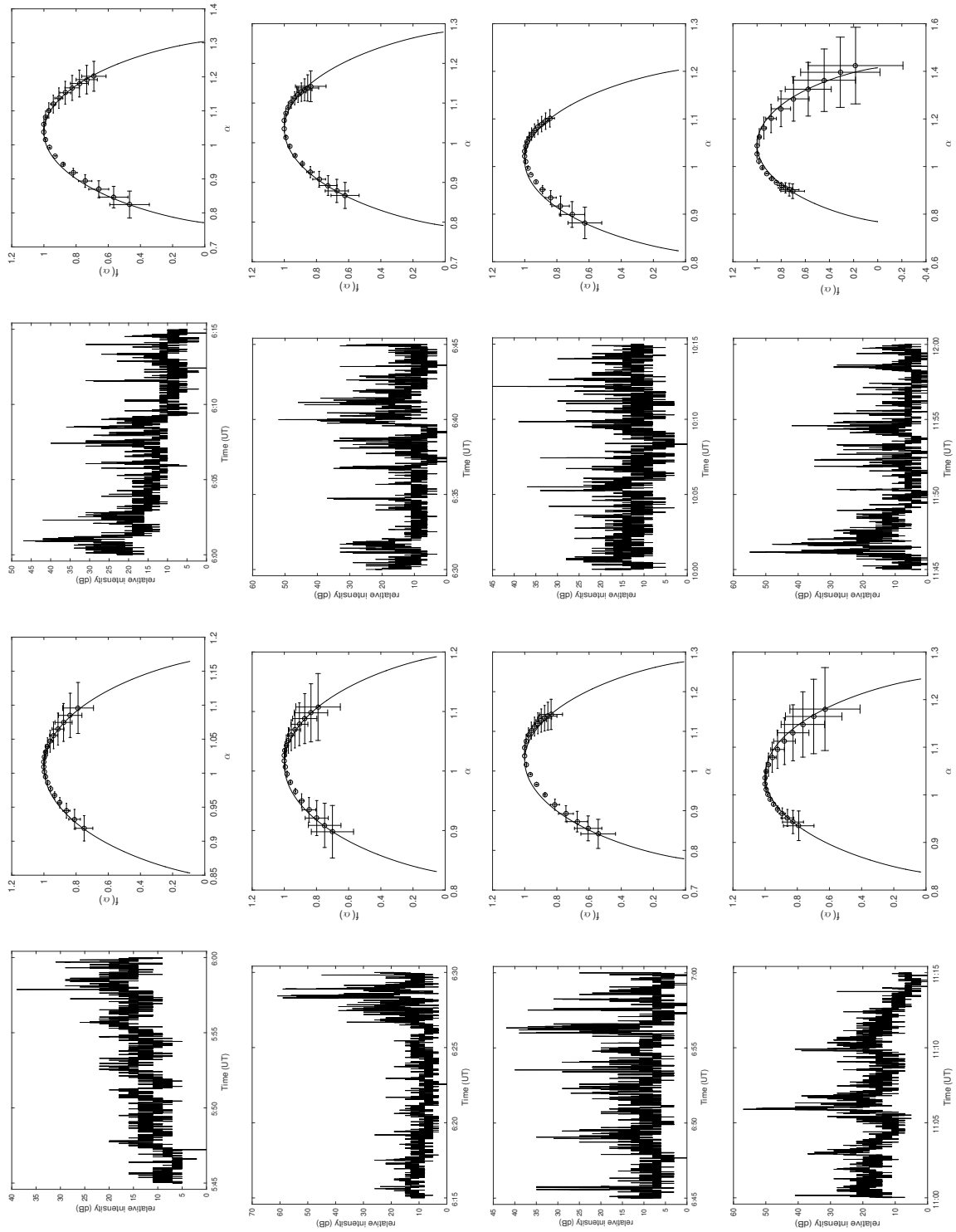
Table 5.5 - Multifractal analysis measures: For the eight time series listed in the first column, start and end time of the corresponding series are listed in the second and third columns. Forth and fifth column list the p model fit parameters, p_1 and dp respectively. Sixth column lists degree of multifractality ($\Delta\alpha$) and last column lists asymmetry measure A.

Data	start time (UT)	end time	p_1	dp	$\Delta\alpha$	A
data 1	05:45	06:00	0.445	0.000	0.18	1.00
data 2	06:00	06:15	0.405	0.009	0.38	1.31
data 3	06:15	06:30	0.437	0.000	0.21	1.33
data 4	06:30	06:45	0.412	0.001	0.28	1.70
data 5	06:45	07:00	0.413	0.004	0.30	2.00
data 1-5	05:45	07:00	0.442	0.000	0.32	1.73
data 6	10:00	10:15	0.434	0.000	0.33	1.75
data 7	11:00	11:15	0.422	0.018	0.25	0.50
data 8	11:45	12:00	0.375	0.038	0.53	0.41

parameter differ from 0.5. Also, necessity of dp parameter in the p model fit affirms intermittency in the data. Type I noise storm data obtained between 11:45 and 12:00 UT has maximum spectrum width, $\Delta\alpha = 0.53$ whereas data recorded between 05:45 and 06:00 UT has the least multifractal width, $\Delta\alpha = 0.18$. Probability parameter varies in a range of $0.375 < p < 0.445$ to fit the p model.

Comparing the spectra for time series recorded between 05:45 and 07:00 in Figure 5.12 with Figure 5.13 where these five time series are merged, confirm that the first event is characterized by larger fluctuations ($A > 1$).

The current finding is in agreement with the previous work done by Cintra (2018), Sodré et al. (2019) where authors found these type I noise series to be turbulent in nature and also with Veronig et al. (2000) where authors confirmed the nonlinearity in the type I noise storm data. Optimal p model fit affirms the turbulent and multifractal nature of type I noise storm series and p model parameters quantify the energy cascade process.

5.4 Modeling endogenous and exogenous noise

The techniques explored in this thesis have versatile applications. Multiplicative cascade process do allow to construct time series with the desired properties. In this analysis, the p model is explored to model the endogenous and exogenous noise to study extreme event like *international armed conflict*. Armed conflicts (AC) continues to be a rising concern as they catastrophically affect the world in various spheres like economical, social, geographical etc. Analysis of the AC dataset and the underlying patterns can provide a benchmark to understand the international geopolitical affairs, evolving complex equations among different states and changing policies.

In a time series, internal perturbations give rise to endogenous shocks characterized by smoother continuous fluctuations on both sides of the peak that increases slowly and after reaching its highest peak, gradually reduces by itself. On the other hand, exogenous shock results from an external perturbation and can be characterized by a sudden peak followed by unexpected rapid drop in the fluctuations. Around the peak very less continuous fluctuations can be observed.

Sornette et al. (2004) demonstrated a way to characterize endogenous and exogenous fluctuations in a non–physical system (book sale ranking on Amazon website). Authors considered sale of two books – one driven by a propaganda (exogenous) and the other by reviews (endogenous). Irrespective of the nature of sales, it is similar to the cascade process where first generation of buyers do influence on subsequent generations of buyers. Endogenous fluctuations were found to follow PSD exponent of 0.4 while exogenous fluctuations were found to follow PSD exponent of 0.7.

5.4.1 Armed conflict data

Centre for the study of civil wars, international peace research institute at Oslo (PRIO) and uppsala conflict data program (UCDP) at the department of peace and conflict research, uppsala university prepared, in collaboration, a dataset of armed conflicts. Uppsala database provides one of the most accurate and extensive information on ACs including attributes like conflict intensity based on total number of battle–related deaths; conflict type whether internal or external to the state; details of warring party including geographical information; conflict period with specific start and end date etc. The database is updated annually and considered a well–used data–sources on global armed conflicts. Its definition of armed conflict is becoming a standard in how conflicts are systematically defined and studied.

According to UCDP, armed conflict is defined as: a contested incompatibility that concerns government and/or territory where the use of armed force between two parties, of which at least one is the government of a state, results in at least 25 battle-related deaths. Uppsala categorizes AC in different intensity levels based on the total battle–related causalities:

- *Not active*: less than 25 battle–related deaths per year.

- *Minor*: at least 25 battle–related deaths per year but fewer than in the conflict period.

- *Intermediate*: at least 25 battle–related deaths per year and total accumulated of at least 1000 deaths, but fewer than 1000 in any given year.

- *War*: at least 1000 battle–related deaths per year.

5.4.2   Categorization of the AC database

Looking through current international affairs and conflicts in the AC dataset, a new scheme has designed to understand conflict intensity based on causalities. International AC data when plotted on semilog-y scale (Figure 5.14), shows four distinct levels which can be categorized as:

- *stability*: battle related deaths are approximately 10^2 on log scale. It has almost no fluctuation, continuous smooth unit vector.

- *conflicts*: battle related deaths are more than 10^2 but maximum 10^3 on log scale. This is interpreted as one of the party having conflicts with the other involved in the battle. But there was no use of any missiles or nuclear weapons nor threats.

- *cold war*: battle related deaths are more than 10^3 but maximum 10^4 on log scale. One of the party threatens the other party followed by attacks. High production and large number of nuclear weapons test but none of the party uses missiles and/or nuclear weapons.

- *warm war*: battle related deaths are more than 10^4 on log scale. One of the party uses the missiles and/or nuclear weapons. Threats of the use of nuclear weapons is high.

Figure 5.14 - Armed conflict data with distinct levels: stability, conflicts, cold war, warm war, hot war.
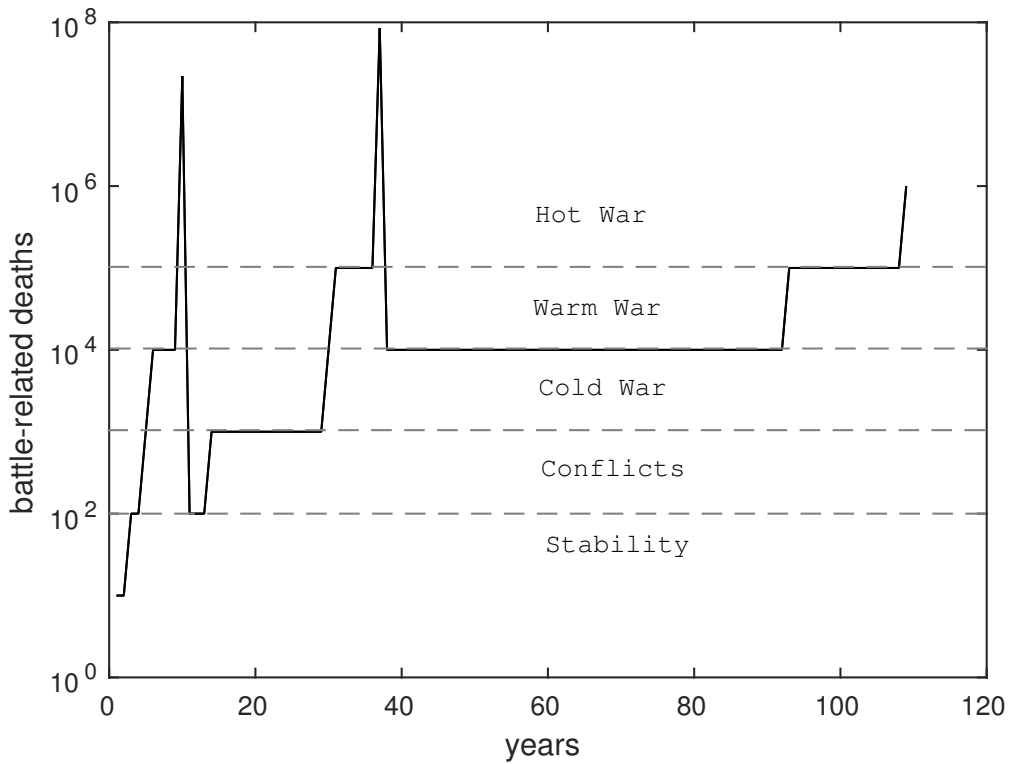
Source: produced by author.

- *war or hot war*: battle related deaths are more than 10^5 on log scale. Both parties use the missiles and/or nuclear weapons.

Inspecting a cause of a conflict, the focus is on determining whether internal or external factors play a role, in other words, is it endogenous or requires some thrust and be categorized as exogenous? To analyze endogeneity and exogeneity in AC, a model has been built by inducing endogenous and exogenous p model time series as a noise.

5.4.3 Building a model for AC

Figure 5.15 shows how different values of p describe the nature of the time series. Each panel shows the value of p and PSD exponent β used to generate time series. p values are varied from 0.1 to 0.9 except 0.5 and β value used are 0.4 and 0.7 for all eight values of p. Endogenous nature can be observed prominently in time series generated with p values 0.4 and 0.6 whereas exogenous nature can be seen prominently in time series generated with p values 0.1 and 0.9. These time series are generated using the algorithm given by Venema (UNIVERSITY OF BONN, ; DAVIS et al., 1997) where PSD exponent is also one of the input parameter along with p value.

Figure 5.15 - different p value describe different nature of time series. Each panel shows the value of p and β used to generate time series.
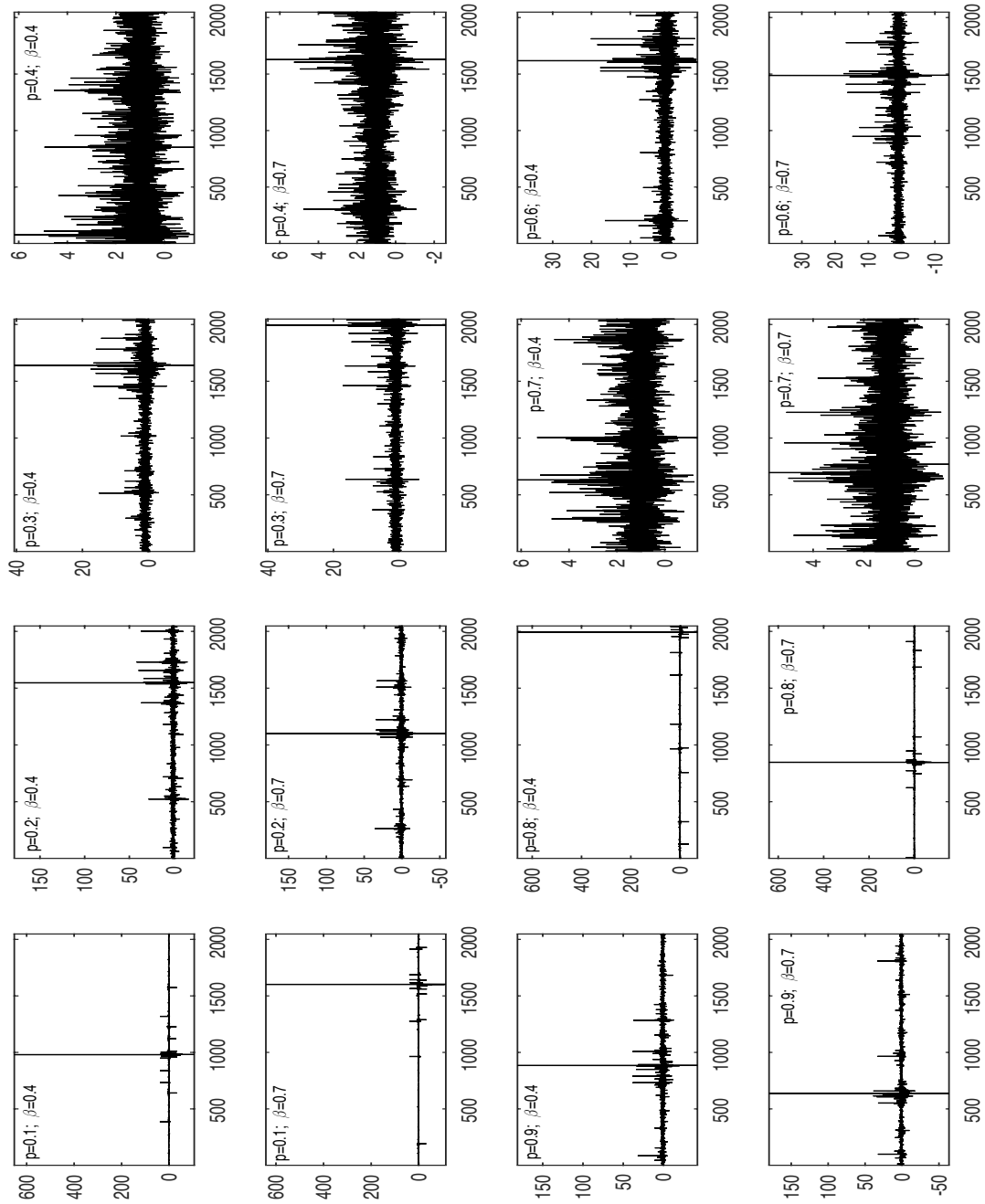
Figure 5.16 - Panels: (a) endogenous p model time series with $p_1 = 0.6$ and $\beta = -0.4$ (b) exogenous p model time series with $p_1 = 0.75$ and $\beta = -0.7$.
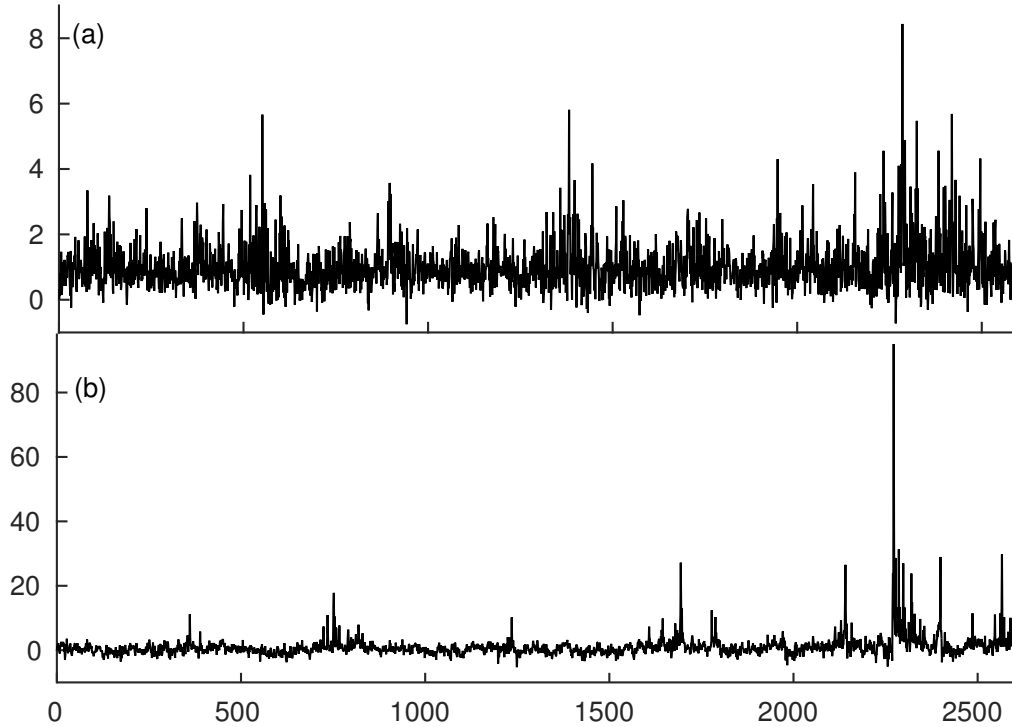
Source: produced by author.

The AC is an annually aggregated global database that records the total deaths that occurred in conflicts. The data is resampled from the original 109 points to 2592 points with a bimonthly resampling. Resampled time series also exhibits the distinct levels similar to the original data. Utilizing the PSD exponent values 0.4 and 0.7 along with proper p values 0.6 and 0.75, endogenous and exogenous time series are generated respectively (Figure 5.16).

Knowing the length of the signal at different levels, endogenous and exogenous time series resampled at those lengths are then multiplied by different multipliers and added to the resampled AC signal as a noise. Multipliers for different levels are: 10^1 for stability; 10^2 for conflict; 10^3 for cold war; and 10^4 for warm war.

Figure 5.17 - Panels: (a) resampled AC time series (b) resampled AC time series with
  endogenous noise (c) resampled AC time series with exogenous noise. Years
  shown for all three panels are correspond to the first world war at 1918, the
  second world war at 1945, 9/11 attack in 2001 and USA missile launch on
  Syria in 2017.
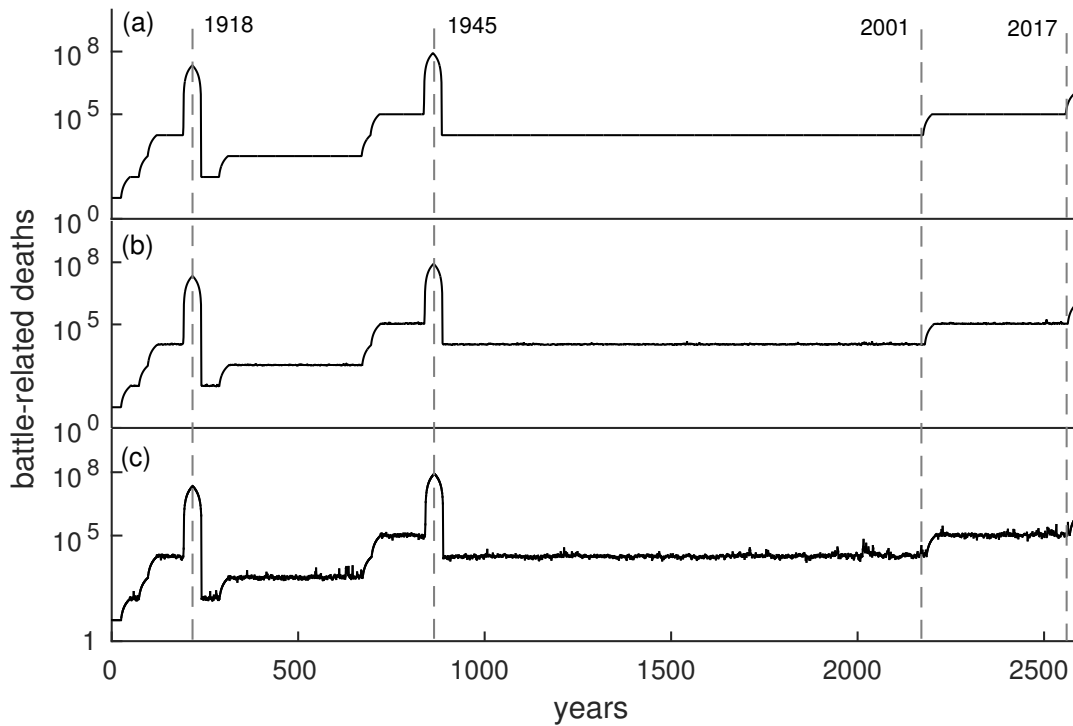
Source: produced by author.

Figure 5.17 shows the AC model. Panel a shows resampled AC series. Panel b shows
AC series with endogenous noise and panel c shows AC series with exogenous noise.
Exogenous noise added series has sudden peaks but before and after shows contin-
uous fluctuations, thus, suggesting endogenous nature.

Roberts and Turcotte (1998) explored fractal behavior of war intensity in terms
of battle–related deaths and found it exhibits long–range correlation. The current
work explores conflict intensity in terms of battle–related deaths. Endogenous and
exogenous noise added armed conflict resampled time series are subjected to the DFA
(Figure 5.18). Results show long–range correlation and in agreement with previous
results. Also, results confirm the robustness of the DFA method against noise as

fluctuation functions for both noise induced time series are overlapped.

Figure 5.18 - Armed conflict resampled time series with induced endogenous and exoge-
nous noise are subjected to the DFA. Results show long–range correlation
and also confirms the robustness of the DFA method against noise as fluc-
tuation functions for both noise induced time series are overlapped.
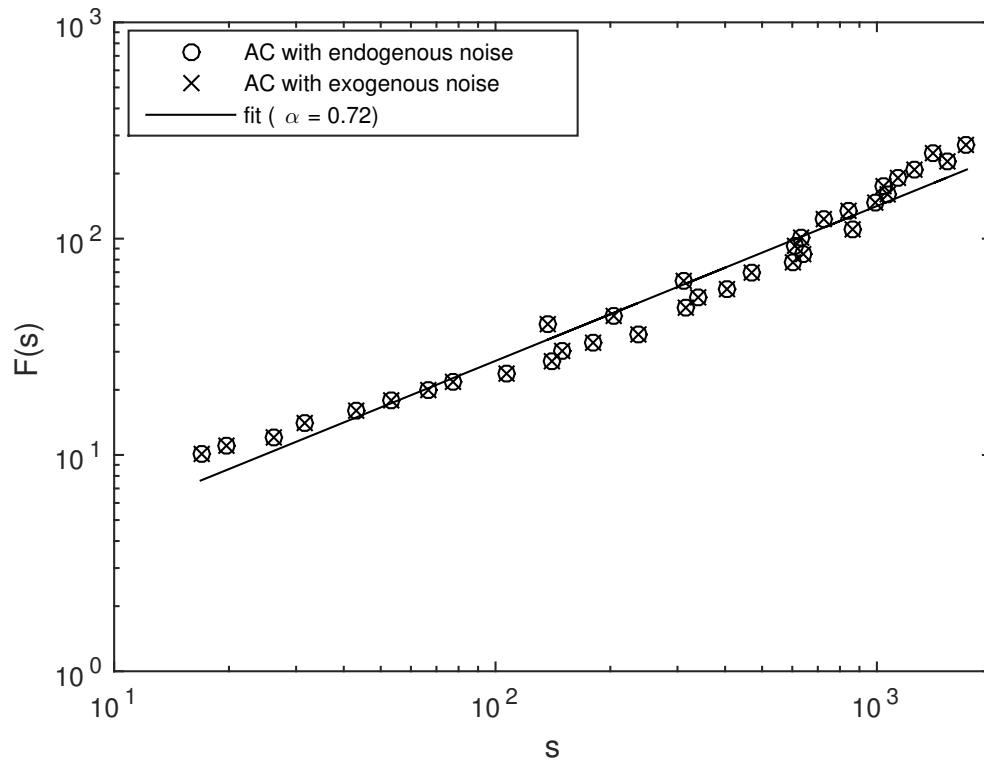
Source: produced by author.

6 CONCLUDING REMARKS

Detrended fluctuation analysis performed on the E-F valley irregularities have shown long–range correlation with a crossover which is an inherent property of the valley region irregularities. The presence of a crossover confirmed that the electron density fluctuation data changes its scaling exponent over different scales depending on the detrending order. Using equivalence relation between PSD and DFA, PSD exponent, β, has been calculated from the obtained DFA exponents, α and the variation found in scaling exponents are compared with the former equivalent sounding rocket experiment data analyzed using PSD method. Deviation in the β exponent is found to be $\sigma_m \gg 54\%$. These finding indicate that equatorial ionospheric plasma irregularities from the valley region are non–homogeneous.

The multifractal detrended fluctuation analysis provides various measures which need to be understood collectively to interpret the results. From this analysis, $h(q)$ infers long–range correlation with persistent temporal fluctuations in the time series, $\tau(q)$ infers the interaction between the scales to be nonlinear with non–homogeneous cascade, α tells how many fractal exponents or scales are required to reconstruct the time series and also high values of α_0 interpret underlying irregular process. Asymmetry (A) infers transition of fluctuations from small to large scales in the time series while moving to higher altitudes, probabilistic weights other than 0.5 confirms the multifractality in the series and quantifying them allows reconstructing the time series. The parameters $\Delta\alpha$ and dp, both do infer the intermittency in the series. All these collective information allow to conclude that the equatorial low latitude valley and F region plasma irregularities are nonlinear, intermittent, multifractal and exhibit non–homogeneous energy cascade. Therefore, this nature can be attributed to the wide variation observed in the spectral indices.

The potential of the MFDFA algorithm is tested in deciphering the morphology of the cascading phenomena by analyzing the F region irregularities where the rocket intercepted a plasma bubble. Muralikrishna et al. (2003) reported the presence of predominant sharp peaks in the power spectra over a wide range of heights, and they attribute these to a developing plasma bubble that subsequently dissipated energy, reaching an equilibrium which is evidenced by the absence of peaks. Multifractal analysis has captured this sequence of events. The presence of a plasma bubble characterized by large scale irregularities, which in turn is reflected in the low density, is observed around a mean height of 292.37 km. Contrarily, stronger multifractality is observed at this height. This inverse variation is in agreement with the turbulent–like

multiplicative cascade process. On the other hand, as the rocket traversed through higher altitudes, the mean density increased while the multifractality became weaker. This suggests that the cascading process resulted in smaller scale irregularities by dissipating energy.

The MFDFA algorithm quantifies the influence of larger fluctuations in the upper valley region time series. This characteristic is intriguing as valley region irregularities are found to be triggering the F region irregularities. The inverse variation between $\Delta\alpha$ and mean density is observed for the valley region irregularities also and evident that a more complex structure shows more richness of scaling.

Type I noise storm data are characterized as a nonlinear dynamical dissipative system. The intermittent multitude behavior of type I solar emission using multifractal analysis has been characterized. Two RNS events found to be nonlinear, multifractal, intermittent and exhibit non–homogeneous energy cascade. The pattern of asymmetry is intriguing. The first event recorded between 05:45 and 07:00 UT is characterized by larger fluctuations. For the second event transition of larger fluctuations (at 10:00 UT) to smaller fluctuations (at 11:00 and 11:45 UT) is evident.

An intriguing observation is noted regarding the valley region (Table 5.3) and type I solar noise burst (Table 5.5) multifractal analysis. A maximum $\Delta\alpha$ is observed for the most right–skewed spectrum which infers the dominance of smaller fluctuations. In the case of the valley region, $\Delta\alpha = 0.61$ and $A = 0.54$ and for type I noise storm, $\Delta\alpha = 0.53$ and $A = 0.41$. However, for the F region data, a maximum $\Delta\alpha = 0.93$ is observed for the most left–skewed spectrum with $A = 2.99$ (Table 5.4), where large scale irregularities (plasma bubble) were reported. A relation between maximum multifractal width, $\Delta\alpha$ and maximum left or right skewness, A requires to be investigated in detail.

A turbulent system evolves through nonlinear processes which are multiplicative in nature with nonlinear energy distribution among the scales, and is intermittent too (FRISCH, 1995; ABRAMENKO et al., 2002; ABRAMENKO; YURCHYSHYN, 2010). The energy dissipation can not be homogeneous in an intermittent system, in fact, it is intermittent (MONIN; YAGLOM, 1975; FRISCH, 1995). Hence, investigating intermittency in the space plasma fluctuations provide important information on the energy dissipation process. From these analyses, it is observed that ionospheric electron density fluctuations as well as type I solar emissions are intermittent, showing non–homogeneous energy cascade. To sum up, this work has provided sufficient analyses in favor of the third possibility for the wide variation reported in the spectral indices,

i.e., "The turbulent process does not follow a homogeneous cascade of the energy distribution between the scales involved in the dissipative process."

6.1 Future work

Multiplicative cascade process is a versatile tool to quantify scaling structures and to model different types of time series. The simple p model (MENEVEAU; SREENIVASAN, 1987) provide inputs for the underlying scaling structures (of plasma irregularities) but to characterize asymmetry in the multifractality, further advanced models can be used, where scale parameter is varied along with the probability parameter. Advanced fitting models and different methods have been suggested and implemented to analyze the asymmetric multifractal distribution (MACEK, 2007; SZCZEPANIAK; MACEK, 2008; CHENG, 2014). In future, this study will be extended to characterize and discuss the asymmetric multifractal nature of space plasma irregularities.

REFERENCES

ABRAMENKO, V.; YURCHYSHYN, V. Intermittency and multifractality spectra of the magnetic field in solar active regions. **The Astrophysical Journal**, v. 722, n. 1, p. 122–130, 2010. 8, 11, 68

ABRAMENKO, V. I. Multifractal analysis of solar magnetograms. **Solar Physics**, v. 228, p. 29–42, 2005. 22

ABRAMENKO, V. I.; YURCHYSHYN, V. B.; WANG, H.; SPIROCK, T. J.; GOODE, P. R. Scaling behavior of structure functions of the longitudinal magnetic field in active regions on the sun. **The Astrophysical Journal**, v. 577, p. 487–495, 2002. 11, 22, 68

ALIMOV, V. A.; VYBORNOV, F. I.; RAKHLIN, A. V. Multifractal structure of intermittency in a developed ionospheric turbulence. **Radiophys Quantum El**, v. 51, p. 438–445, 2008. 11

ALVAREZ-RAMIREZ, J.; IBARRA-VALDEZ, C.; RODRIGUEZ, E.; DAGDUG, L. 1/f-noise structures in Pollocks's drip paintings. **Physica A: Statistical Mechanics and its Applications**, v. 387, n. 1, p. 281–295, 2008. 16

BARABÁSI, A.-L.; VICSEK, T. Multifractality of self-affine fractals. **Physical Review A**, v. 44, p. 2730–2733, 1991. 32

BENTLEY, R. D.; KLEIN, K. L.; DRIEL-GESZTELYI, v. L.; DÉMOULIN, P.; TROTTET, G.; TASSETTO, P.; MARTY, G. Magnetic activity associated with radio noise storms. **Solar Physics**, v. 193, p. 227–245, 2000. 9

BENZ, A. O.; MONSTEIN, C.; MEYER, H. Callisto – a new concept for solar radio spectrometers. **Solar Physics**, v. 226, p. 143–151, 2005. 8

BENZ, A. O.; MONSTEIN, C. A.; MEYER, H.; MANOHARAN, P. K.; RAMESH, R.; ALTYNTSEV, A.; LARA, A.; PAEZ, J.; CHO, K. S. A world-wide net of solar radio spectrometers: e-callisto. **Earth, Moon, and Planets**, v. 104, p. 277–285, 2009. 8, 53

BERNERS-LEE, T.; KAGAL, L. The fractal nature of the semantic web. **AI Magzine**, v. 29, p. 29, 2008. 16

BISKAMP, D. **Nonlinear magnetohydrodynamics**. USA: Cambridge University Press, 1993. 42

BOLZAN, M.; ROSA, R. R.; SAHAI, Y. Multifractal analysis of low-latitude geomagnetic fluctuations. **Annales Geophysicae**, v. 27, p. 569–576, 2009. 32

BOLZAN, M. J. A.; TARDELLI, A.; PILLAT, V. G.; FAGUNDES, P. R.; ROSA, R. R. Multifractal analysis of vertical total electron content (VTEC) at equatorial region and low latitude, during low solar activity. **Annales Geophysicae**, v. 31, n. 1, p. 127–133, 2013. 11, 32

BOOKER, H. G.; WELLS, H. W. Scattering of radio waves by the F-region of the ionosphere. **Terrestrial Magnetism and Atmospheric Electricity**, v. 43, n. 3, p. 249–256, 1938. 5

BURLAGA, L.; WANG, C.; NESS, N. A model and observations of the multifractal spectrum of the heliospheric magnetic field strength fluctuations near 40 AU. **Geophysical Research Letters**, v. 30, n. 10, p. 1543, 2003. 11, 32

BURLAGA, L. F. Intermittent turbulence in the solar wind. **Journal of Geophysical Research: Space Physics**, v. 96, n. A4, p. 5847–5851, 1991. 10, 11

CARBONE, V. Cascade model for intermittency in fully developed magnetohydrodynamic turbulence. **Physical Review Letters**, v. 71, p. 1546–1548, 1993. 32

CARBONE, V.; BRUNO, R.; VELTRI, P. Scaling laws in the solar wind turbulence. In: _____. **Small-scale structures in three-dimensional hydrodynamic and magnetohydrodynamic turbulence, lecture notes in physics**. Heidelberg: Springer, 1995. v. 462, p. 153–158. 11

CHANDRASEKHAR, E.; PRABHUDESAI, S. S.; SEEMALA, G. K.; SHENVI, N. Multifractal detrended fluctuation analysis of ionospheric total electron content data during solar minimum and maximum. **Journal of Atmospheric and Solar-Terrestrial Physics**, v. 149, p. 31–39, 2016. 11, 18

CHAU, J. L.; HYSELL, D. L. High altitude large-scale plasma waves in the equatorial electrojet at twilight. **Annales Geophysicae**, v. 22, p. 4071–4076, 2004. 6

CHEN, Z.; IVANOV, P. C.; HU, K.; STANLEY, H. E. Effect of nonstationarities on detrended fluctuation analysis. **Physical Review E**, v. 65, p. 041107, 2002. 15

CHENG, Q. Generalized binomial multiplicative cascade processes and asymmetrical multifractal distributions. **Nonlinear Processes in Geophysics**, v. 21, n. 2, p. 477–487, 2014. 22, 69

CHHABRA, A.; JENSEN, R. V. Direct determination of the f(α) singularity spectrum. **Physical Review Letters**, v. 62, p. 1327–1330, 1989. 30

CHIAN, A. C. L.; ABALDE, J. R.; MIRANDA, R. A.; BOROTTO, F. A.; HYSELL, D. L.; REMPEL, E. L.; RUFFOLO, D. Multi-spectral optical imaging of the spatiotemporal dynamics of ionospheric intermittent turbulence. **Scientific Reports**, v. 8, n. 10568, 2018. 11

CHIAN, A. C. L.; MUÑOZ, P. R. Detection of current sheets and magnetic reconnections at the turbulent leading edge of an interplanetary coronal mass ejection. **The Astrophysical Journal Letters**, v. 733, n. L34, 2011. 11

CINTRA, M. A. U. **Comparação entre tempestades de ruídos solares tipo I e padrões de flutuações canônicas via análise de espectro gradiente**. 117 p. Dissertação (Mestrado em Física e Astronomia) — Universidade do Vale do Paraíba, São José dos Campos, 2018. Available from: <https://biblioteca.univap.br/dados/00003d/00003de4.pdf>. 8, 53, 58

CORONADO, A.; CARPENA, P. Size effects on correlation measures. **Journal of Biological Physics**, v. 31, p. 121–133, 2005. 15

COSTA, E.; KELLEY, M. C. On the role of steepened structures and drift waves in equatorial spread F. **Journal of Geophysical Research**, v. 83, n. A9, p. 4359–4364, 1978. 5

DAVIS, A.; A., M.; R., C.; WISCOMBE, W. The landsat scale break in stratocumulus as a three-dimensional radiative transfer effect: implications for cloud remote sensing. **Journal of the Atmospheric Sciences**, v. 54, n. 2, p. 241–260, 1997. 62

DELIGNIÉRES, D.; RAMDANI, S.; LEMOINE, L.; TORRE, K.; FORTES, M.; NINOT, G. Fractal analyses for 'short' time series: a re-assessment of classical methods. **Journal of Mathematical Psychology**, v. 50, n. 6, p. 525–544, 2006. 14

DELIGNIÉRES, D.; TORRE, K.; LEMOINE, L. Methodological issues in the application of monofractal analyses in psychological and behavioral research. **Nonlinear Dynamics, Psychology, and Life Sciences**, v. 9, n. 4, p. 435–461, 2005. 13, 14

DING, Z.; CLIVE, W. J. G.; ENGLE, R. F. J. A long memory property of stock market returns and a new model. **Journal of Empirical Finance**, v. 1, p. 83–106, 1993. 16

DUBRULLE, B. Beyond Kolmogorov cascades. **Journal of Fluid Mechanics**, v. 867, 2019. 32

DUTTA, S.; GHOSH, D.; CHATTERJEE, S. Multifractal detrended fluctuation analysis of human gait diseases. **Frontiers in Physiology**, v. 4, p. 274, 2013. 18

DYRUD, L.; KRANE, B.; OPPENHEIM, M.; PÉCSELI, H. L.; TRULSEN, J.; WERNIK, A. W. Structure functions and intermittency in ionospheric plasma turbulence. **Nonlinear Processes in Geophysics**, v. 15, p. 847–862, 2008. 11

DYSON, P. L.; MCCLURE, J. P.; HANSON, W. B. In situ measurements of the spectral characteristics of F region ionospheric irregularities. **Journal of Geophysical Research**, v. 79, n. 10, p. 1497–1502, 1974. 7

EKE, A.; HERMAN, P.; KOCSIS, L.; KOZAK, L. R. Fractal characterization of complexity in temporal physiological signals. **Physiological Measurement**, v. 23, n. 1, p. R1–R38, 2002. 13, 14, 15, 19

EKE, A.; HERMAN, P.; SANGANAHALLI, B.; HYDER, F.; MUKLI, P.; NAGY, Z. Pitfalls in fractal time series analysis: fMRI BOLD as an exemplary case. **Frontiers in Physiology**, v. 3, p. 417, 2012. 15

EKE, E.; HERMÁN, P.; BASSINGTHWAIGHTE, J. B.; RAYMOND, G. M.; PERCIVAL, D. B.; CANNON, M.; BALLA, I.; IKRÉNYI, C. Physiological time series: distinguishing fractal noises from motions. **European Journal of Physiology**, v. 439, p. 403–415, 2000. 15, 19

FEDER, J. **Fractals**. New York: Plenum, 1988. 25

FORNARI, G. **Estudo de técnicas fractal e multifractal para análise de irregularidades na ionosfera equatorial**. 157 p. Tese (Mestrado em Applied Computing) — Instituto Nacional de Pesquisas Espaciais (INPE), São José dos Campos, 2016. Available from: <http://urlib.net/rep/8JMKD3MGP3W34P/3LHFT8S>. 47

FORNARI, G.; ROSA, R.; MENESES, F. C. d.; MURALIKRISHNA, P. Spectral fluctuation analysis of ionospheric inhomogeneities over Brazilian territory. part I: equatorial F-region plasma bubbles. **Advances in Space Research**, v. 58, n. 10, p. 2037–2042, 2016. 7, 11, 37

FRANÇA, L. G. S.; MIRANDA, J. G. V.; LEITE, M.; SHARMA, N. K.; WALKER, M. C.; LEMIEUX, L.; WANG, Y. Fractal and multifractal properties of electrographic recordings of human brain activity: toward its use as a signal feature for machine learning in clinical applications. **Frontiers in Physiology**, v. 9, p. 1767, 2018. 18

FRISCH, U. **Turbulence**. USA: Cambridge University Press, 1995. 10, 22, 38, 42, 68

GHOSH, D.; DEB, A.; DUTTA, S.; SENGUPTA, P.; SAMANTA, S. Multifractality of radon concentration fluctuation in earthquake related signal. **Fractals**, v. 20, n. 01, p. 33–39, 2012. 42

GOLDBERGER, A. L.; AMARAL, L. A. N.; GLASS, L.; HAUSDORFF, J. M.; IVANOV, P. C.; MARK, R. G.; MIETUS, J. E.; MOODY, G. B.; PENG, C.-K.; STANLEY, H. E. Physiobank, physiotoolkit, and physionet: components of a new research resource for complex physiologic signals. 2000. Available from: <http://circ.ahajournals.org/cgi/content/full/101/23/e215]>. 35

GRAUER, R.; KRUG, J.; MARLIANI, C. Scaling of high-order structure functions in magnetohydrodynamic turbulence. **Physics Letters A**, v. 195, p. 335–338, 1994. 11

GRECH, D. Alternative measure of multifractal content and its application in finance. **Chaos, Solitons & Fractals**, v. 88, p. 183–195, 2016. 18

GRECH, D.; MAZUR, Z. Can one make any crash prediction in finance using the local Hurst exponent idea? **Physica A**, v. 336, p. 133–145, 2004. 16

GREINER, M.; EGGERS, H. C.; LIPA, P. Analytic multivariate generating function for random multiplicative cascade processes. **Physical Review Letters**, v. 80, p. 5333–5336, 1998. 32

HALSEY, T. C.; JENSEN, M. H.; KADANOFF, L. P.; PROCACCIA, I.; SHRAIMAN, B. I. Fractal measures and their singularities: the characterization of strange sets. **Physical Review A**, v. 33, n. 2, p. 1141–1151, 1986. 28, 29

HAMIDI, Z.; SHARIFF, N. **Investigation of characteristics of noise storm solar burst type I on 11th march 2013**. Singapore: Springer Nature Singapore Pte Ltd, 2018. 53

HARDSTONE, R.; POIL, S.-S.; SCHIAVONE, G.; JANSEN, R.; NIKULIN, V. V.; MANSVELDER, H. D.; LINKENKAER-HANSEN, K. Detrended fluctuation analysis: a scale-free view on neuronal oscillations. **Frontiers in Physiology**, v. 3, n. 450, 2012. 15

HARTMANN, A.; MUKLI, P.; NAGY, Z.; KOCSIS, L.; HERMÁN, P.; EKE, A. Real-time fractal signal processing in the time domain. **Physica A: Statistical Mechanics and its Applications**, v. 392, n. 1, p. 89–102, 2013. 13, 14

HENEGHAN, C.; MCDARBY, G. Establishing the relation between detrended fluctuation analysis and power spectral density analysis for stochastic processes. **Physical Review E**, v. 62, p. 6103–6110, 2000. 15

HILBORN, R. **Chaos and nonliner dynamics**. USA: Oxford university press, 2000. 29

HÖLL, M.; KIYONO, K.; KANTZ, H. Theoretical foundation of detrending methods for fluctuation analysis such as detrended fluctuation analysis and detrending moving average. **Physical Review E**, v. 99, n. 033305, 2019. 13, 14

HYSELL, D. An overview and synthesis of plasma irregularities in equatorial spread F. **Journal of Atmospheric and Solar-Terrestrial Physics**, v. 62, p. 1037–1056, 2002. Available from: <http://dx.doi.org/10.1016/S1364-6826(00)00095-X>. 5

HYSELL, D.; KELLEY, M. C.; SWARTZ, W. E.; WOODMAN, R. F. Seeding and layering of equatorial spread-F by gravity waves. **Journal of Geophysical Research**, v. 95, p. 17253–17260, 1999. 5

HYSELL, D. L.; KELLEY, M. C.; SWARTZ, W. E.; PFAFF, R. F.; M., S. C. Steepened structures in equatorial spread F: 1. new observations. **Journal of Geophysical Research**, v. 99, n. A5, p. 8827–8840, 1994. 5

HYSELL, D. L.; SEYLER, C. E.; KELLEY, M. C. Steepened structures in equatorial spread F: 2. theory. **Journal of Geophysical Research**, v. 99, n. A5, p. 8841–8850, 1994. 5

IHLEN, E. Introduction to multifractal detrended fluctuation analysis in matlab. **Frontiers in Physiology**, v. 3, p. 141, 2012. 18, 20

INSTITUTE FOR DATA SCIENCE FHNW BRUGG/WINDISCH, SWITZERLAND. **E-Callisto bleien solar radio data**. 2011. Available from:

<http://soleil.i4ds.ch/solarradio/data/2002-20yy_Callisto/2011/07/30/BLEN7M_20110730_064502_25.fit.gz>. 97

JACKSON, J. E. Measurements in the E-layer with the navy viking rocket. **Journal of Geophysical Research**, v. 59, n. 3, p. 377–390, 1954. 6

JACKSON, J. E.; SEDDON, J. C. Ionosphere electron-density measurements with the navy aerobee-hi rocket. **Journal of Geophysical Research**, v. 63, n. 1, p. 197–208, 1958. 6

JAHN, J. M.; LABELLE, J. Rocket measurements of high-altitude spread F irregularities at the magnetic dip equator. **Journal of Geophysical Research: Space Physics**, v. 103, n. A10, p. 23427–23441, 1998. 6, 11

JOSHI, N.; ROSA, R. R.; SAVIO, S.; KHERANI, E. A.; MENESES, F. C. de; STEPHANY, S.; MURALIKRISHNA, P. Structural characterization of the equatorial F region plasma irregularities in the multifractal context. **Annales Geophysicae**, v. 38, n. 2, p. 445–456, 2020. 18, 45

KAI, K.; MELROSE, D. B.; SUZUKI, S. **Storms**. USA: Cambridge University Press, 1985. 415-441 p. 8

KANTELHARDT, J. W. Fractal and multifractal time series. In: _____. **Encyclopedia of complexity and systems science**. New York: Springer New York, 2009. p. 3754–3779. 13, 15, 17, 18, 29, 32

KANTELHARDT, J. W.; KOSCIELNY-BUNDE, E.; REGO, H. H. A.; HAVLIN, S.; BUNDE, A. Detecting long-range correlations with detrended fluctuation analysis. **Physica A**, v. 295, p. 441–454, 2001. 17, 18

KANTELHARDT, J. W.; ZSCHIEGNER, S. A.; KOSCIELNY-BUNDE, E.; HAVLIN, S.; BUNDE, A.; STANLEY, H. E. Multifractal detrended fluctuation analysis of nonstationary time series. **Physica A: Statistical Mechanics and its Applications**, v. 316, n. 1, p. 87–114, 2002. Available from: <http://dx.doi.org/10.1016/S0378-4371(02)01383-3>. 18, 20, 23, 25, 32

KELLEY, M. **The Earth's ionosphere**. USA: Elsevier, 2009. 5

KELLEY, M. C.; HYSELL, D. L. Equatorial spread-F and neutral atmospheric turbulence: a review and a comparative anatomy. **Journal of Atmospheric and Terrestrial Physics**, v. 53, n. 8, p. 695–708, 1991. 7, 11

KELLEY, M. C.; ILMA, R. R.; CROWLEY, G. On the origin of pre-reversal enhancement of the zonal equatorial electric field. **Annales Geophysicae**, v. 27, 2009. 7

KELLEY, M. C.; PFAFF, R. F.; BAKER, K. D.; ULWICK, J. C.; LIVINGSTON, R.; RINO, C.; TSUNODA, R. Simultaneous rocket probe and radar measurements of equatorial spread-F-transitional and short wavelength results. **Journal of Geophysical Research**, v. 87, n. A3, p. 1575–1588, 1982. 7, 37, 38

KELLEY, M. C.; SEYLER, C. E.; ZARGHAM, S. Collisional interchange instability: 2. a comparison of the numerical simulations with the in situ experimental data. **Journal of Geophysical Research**, v. 92, p. 10089–10094, 1987. 5

KHERANI, E. A.; PAULA, E. R. D.; CUEVA, R. Y. C.; CAMARGO, L. A. P. Observations of nighttime equatorial-upper-E-valley region irregular structures from São Luís radar and their occurrence statistics: a manifestation of vertical coupling between E and F regions. **Journal of Atmospheric and Solar-Terrestrial Physics**, v. 75-76, p. 64–70, 2012. 7

KIMIAGAR, S.; MOVAHED, M. S.; KHORRAM, S.; SOBHANIAN, S.; TABAR, M. R. R. Fractal analysis of discharge current fluctuations. **Journal of Statistical Mechanics: Theory and Experiment**, v. 2009, n. 03, p. P03020, 2009. 18

KINTNER, P. M.; SEYLER, C. E. The status of observations and theory of high latitude ionospheric and magnetospheric plasma turbulence. **Space Science Review**, v. 41, p. 91–129, 1985. 7, 9

KIYONO, K. Establishing a direct connection between detrended fluctuation analysis and Fourier analysis. **Physical Review E**, v. 92, p. 042925, 2015. 15

KNOWLES, H.; HOSTETLER, M.; LIEBOVITCH, L. Describing the dynamics, distributions, and multiscale relationships in the time evolution of residential building energy consumption. **Energy and Buildings**, v. 158, p. 310–325, 2018. 18

KOSCIELNY-BUNDE, E.; KANTELHARDT, J. W.; BRAUN, P.; BUNDE, A.; HAVLIN, S. Long-term persistence and multifractality of river runoff records: detrended fluctuation studies. **Journal of Hydrology**, v. 322, p. 120–137, 2016. 32

KUDEKI, E.; FAWCETT, C. D. High resolution observations of 150 km echoes at Jicamarca. **Geophysical Research Letters**, v. 20, p. 1987–1990, 1993. 6

LEE, C.-K.; JUANG, L.-C.; WANG, C.-C.; LIAO, Y.-Y.; YU, C.-C.; LIU, Y.-C.; HO, D.-S. Scaling characteristics in ozone concentration time series (octs). **Chemosphere**, v. 62, p. 934–946, 2006. 32

LI, C.; CHEN, Y.; WANG, B.; RUAN, G. P.; FENG, S. W.; DU, G. H.; KONG, X. L. Euv and magnetic activities associated with type-I solar radio bursts. **Solar Physics**, v. 292, n. 82, 2017. 9, 53

LI, G.; NING, B.; PATRA, A. K.; WAN, W.; HU, L. Investigation of low-latitude E and valley region irregularities: their relationship to equatorial plasma bubble bifurcation. **Journal of Geophysical Research**, v. 116, p. A11319, 2011. 7

LIU, Y. H.; CIZEAU, P.; MEYER, M.; PENG, C. K.; STANLEY, H. E. Correlations in economic time series. **Physica A**, v. 245, p. 437–440, 1997. 16

LÓPEZ, J. L.; VELEVA, L.; LÓPEZ-SAURI, D. A. Multifractal detrended analysis of the corrosion potential fluctuations during copper patina formation on its first stages in sea water. **International Journal of Electrochemical Science**, v. 9, p. 1637–1649, 2014. 18

LU, X.; ZHAO, H.; LIN, H.; WU, Q. Multifractal analysis for soft fault feature extraction of nonlinear analog circuits. **Mathematical Problems in Engineering**, v. 2016, p. 7, 2016. 18

MACEK, W. M. Multifractality and intermittency in the solar wind. **Nonlinear Processes in Geophysics**, v. 14, n. 6, p. 695–700, 2007. 11, 22, 32, 69

MAEDA, K.-i. Mid-latitude electron density profile as revealed by rocket experiments. **Journal of Geomagnetism and Geoelectricity**, v. 21, n. 2, p. 557–567, 1969. 7

MALAMUD, B. D.; TURCOTTE, D. L. Self-affine time seriers: I. generation and analysis. **Advances in Geophysics**, v. 40, p. 1–90, 1999. 13

MANDAL, S.; ROYCHOWDHURY, T.; CHIROM, K.; BHATTACHARYA, A.; SINGH, R. K. B. Complex multifractal nature in mycobacterium tuberculosis genome. **Scientific Reports**, v. 7, n. 46395, 2017. 18, 42

MANDELBROT, B. Possible refinement of the lognormal hypothesis concerning the distribution of energy dissipation in intermittent turbulence. In: _____.

Statistical models and turbulence. lecture notes in physics. Heidelberg: Springer, 1972. v. 12. 25

_____. **Multifractals and 1/f Noise, wild self-affinity in physics (1963–1976)**. New York: Springer, 1998. 13

MCATEER, R. T. J.; GALLAGHER, P. T.; CONLON, P. A. Turbulence, complexity, and solar flares. **Advances in Space Research**, v. 45, p. 1067–1074, 2010. 11

MENEVEAU, C.; SREENIVASAN, K. R. Simple multifractal cascade model for fully developed turbulence. **Physical Review Letters**, v. 59, p. 1424–1427, Sep 1987. 25, 28, 29, 69

_____. The multifractal nature of turbulent energy dissipation. **Journal of Fluid Mechanics**, v. 224, p. 429–484, 1991. 10, 25

MIRANDA, R. A.; CHIAN, A. C.-L.; REMPEL, E. L. Universal scaling laws for fully-developed magnetic field turbulence near and far upstream of the Earth's bow shock. **Advances in Space Research**, v. 51, n. 1893, 2013. 11

MIRIYALA, S.; KOPPIREDDI, P. R.; CHANAMALLU, S. R. Robust detection of ionospheric scintillations using MF-DFA technique. **Earth, Planets and Space**, v. 67, n. 98, 2015. 11, 18

MONIN, A.; YAGLOM, A. **Statistical fluid mechanics**. USA: Cambridge:MIT Press,, 1975. 40, 42, 68

MUKLI, P.; NAGY, Z.; EKE, A. Multifractal formalism by enforcing the universal behavior of scaling functions. **Physica A**, v. 417, p. 150–167, 2015. 18

MURALIKRISHNA, P.; ABDU, M. A. Rocket measurements of ionospheric electron density from Brazil in the last two decades. **Advances in Space Research**, v. 37, p. 1091–1096, 2006. 47

MURALIKRISHNA, P.; VIEIRA, L. Equatorial F-region irregularities generated by the Rayleigh-Taylor instability mechanism - rocket obervations from Brazil. **Revista Brasileira de Geofísica**, v. 25, p. 135–149, 2007. 37, 38, 47

MURALIKRISHNA, P.; VIEIRA, L. P.; ABDU, M. A. Electron density and electric field fluctuations associated with developing plasma bubbles. **Journal of Atmospheric and Solar-Terrestrial Physics**, v. 65, n. 14, p. 1315–1327, 2003. 7, 47, 67

NEELAKSHI, J.; ROSA, R. R.; SAVIO, S.; MENESES, F. C. D.; STEPHANY, S.; FORNARI, G.; MURALIKRISHNA, P. Spectral fluctuation analysis of ionospheric inhomogeneities over Brazilian territory. part II: E-F valley region plasma instabilities. **Advances in Space Research**, v. 64, p. 1592–1599, 2019. 7, 11, 35

ODRIOZOLA, S. S. **Estudo de irregularidades do plasma ionosférico na região entre as camadas E e F no setor brasileiro a partir de medidas de foguete**. 250 p. Tese (Doutorado em Aeronomia) — Instituto Nacional de Pesquisas Espaciais (INPE), São José dos Campos, 2017. Available from: <http://urlib.net/rep/8JMKD3MGP3W34P/3MHF9DS>. 33, 35

ODRIOZOLA, S. S.; MENESES, F. C. de; MURALIKRISHNA, P.; PIMENTA, A.; KHERANI, E. A. Rocket in situ observation of equatorial plasma irregularities in the region between E and F layers over Brazil. **Annales Geophysicae**, v. 35, p. 413–422, 2017. 7, 33, 34

ORAL, E.; UNAL, G. Modeling and forecasting time series of precious metals: a new approach to multifractal data. **Financial Innovation**, v. 5, p. 22, 2019. 18

PARGA, M. Vázquez de; GARCÌA, P.; LÓPEZ, D. A sufficient condition to polynomially compute a minimum separating DFA. **Information Sciences**, v. 370-371, p. 204–220, 2016. 15

PASCHALIS, A.; MOLNAR, P.; BURLANDO, P. Temporal dependence structure in weights in a multiplicative cascade model for precipitation. **Water Resources Research**, v. 48, p. W01501, 2012. 32

PATRA, A. K. Some aspects of electrostatic coupling between E and F regions relevant to plasma irregularities: a review based on recent observations. **Journal of Atmospheric and Solar-Terrestrial Physics**, v. 70, n. 17, p. 2159–2171, 2008. 7

PÉCSELI, H. L. Spectral properties of electrostatic drift wave turbulence in the laboratory and the ionosphere. **Annales Geophysicae**, v. 33, n. 7, p. 875–900, 2015. 7

PEITGEN, H.-O.; JÜRGENS, H.; SAUPE, D. **Chaos and Fradals**. New York: Springer-Verlag, 1992. 25

PENG, C. K.; BULDYREV, S. V.; HAVLIN, S.; SIMONS, M.; STANLEY, H. E.; GOLDBERGER, A. L. Mosaic organization of DNA nucleotides. **Physical Review E**, v. 49, n. 2, p. 1685–1689, 1994. 13, 14

PILGRIM, I.; TAYLOR, R. P. Fractal analysis of time-series data sets: methods and challenges. **Fractal Analysis**, 2018. 13, 14

POPE, S. **Turbulent flows**. USA: Cambridge University Press, 2000. 10

PRAKASH, S. Production of electric field perturbations by gravity wave winds in the E region suitable for initiating equatorial spread F. **Journal of Geophysical Research**, v. 104, n. A5, p. 10051–10069, 1999. 7

REDNER, S. Random multiplicative processes: an elementary tutorial. **American Journal of Physics**, v. 58, p. 267–273, 1989. 32

RINO, C. L.; TSUNODA, R. T.; PETRICEKS, J.; LIVINGTON, R. C.; KELLEY, M. C.; BAKER, K. D. Simultaneous rocket-borne beacon and in situ measurements of equatorial spread F-intermediate wavelength results. **Journal of Geophysical Research**, v. 86, n. A4, p. 2411–2420, 1981. 37, 38

ROBERTS, D. C.; TURCOTTE, D. L. Fractality and self-organized criticality of wars. **Fractals**, v. 06, n. 04, p. 351–357, 1998. 65

RODRIGUES, F. S.; PAULA, E. R. D.; CHAU, J. L. On the characteristics of 150-km echoes observed in the Brazilian longitude sector by the 30 MHz São Luís radar. **Annales Geophysicae**, v. 29, p. 1905–1916, 2011. 6

ROSA, R. R.; BOLZAN, M. J. A.; FERNANDES, F.; VERONESE, T.; SAWANT, H. S. Multifractal analysis of an intermittent solar burst observed by the Brazilian solar spectroscope. **Proceedings of the Brazilian Decimetric Array Workshop**, 2008. 8, 32

ROSA, R. R.; BOLZAN, M. J. A.; FERNANDES, F. C. R.; SAWANT, H. S.; KARLICKÝ, M. Nonlinear analysis of decimetric solar bursts. **Solar and Stellar Variability: Impact on Earth and Planets, Proceedings of the International Astronomical Union**, v. 264, p. 279–281, 2010. 32

ROSA, R. R.; NEELAKSHI, J.; PINHEIRO, G. A. L. L.; BARCHI, P. H.; SHIGUEMORI, E. H. **Modeling social and geopolitical disasters as extreme events: a case study considering the complex dynamics of international armed conflicts**. Cham: Springer International Publishing, 2019. 233-254 p. 32

SALAT, H.; MURCIO, R.; ARCAUTE, E. Multifractal methodology. **Physica A: Statistical Mechanics and its Applications**, v. 473, p. 467–487, 2017. 18

SALAT, H.; MURCIO, R.; YANO, K.; ARCAUTE, E. Uncovering inequality through multifractality of land prices: 1912 and contemporary Kyoto. **PLOS ONE**, v. 13, n. 4, p. 1–19, 2018. 18

SANTHANAM, M. S.; BANDYOPADHYAY, J. N.; ANGOM, D. Quantum spectrum as a time series: fluctuation measures. **Physical Review E**, v. 73, p. 015201, 2006. 15

SAOUMA, V. E.; BARTON, C. C.; GAMALELDIN, N. A. Fractal characterization of fracture surfaces in concrete. **Engineering Fracture Mechanics**, v. 35, n. 1, p. 47–53, 1990. 15

SAVIO, S.; MURALIKRISHNA, P.; BATISTA, I. S.; MENESES, F. C. de. Wave structures observed in the equatorial F-region plasma density and temperature during the sunset period. **Advances in Space Research**, v. 58, p. 2043–2051, 2016. 33

SEN, A. K. Multifractality as a measure of complexity in solar flare activity. **Solar Physics**, v. 241, 2007. 11

SHAO, Y.-H.; GU, G.-F.; JIANG, Z.-Q.; ZHOU, W.-X.; SORNETTE, D. Comparing the performance of FA, DFA and DMA using different synthetic long-range correlated time series. **Scientific Reports**, v. 2, n. 835, 2012. 13, 14

SIKORA, G.; HÖLL, M.; GAJDA, J.; KANTZ, H.; CHECHKIN, A. V.; WYLOMAǸSKA, A. Probabilistic properties of detrended fluctuation analysis for Gaussian processes. **Physical Review E**, v. 101, n. 032114, 2020. 13, 14

SINHA, H.; PANDEY, R.; SHARMA, S.; MISRA, R. N. Nighttime E region plasma irregularities over an equatorial station Trivandrum. **Journal of Atmospheric and Solar-Terrestrial Physics**, v. 73, n. 17-18, p. 2444–2452, 2011. 37, 38

SINHA, H. S. S.; PANDEY, R.; MISRA, R. N. In situ measurement of nighttime plasma density irregularities over an equatorial station Trivandrum. **Journal of Geophysical Research**, v. 115, p. A11308, 2010. 37, 38

SINHA, H. S. S.; RAIZADA, S.; MISRA, R. N. First simultaneous in situ measurement of electron density and electric field fluctuations during spread F in the Indian zone. **Geophysical Research Letters**, v. 26, n. 12, p. 1669–1672, 1999. 7

SIVAVARAPRASAD, G.; OTSUKA, Y.; TRIPATHI, N. K.; CHOWDHARY, V. R.; RATNAM, D. V.; KHAN, M. A. Spatial and temporal characteristics of ionospheric total electron content over indian equatorial and low-latitude GNSS stations. **Conference on Signal Processing And Communication Engineering Systems**, p. 105–108, 2018. 11

SODRÉ, Z. A. L.; CUNHA-SILVA, R. D.; FERNANDES, F. C. R. Analysis of chains of metric solar type I bursts. **Solar Physics**, v. 209, p. 159–168, 2015. 8, 9, 11, 53

SODRÉ, Z. A. L.; FERNANDES, F. C. R.; SANTOS, J. C.; WRASSE, C. M. Radio noise storms and the connection with the reorganization of photospheric magnetic fields. **Solar Physics**, v. 294, n. 140, 2019. 9, 53, 58

SORNETTE, D.; DESCHÂTRES, F.; GILBERT, T.; AGEON, Y. Endogenous versus exogenous shocks in complex networks: an empirical test using book sale rankings. **Physical Review Letters**, v. 93, p. 228701, 2004. 59

SOUZA, V. C. O.; ASSIREU, A. T. Detrended fluctuation analysis of spatially extended digital surfaces: the classification process of 1/f noise and computacional performance. **Journal of Computational Interdisciplinary Sciences**, 2016. Available from: <http://www.epacis.net/jcis/PDF_JCIS/JCIS11-art.0115.pdf>. 14

SPICER, D. S.; BENZ, A. O.; HUBA, J. D. Solar type I noise storms and newly emerging magnetic flux. **Astronomy and Astrophysics**, v. 105, p. 221–228, 1982. 8

SPICHER, A.; MILOCH, W. J.; CLAUSEN, L. B. N.; MOEN, J. I. Plasma turbulence and coherent structures in the polar cap observed by the ICI-2 sounding rocket. **Journal of Geophysical Research Space Physics**, v. 120, p. 10959–10978, 2015. 11

SZCZEPANIAK, A.; MACEK, W. M. Asymmetric multifractal model for solar wind intermittent turbulence. **Nonlinear Processes in Geophysics**, v. 15, n. 4, p. 615–620, 2008. 69

TANNA, H. J.; PATHAK, K. N. Multifractal behaviour of the ionospheric scintillation index time series over an Indian low latitude station Surat. **Journal of Atmospheric and Solar-Terrestrial Physics**, v. 109, p. 66–74, 2014. 11, 18, 42

TELESCA, L.; LOVALLO, M. Revealing competitive behaviours in music by means of the multifractal detrended fluctuation analysis: application to Bach's sinfonias. **Proceedings of the Royal Society A**, v. 467, p. 3022–3032, 2011. 18

UNIVERSITY OF BONN. p **model time series by Victor Venema**. Available from: <http://www2.meteo.uni-bonn.de/staff/venema/themes/surrogates/pmodel/pmodel.m>. 62

VERONESE, T. B.; ; ROSA, R. R.; BOLZAN, M. J. A.; FERNANDES, F. C. R.; SAWANT, H. S.; KARLICKỲ, M. Fluctuation analysis of solar radio bursts associated with geoeffective X-class flares. **Journal of Atmospheric and Solar-Terrestrial Physics**, v. 73, p. 1311–1316, 2011. 8, 11, 15

VERONIG, A.; MESSEROTTI, M.; A., H. Determination of fractal dimensions of solar radio bursts. **Astronomy and Astrophysics**, v. 357, p. 337–350, 2000. 58

VICKREY, J. F.; KELLEY, M. C. The effects of a conducting E layer on classical F region cross-field plasma diffusion. **Journal of Geophysical Research**, v. 87, n. A6, p. 4461–4468, 1982. 7

VICKREY, J. F.; KELLEY, M. C.; PFAFF, R.; GOLDMAN, S. R. Low-altitude image striations associated with bottomside equatorial spread F: observations and theory. **Journal of Geophysical Research**, v. 89, n. A5, p. 2955–2961, 1984. 7

WAKAI, N. Quiet and disturbed structure and variations of the nighttime E region. **Journal of Geophysical Research**, v. 72, n. 17, p. 4507–4517, 1967. 7

WAKAI, N.; SAWADA, K. Nocturnal variation of the ionospheric E region in a temperate latitude associated with geomagnetic disturbances. **Journal of Radio Research Laboratory**, v. 11, p. 1–17, 1964. 7

WAWRZASZEK, A.; ECHIM, M.; BRUNO, R. Multifractal analysis of heliospheric magnetic field fluctuations observed by Ulysses. **The Astrophysical Journal**, v. 876, n. 2, p. 1538–4357, 2019. 11

WAWRZASZEK, A.; MACEK, W. M. Observation of the multifractal spectrum in solar wind turbulence by Ulysses at high latitudes. **Journal of Geophysical Research**, v. 115, p. A7, 2010. 11

WERNIK, A. W.; SECAN, J. A.; FREMOUW, E. J. Ionospheric irregularities and scintillation. **Advances in Space Research**, v. 31, n. 4, p. 971–981, 2003. 11

WILD, J. P.; MCCREADY, L. L. Observations of the spectrum of high-intensity solar radiation at metre wavelengths. I. the apparatus and spectral types of solar burst observed. **Australian Journal of Chemistry**, v. 3, p. 387–398, 1950. 8

XIE, H.; LI, G.; ZHAO, X.; HU, L.; WU, B.; NING, B. Statistical study on the occurrences of postsunset ionospheric E, valley, and F region irregularities and their correlations over low-latitude Sanya. **Journal of Geophysical Research: Space Physics**, v. 123, n. 11, p. 9873–9880, 2018. 7

XIONG, G.; YU, W.; XIA, W.; ZHANG, S. Multifractal signal reconstruction based on singularity power spectrum. **Chaos, Solitons and Fractals**, v. 91, p. 25–32, 2016. 32

XIONG, G.; ZHANG, S.; ZHAO, H. Multifractal spectrum distribution based on detrending moving average. **Chaos, Solitons & Fractals**, v. 65, p. 97–110, 2014. 32

YAMAMOTO, N.; KUBO, Y.; ISHIZAWA, K.; KIM, G.; MORIYA, T.; YAMANOUCHI, T.; OTSUKA, K. Detrended fluctuation analysis is considered to be useful as a new indicator for short-term glucose complexity. **Diabetes Technology and Therapeutics**, v. 12, n. 10, 2010. 15

YOKOYAMA, T.; PATRA, A. K.; FUKAO, S.; YAMAMOTO, M. Ionospheric irregularities in the low-latitude valley region observed with the equatorial atmosphere radar. **Journal of Geophysical Research**, v. 110, p. A10304, 2005. 7

ZARGHAM, S.; SEYLER, C. E. Collisional interchange instability: 1. numerical simulations of intermediate-scale irregularities. **Journal of Geophysical Research**, v. 92, n. A9, p. 10073–10088, 1987. 5

ZAVVARI, A.; ISLAM, M. T.; ANWAR, R.; ABIDIN, Z. Z.; ASILLAM, M. F.; MONSTEIN, C. Analysis of radio astronomy bands using CALLISTO spectrometer at Malaysia-UKM station. **Experimental Astronomy**, v. 41, p. 185–195, 2016. 53

APPENDIX A: TIME COMPLEXITY AND FLOWCHARTS

A.1 Error calculation

Absolute errors shown in the MFDFA plots (Figures 5.4, 5.5, 5.8, 5.9, 5.11, 5.12, & 5.13) are calculated as following:

While computing $h(q)$, obtaining linear fit to the fluctuation function for each q introduces error. Error in $h(q)$ ($E[h(q)]$) is calculated by subtracting detrended fit points from the corresponding $F_q(s)$ profile. Knowing the error in $h(q)$ and using the equations for computing $\tau(q)$ (equation 3.10), α (equation 3.11), and $f(\alpha)$ (equation 3.12) from $h(q)$, errors are calculated as

$$E[\tau(q)] = qE[h(q)] \tag{A.1}$$

$$E[\alpha] = E[h(q)] + qE\Big[\frac{dh(q)}{dq}\Big] \tag{A.2}$$

$$E[f(\alpha)] = q^2 E\Big[\frac{dh(q)}{dq}\Big] \tag{A.3}$$

A.2 Computational time complexity

Computational time complexity infers the abstract execution time of an algorithm. It is denoted in an asymptotic notation, as big O, which represents upper bound on the algorithm's run time. It is independent of the hardware.

a) DFA:
First *for* loop run on the scales. Scales are increased with a base two (2^n). Here, the complexity is $\mathcal{O}(\log n)$. Within the scales' loop, another *for* loop runs on segments and each segment is detrended with a linear fit. Here, the complexity is $\mathcal{O}(n)$. Other computational steps follow linear complexity. Hence, total run time complexity for DFA is $\mathcal{O}(n \log n)$.

b) MFDFA:
Since MFDFA is the generalized version of the DFA, its complexity should minimal be that of DFA. Additional computational step is to compute q^{th} order fluctuation function. It can be done in two ways.
(i) After computing the fluctuation function as described in the DFA, run a *for* loop on values of q. A *for* loop will increase the complexity by $\mathcal{O}(n)$, giving total complexity for the MFDFA as $\mathcal{O}(n + n \log n)$, retaining the

complexity equivalent to the DFA.

(ii) Embed the DFA *for* loops within the q *for* loop. However, this increases the complexity by $O(n * n \log n)$ which is $\mathcal{O}(n^2 \log n)$.

c) p model singularity spectrum:

Among the computational steps, complexity is solely determined by a *for* loop. Here, the complexity is given by $\mathcal{O}(n)$.

d) p model time series:

This algorithm involves first *for* loop where an array gets divided into two equal parts in each run giving the complexity $\mathcal{O}(n)$. Inside this *for* loop, value is assign to each segment, giving the complexity as $\mathcal{O}(n)$. Total complexity of this algorithm is $\mathcal{O}(n^2)$.

A.3 Flowcharts

This section presents flowcharts for the DFA and MFDFA, the p model for fitting the multifractal spectrum and for generating time series. The codes are written in Octave and in Python, and are available in the following repository: `https://github.com/neelakshij/codes`

Figure A.1 - Flowchart: DFA

Description
Inputs: time series x_k; k=1,2,...,1024 scales, s(i) = [8,32,..,256]
for s(i) = 256 nseg(j) = 1024/256 = 4
for each of 4 segments find trend segment – trend compute variance end
for all scales compute F(s) end
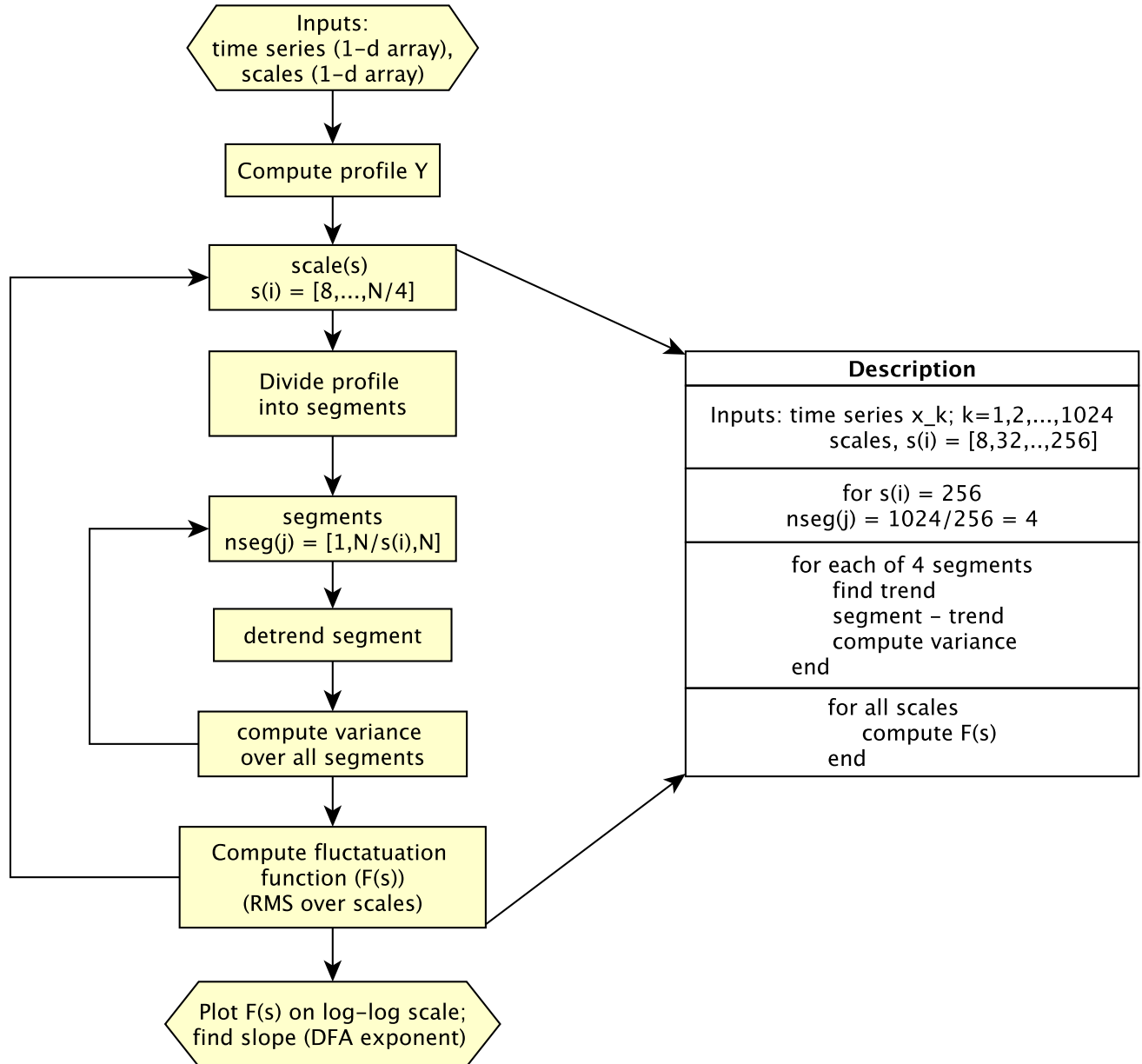
Source: produced by author.

Figure A.2 - Flowchart: MFDFA

Inputs:
time series (1–d array),
moments q (1–d array),
scales (1–d array)

Yes — DFA alpha = [1.2,1.8] ? — No

Compute profile
Y(i) = x(i+1) – x(i)

Compute profile Y

scale(s)
s(i) = [8,...,N/4]

Divide profile
into segments

segments
nseg(j) = [1,N/s(i),N]

detrend segment

compute variance
over all segments

Compute fluctatuation
function (F(s))
(RMS over scales)

Compute qth–order
fluctatuation (Fq(s))

Plot Fq(s) on log–log scale;
find slope (hq exponents)
compute tau(q) and
multifractal spectrum

Description
Inputs: time series x_k; k=1,2,...,1024 scales, s(i) = [8,32,..,256]
for s(i) = 256 nseg(j) = 1024/256 = 4
for each of 4 segments find trend segment – trend compute variance end
for all scales compute F(s) end
for all moments compute Fq(s) end

Source: produced by author.

Figure A.3 - Flowchart: p model singularity spectra
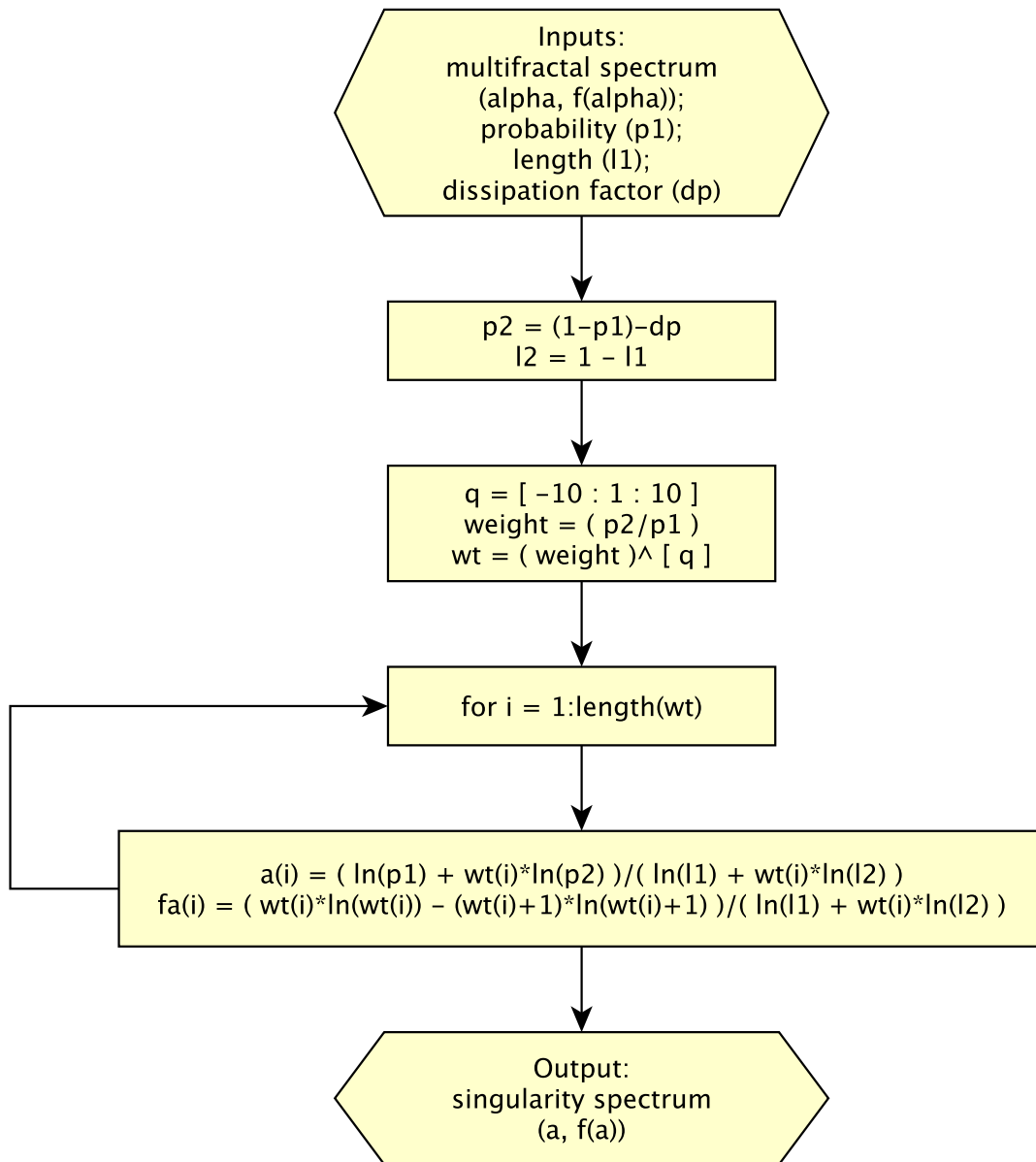
Figure A.4 - Flowchart: p model time series
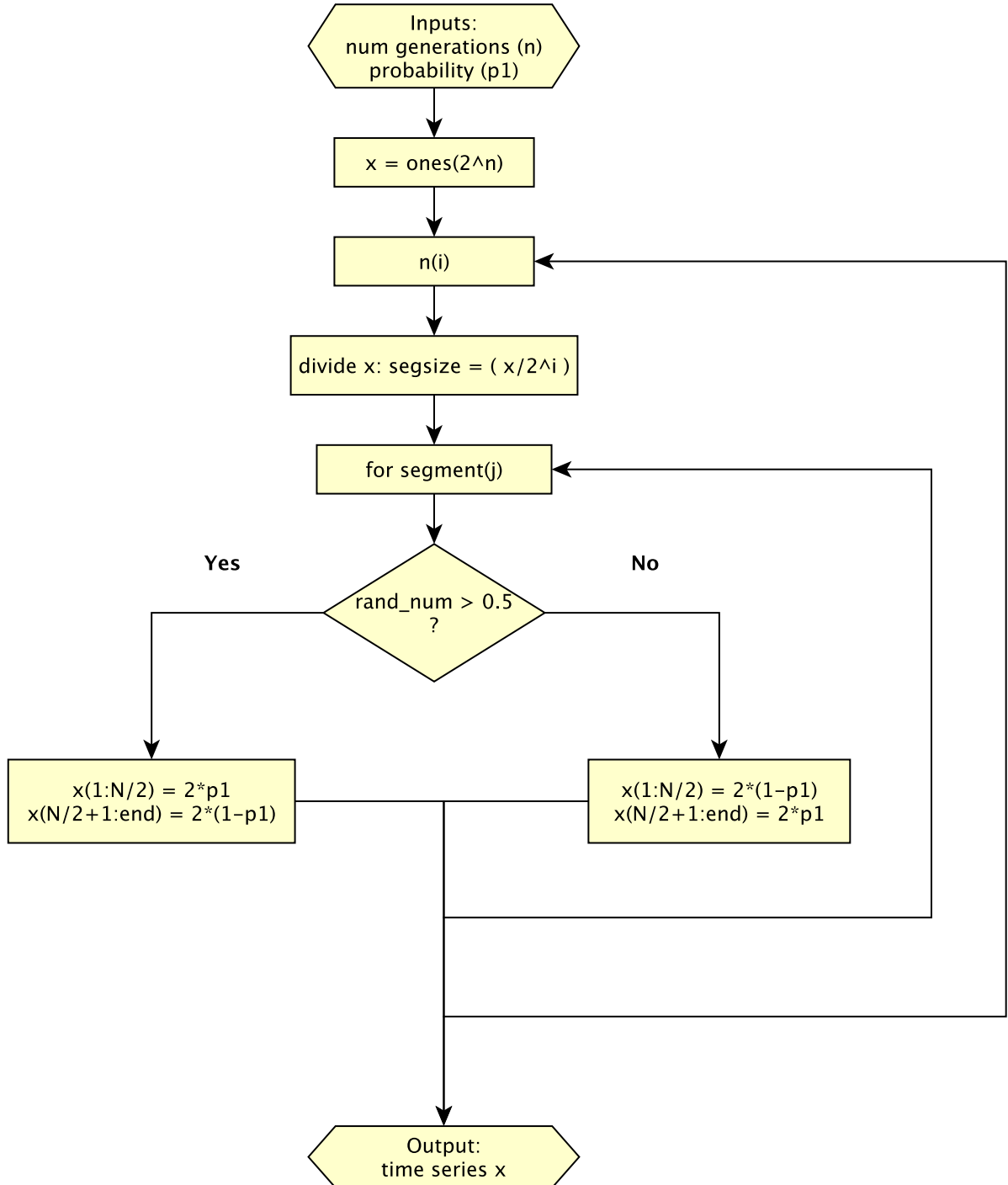
Source: produced by author.

APPENDIX B: ANALYSIS

B.1   DFA of time series from the upleg profile

Figure B.1 - Left column shows electron density fluctuations time series for mean heights of 152.56, 169.13, 263.69 and 316.9 km from the upleg profile. Right column shows corresponding fluctuation function profile.

Source: produced by author.

93
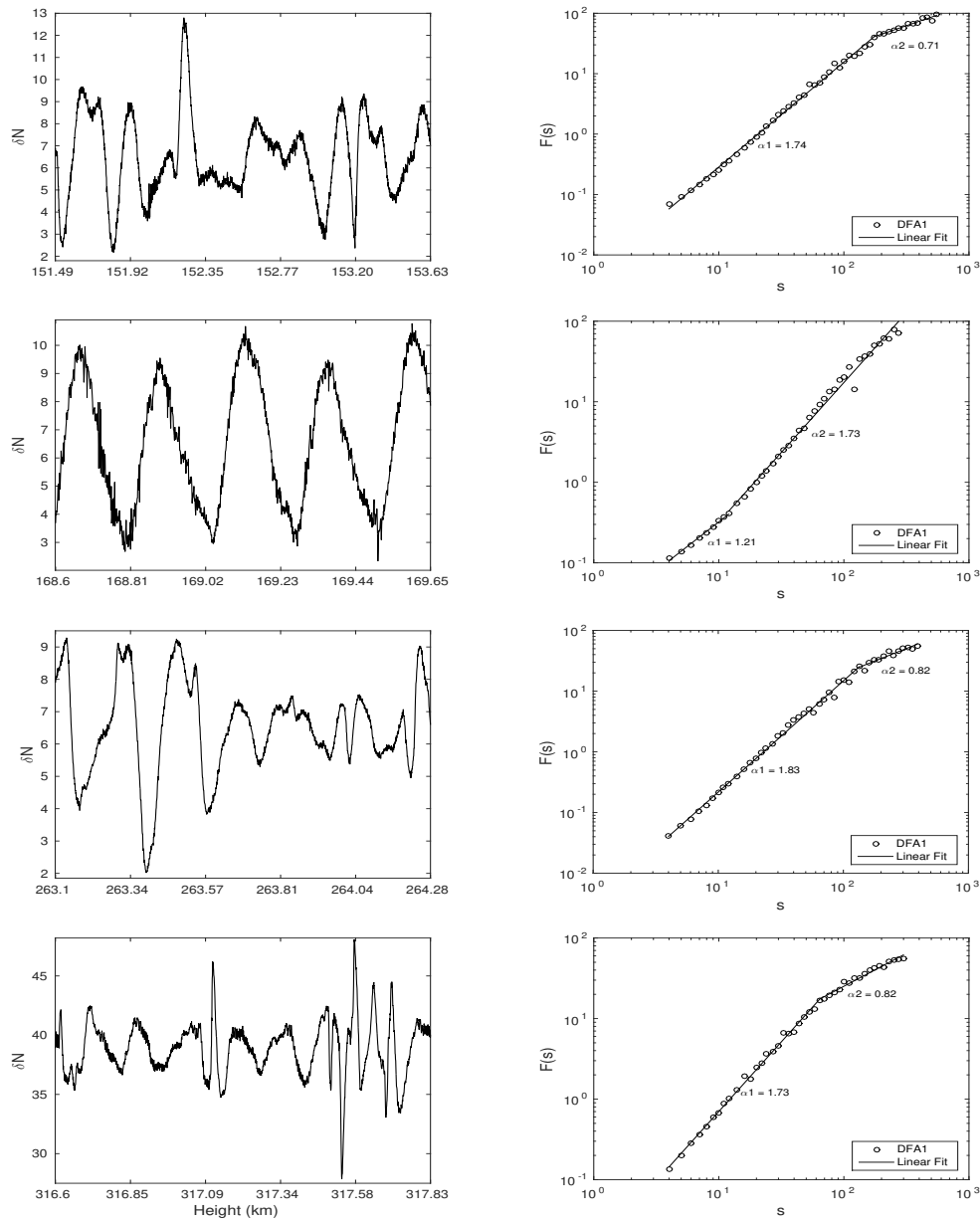
B.2 Source of the multifractality

B.2.1 Source of multifractality in the valley region time series

Figure B.2 shows the original and shuffled time series and their respective multifractal spectra for the mean height 259.34 km from the downleg profile. Shuffled series shows weaker multifractality compared to the original series, hence multifractality is attributed to the long–range correlations as well as to the broad probability density function.

Figure B.2 - Left panel shows original (below) and randomly shuffled (top) downleg time series for the mean height 259.34 km from the valley region. Right panel shows corresponding multifractal spectra.
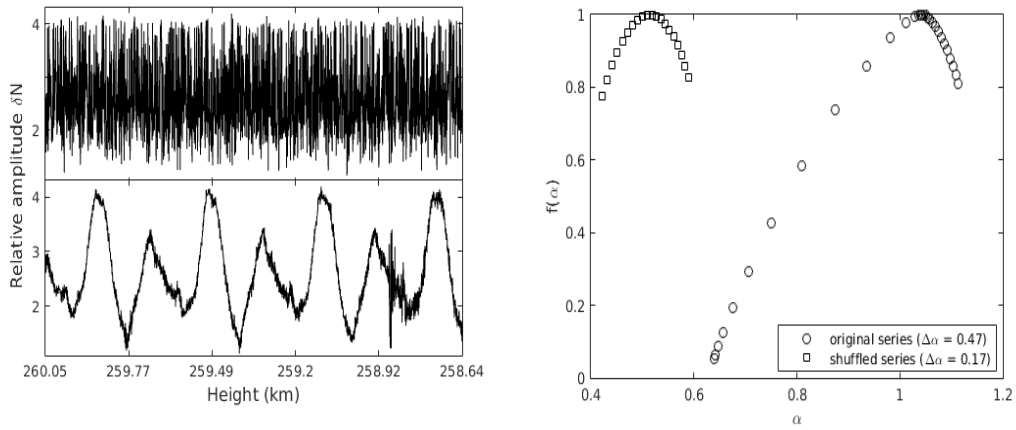
Source: produced by author.

B.2.2   Source of multifractality in the F region time series

Figure B.3 shows the original and shuffled time series and their respective multifractal spectra for the mean height 292.37 km from the downleg profile. Shuffled series shows weaker multifractality compared to the original series, hence multifractality is attributed to the long–range correlations as well as to the broad probability density function.

Figure B.3 - Left panel shows original (below) and randomly shuffled (top) downleg time series for the mean height 292.37 km from the F region. Right panel shows corresponding multifractal spectra.
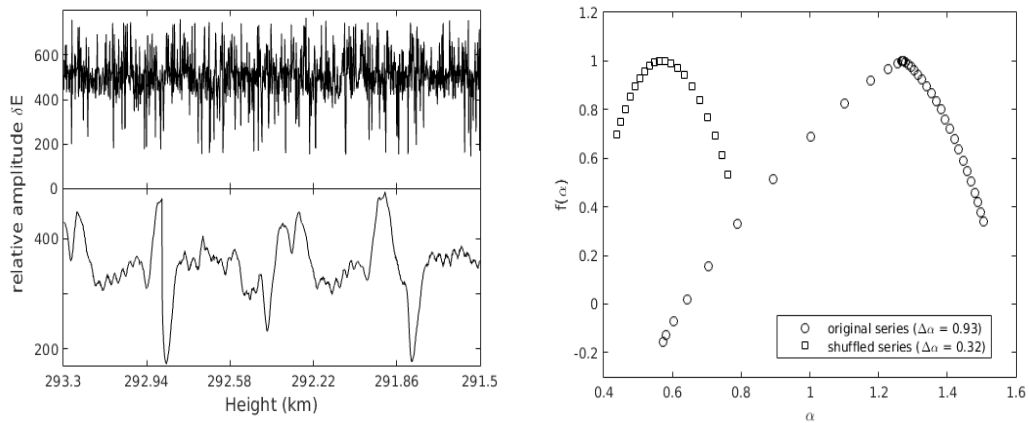
Source: produced by author.

B.2.3 Source of multifractality in type I noise storm series

Figure B.4 shows the original and shuffled time series and their respective multifractal spectra for type I noise storm recorded between 06:45 and 07:00 UT. Shuffled series retained its multifractality, hence multifractality is attributed to the broad probability density function.

Figure B.4 - Left panel shows original (below) and randomly shuffled (top) type I noise storm series recorded between 06:45 and 07:00 UT. Right panel shows corresponding multifractal spectra.
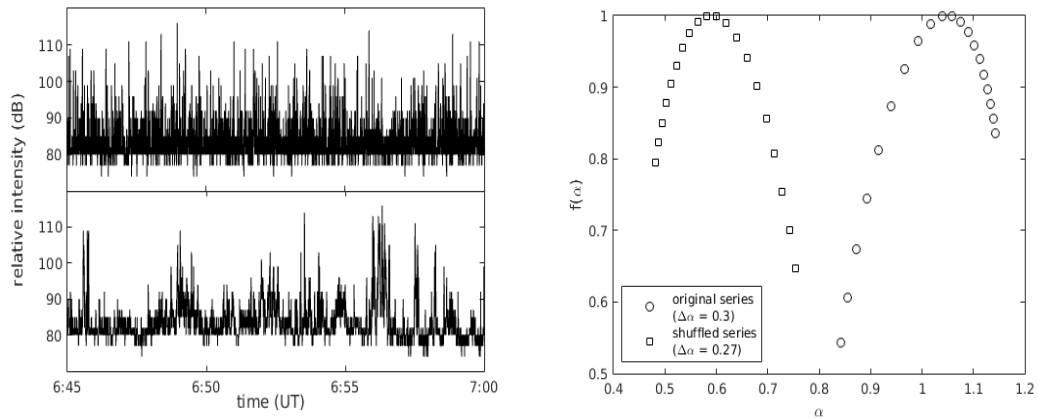
Source: produced by author.

Spectrogram of type I noise storm series obtained from e-Callisto, recorded between 06:45 and 07:00 UT is shown in the Figure B.5.

Figure B.5 - Spectrogram of type I noise storm series recorded between 06:45 and 07:00 UT.
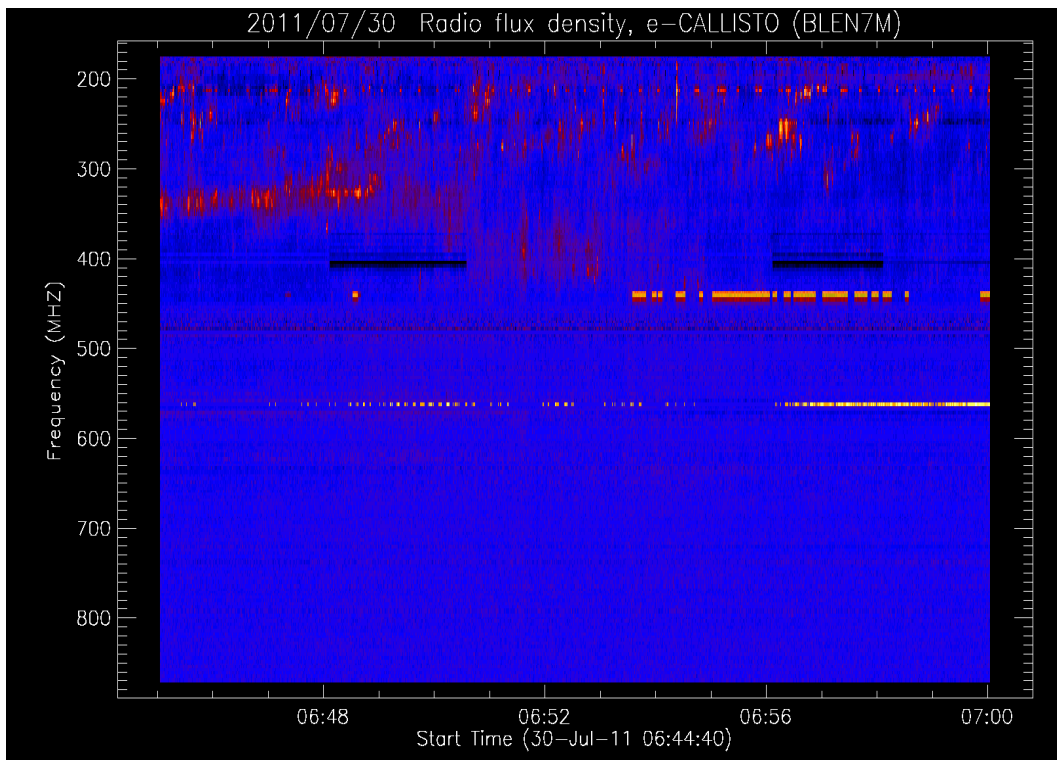
ANNEX - ARTICLE 1

This annex presents a paper published in the journal Advances in Space Research.

Spectral fluctuation analysis of ionospheric inhomogeneities over Brazilian territory Part II: E-F valley region plasma instabilities

Neelakshi Joshi, Reinaldo R. Rosa, Siomel Savio Odriozola, Francisco Carlos de Meneses, Stephan Stephany, Gabriel Fornari and Polinaya Muralikrishna

National Institute for Space Research

Abstract

This article presents the DFA of the E-F valley region electron density fluctuations for the first time. Analysis shows that these irregularities exhibit long–range correlation with crossovers that are intrinsic to the data for all the chosen altitudes. The PSD exponent β is computed for the analyzed data and compared with earlier similar experiments. The results show $\sigma_m >> 50\%$. These observations along with the profile of α with respect to the height indicate that scaling exponents show wide variation from the $K41$ theory, for both the E-F valley and F regions. This implies that the turbulent like ionospheric fluctuations as a whole cannot be described by the $K41$ homogeneous energy cascade theory.

Spectral fluctuation analysis of ionospheric inhomogeneities over Brazilian territory Part II: E-F valley region plasma instabilities

Neelakshi J. [a,*], Reinaldo R. Rosa [a], Siomel Savio [b,c,d],
Francisco C. de Meneses [c,e], Stephan Stephany [a], Gabriel Fornari [a], Muralikrishna P. [b]

[a] *Computational Space Physics Group, Lab for Computing and Applied Math (LABAC), National Institute for Space Research (INPE), Av. dos Astronautas, 1758, São José dos Campos, São Paulo 12227-690, Brazil*
[b] *Aeronomy Division, National Institute for Space Research (INPE), Av. dos Astronautas, 1758, São José dos Campos, São Paulo 12227-690, Brazil*
[c] *China-Brazil Joint Laboratory for Space Weather, NSSC/INPE, Av. dos Astronautas, 1758, São José dos Campos, São Paulo 12227-690, Brazil*
[d] *State Key Laboratory of Space Weather, National Space Science Center (NSSC), Chinese Academy of Sciences, No. 1, Nanertiao, Zhongguancun, Haidian District, Beijing 100190, China*
[e] *School of Physics and Mathematics, Autonomous University of Nuevo León (UANL), Av. Universidad s/n, Cd. Universitaria, San Nicolás de los Garza, N.L. 66455, Mexico*

Abstract

The turbulent-like process associated with ionospheric instabilities, has been identified as the main nonlinear process that drives the irregularities observed in the different ionospheric regions. In this complementary study, as proposed in the first article of this two-paper series (Fornari et al., 2016), we performed the detrended fluctuation analysis of the equatorial E-F valley region electron density fluctuations measured from an in situ experiment performed over the Brazilian territory. The spectral consistency with the K41 turbulent universality class is analyzed for E-F valley region from the DFA spectra for four electron density time series. A complementary detrended fluctuation analysis for four time series of the F-layer electric field is also presented. Consistent with the results obtained for the F region, the analysis for the E-F valley region also shows a very high spectral variation ($\gg 50\%$). Thus, the spectral analysis performed in both parts of the series suggest that a process such as the homogeneous turbulence K41 ($\beta = -5/3 \pm 2\%$) is inappropriate to describe both the fluctuations of electron density and the electric field associated with the main ionospheric instabilities.
© 2019 COSPAR. Published by Elsevier Ltd. All rights reserved.

Keywords: Equatorial ionospheric plasma irregularities; E-F valley region irregularities; Detrending

1. Introduction

The characteristic features of in situ ionospheric plasma density fluctuation data may provide important information on the structural processes associated with ionospheric irregularities (Muralikrishna et al., 2003). In Part I of this work, Fornari et al. (2016) analyzed in situ F region electric field fluctuation data using the detrended fluctuation analysis (DFA) (Peng et al., 1994) technique to verify the wide variation in the spectral indices reported in earlier rocket experiments based on power spectral density (PSD) method. The results show that the high variability of the spectral indices is not due to the statistical limitation of

* Corresponding author.
E-mail address: neelakshij@gmail.com (J. Neelakshi).

the data, and does not constitute a K41 type of universality class.[1]

As shown, in the first part of this study, PSD although widely used, falls short to characterize turbulence spectra from in situ ionospheric plasma density fluctuation measurements. Many studies have shown that the power spectra of these fluctuations exhibit two or three different spectral exponents indicating the scaling complexity of the process involved (Kelley and Hysell, 1991; Spicher et al., 2014). In general, the spectral indices that have been reported show deviation from the K41 theory but do not elucidate the statistical properties of the energy cascading that is supposed to drive the ionospheric turbulence (Kelley and Hysell, 1991). In this context, the DFA proposed by Peng et al. (1994) is a potential method that could render insights into the statistical properties of the turbulence phenomena.

As envisioned in Part I, here (Part II) the DFA is applied to in situ E-F valley region (hereafter, valley region) data. The valley region is located between the top of the E region and the base of the F region. The valley region, specifically the equatorial ones, hosts a variety of plasma irregularities both during the day, the so-called 150 km echoes (Kudeki and Fawcett, 1993; Rodrigues et al., 2011), and at dusk-nighttime (Chau and Hysell, 2004). This region is still a less explored area of research compared to the F region given the technical limitations in observing it. It can be studied by using powerful incoherent and coherent scatter radar and in situ experiments. Various studies have been reported on the correlation between the valley region irregularities and the equatorial plasma instabilities in the F region:

- Radar observations revealed that (i) the valley region irregularities are often found when the equatorial spread F (ESF) occurred after the sunset and that their spatial structures and temporal variations have resemblance with the ESF, and (ii) the valley region irregularities are a result of the coupling between the unstable equatorial F region and the underlying low-latitude valley and the E region (Vickrey and Kelley, 1982; Vickrey et al., 1984; Patra, 2008; Yokoyama et al., 2005; Li et al., 2011; Kherani et al., 2012).
- Studies based on in situ data found that electric field and gravity waves may play a key role in the generation of these structures (in the valley regions) and that the structures are produced by the generalized Rayleigh-Taylor instability mechanism at the base of the F region (Vickrey et al., 1984; Prakash, 1999; Sinha et al., 1999;

Muralikrishna et al., 2003; Savio Odriozola et al., 2017). Savio Odriozola et al. (2017) reported the presence of wave-like structures in valley region data obtained from an experiment over Brazil, and the same data is used for the present analysis.

In literature, the DFA is applied to study ionospheric irregularities, but we could not find its application to in situ valley region data. This work presents the first instance of application of the DFA to in situ E-F valley region electron density fluctuation data. The paper is organized as follows. Section 2 describes the data along with the electron density vertical profile. The DFA is presented in Section 3 followed by the concluding remarks in Section 4.

2. In situ valley region data

The vertical profile of electron density was obtained from a conical Langmuir probe on-board a two-stage VS-30 Orion sounding rocket experiment launched from an equatorial rocket launching station, Alcântara (2.24° S, 44.4° W, dip latitude 5.5° S), on December 8, 2012, at 19:00 LT, under quiet geomagnetic conditions. During the ~11 min flight, rocket trajectory was in the northnortheast direction towards the magnetic equator, ranging ~384 km horizontally with an apogee covering typical F region altitudes of ~428 km. The conical Langmuir probe worked both in swept and constant bias modes. The probe sensor potential was swept from -1 V to $+2.5$ V linearly in about 1.5 s, during which the electron kinetic temperature was determined from the collected probe current. Then, the potential was maintained at $+2.5$ V (constant bias mode) for 1 s, during which the collected probe current was used to estimate electron density and its fluctuations, in each experiment cycle. This work utilizes the electron density fluctuation data obtained from the conical Langmuir probe. Fig. 1 shows variations in the vertically distributed electron density in the downleg (descent of the rocket) trajectory of the flight.

At the time of launch, the ground-based equipment detected conditions favorable for the generation of plasma bubbles in the F region. Savio Odriozola et al. (2017) reported the presence of several small- and medium-scale plasma irregularities in the valley region (120–300 km) during both ascent and descent, which were more prominent during the descent of the rocket. In the downleg profile, the average electron density observed was around 9×10^9 m^{-3}, equivalent to 1/10th of the E region maximum, and then, it gradually increased after 300 km, where the broad base of F region was detected. These observations are consistent with the work reported by Wakai (1967), which stated that under quiet conditions, the electron concentration in the valley around midnight is about 1/10th of the E region maximum, and width of the valley is very wide compared to the disturbed nights. Prakash et al. (1970) reported observing a deep valley region above

---

[1] The K41 is a theoretical framework for turbulence proposed by Kolmogorov in 1941, which forms a basis to understand the behavior of homogeneous multiplicative energy cascade from turbulent-like processes. Here the turbulent energy spectrum follows a precise power law behavior with index $-5/3 \pm 2\%$ in the inertial range (Frisch, 1995). Therefore, the K41 spectrum represents a universality class for homogeneous turbulent processes.
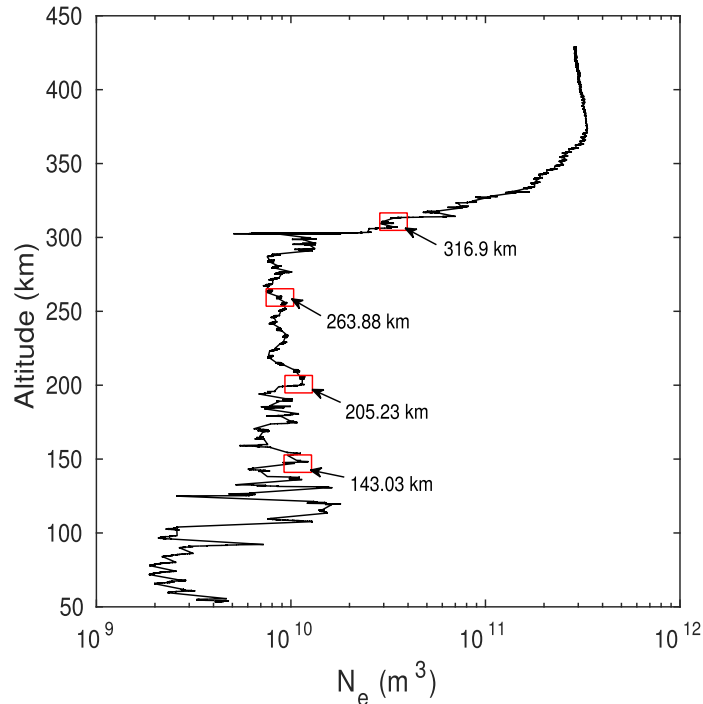
Fig. 1. Vertical profile of electron densities for downleg trajectory. Open boxes represent the chosen heights. (For interpretation of the references to color in this figure legend, the reader is referred to the web version of this article.)

120 km, i.e., 120–140 km, where the electron density fell by two orders of magnitude in their experiment (to a few hundreds per cubic centimeters). Fig. 2 (left panel) shows the selected time series from the downleg electron density profile around average heights of 143, 205, and 263.9 km from the valley region and around 316.9 km, just above the wide base of the F region.

3. Fluctuation analysis, results and interpretation

The DFA proposed by Peng et al. (1994) could render insights into the statistical properties of turbulence phenomena. Originally proposed to detect long-range correlations in DNA sequences and in data influenced by trends, the DFA is widely used in many branches of sciences - medicine, physics, finance and social sciences - to understand the complexity of systems through its scaling exponent that characterizes fractal dynamics of the system (Kantelhardt, 2009; Veronese et al., 2011).

The robustness of DFA can be attributed to some of its interesting features. For instance, Coronado and Carpena (2005) investigated the influence of the length of a time series in quantifying the correlation behavior using techniques like autocorrelation analysis, Hurst exponent, and DFA. The comparison study revealed that the DFA is practically unaffected by the length of time series, contrary to that

observed from the results of Hurst analysis or autocorrelation analysis. Another interesting feature has been reported by Chen et al. (2002) who altered time series by excluding parts of it, stitching the rest and subjecting it to the DFA. The study revealed that even with the removal of 50% of the time series, the scaling behavior of positively correlated signals is unaltered, implying that time series need not be continuous. Heneghan and McDarby (2000) established an equivalence relation between the PSD exponent, β, and the DFA exponent, α, given by $\beta \equiv 2\alpha - 1$. Kiyono (2015) showed that this relationship is valid for the higher order DFA subject to the constraint $0 < \alpha < m + 1$, where m is the order of detrending polynomial in the DFA.

The DFA involves obtaining cumulative sum of the mean subtracted time series followed by dividing it into non-overlapping segments (s), referred to as scales. Further, these segments are detrended using the linear least squares or higher order polynomial (m) method and the variance is calculated. Depending on the detrending order, m, the analysis is referred to as DFAm. Averaging the root mean square over the segments (s) gives the fluctuation function, $F(s)$. Linear fit to the fluctuation function profile yields the scaling exponent α. Implementation procedure can be found in Part I of this paper (Fornari et al., 2016). In this work, four time series of electron density fluc-
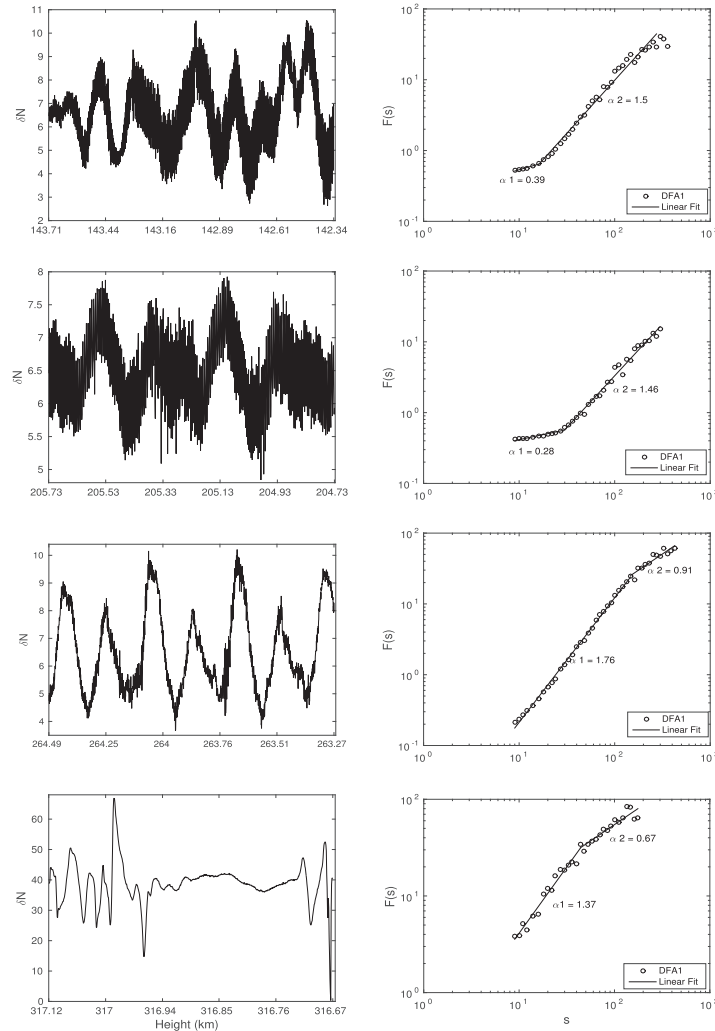
Fig. 2. Left column – E-F valley region time series (δN) of electron density fluctuations obtained from Langmuir probe during the downleg flight for the chosen heights. Right column – Corresponding fluctuation function profile $F(s)$ (open circle) as a function of scales s along with the fit (solid line), i.e., the α exponent.

tuations from the downleg profiles corresponding to the valley region are selected. The selected time series correspond to the mean heights of 143, 205, 263.9, and 316.9 km (please see left panel in Fig. 2).

The selected time series are subjected to DFA. Scales are varied from 10 to $N/4$ with a factor of $2^{\frac{1}{8}}$, where N is the length of time series (Goldberger et al., 2000). The fluctuation function computed from DFA is plotted as a function of scales for all the selected time series (right panel in Fig. 2) on a log-log scale. The profiles of fluctuation function for all the chosen cases exhibit long-range correlation with a crossover. Crossover refers to a change in the scaling

exponent for different scale ranges, and it usually arises due to a change in the correlation properties over different spatial or temporal scales, or from trends in the data. The exponents $\alpha 1$ and $\alpha 2$ are obtained from the linear fit of $F(s)$, where $\alpha 1$ refers to smaller scales and $\alpha 2$ refers to larger scales. Our analysis reveals $\alpha 1$ to be in the range of 0.28 to 1.76 and $\alpha 2$ in the range of 0.67 to 1.5. For mean heights corresponding to 143 and 205 km, we observe $\alpha 1$ is smaller than $\alpha 2$, contrary to the observation for mean heights corresponding to 263.9 and 316.9 km.

In order to be sure that the obtained crossover is intrinsic to the data and not an artifact, we investigated the time

series with higher order DFAs, of the order 1–5. For this investigation, we used the methodology prescribed by Kantelhardt et al. (2001) to identify false crossovers. Artificial crossover exhibits similar characteristic length with identical scaling. Fig. 3 presents the analysis for downleg time series corresponding to the mean height of 143 km with DFA of 1st to 5th order. The crossover exponents are listed in Table 1. It can be observed that as the order of detrending increases, crossover point moves towards larger scales and have different scaling exponents. This investigation confirms that the obtained crossover is an intrinsic property of electron density fluctuation data in the valley region.

The PSD exponent, β, is calculated using the equivalence relationship given above, and the standard deviation σ_m (in %) is determined. The computed DFA exponents in our analysis show a wide range of β from -0.98 to -2.14 with $\sigma_m = 58\%$. Table 2 summarizes the variations in the β exponent obtained from the previous equivalent studies (Rino et al., 1981; Kelley et al., 1982; Muralikrishna and Vieira, 2007; Sinha et al., 2010, 2011) and compares with the present work. All studies reported in Table 2 are based on electron density fluctuation data obtained through rocket experiments. It is observed that the computed

Table 1
DFA1 to DFA5 for downleg time series at ~143.03 km.

DFA order	$\alpha 1$	$\alpha 2$
DFA1	0.39	1.50
DFA2	0.15	1.93
DFA3	0.12	2.08
DFA4	0.10	2.26
DFA5	0.13	2.53

standard deviation $\sigma_m \gg 50\%$, which affirms that the underlying mechanism for instabilities differs from the K41 homogeneous turbulence, given the accepted deviation is $\sigma_m \leq 2\%$ (Frisch, 1995).

We also performed the DFA on in situ electric field fluctuation data from the F region obtained from an earlier experiment conducted on December 18, 1995, at 21:17 LT, under quiet geomagnetic conditions from the same equatorial launching station Alcântara (2.24° S, 44.4° W, dip latitude 5.5° S) (Fornari et al., 2016). The rocket flight traversed through similar altitudes of 200–300 km. This data indicated the presence of a large plasma bubble at an altitude of ~280 km. Fig. 4 presents the time series and the corresponding DFA.
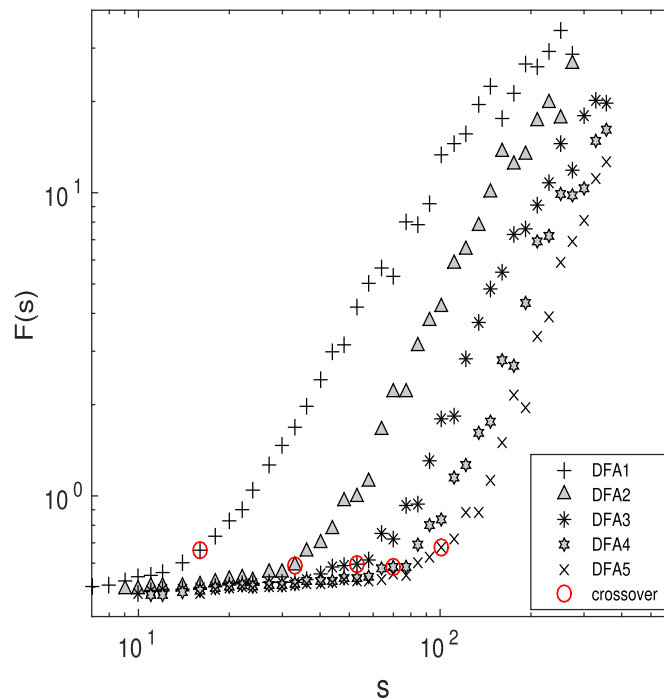

Fig. 3. Fluctuation function profiles for the downleg time series at a mean height of 143 km for polynomials of orders 1–5. Open circles represent the crossover points for the respective detrending order. (For interpretation of the references to color in this figure legend, the reader is referred to the web version of this article.)

Table 2
Comparison of PSD spectral indices (β) found in previous equivalent studies and β obtained here from DFA. All results measured using rockets are related to electronic density measurements during the experiment.

| Date and Time	Spacecraft	Altitude (km)	β range	$\langle \beta \rangle$	σ_m	References
17/07/1979, 12:31:30 UT	Rocket	250 to 370	−1.20 to −3.4	−2.3	110%	Rino et al. (1981)
17/07/1979, 12:31:30 UT	Rocket	250 to 285	−2.00 to −3.4	−2.7	70%	Kelley et al. (1982)
11/12/1985, 00:30 UT	Rocket	210 to 306	−1.34 to −3.3	−2.32	98%	Muralikrishna and Vieira (2007)
31/10/1986, 03:00 UT	Rocket	100 to 220	−1.54 to −3.30	−2.42	88%	Muralikrishna and Vieira (2007)
14/10/1994, 22:55 UT	Rocket	117 to 518	−1.20 to −5.3	−3.25	205%	Muralikrishna and Vieira (2007)
18/12/1995, 00:17 UT	Rocket	240 to 500	−1.11 to −4.90	−3.01	189%	Muralikrishna and Vieira (2007)
15/01/2007, 16:43 UT	Rocket	– to 127	−1.60 to −2.70	−2.15	55%	Sinha et al. (2010)
29/01/2008, 15:49 UT	Rocket	– to 117	−2.00 to −3.50	−2.75	75%	Sinha et al. (2011)
08/12/2012, 22:00 UT	Rocket	– to 317	−0.98 to −2.14	−1.56	58%	This paper
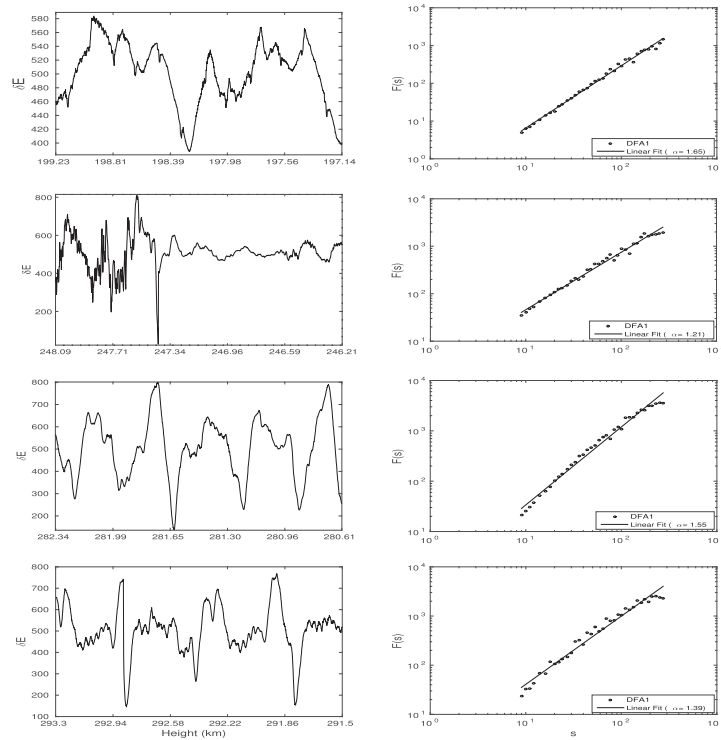
Fig. 4. Left column – F region time series (δE) of electric field fluctuations obtained from electric field probe during the downleg flight. Right column – Corresponding fluctuation function profile $F(s)$ (open circle) as a function of scales s along with the fit (solid line), i.e., the α exponent.

The data from aforementioned experiments is selected for the altitudes of 200–300 km. In the valley region data, small-to-medium scale plasma irregularities (Savio Odriozola et al., 2017) are found, while the F region data shows medium-to-large scale plasma irregularities (Fig. 2 in Muralikrishna et al., 2003). Hence, it will be interesting to compare the scaling exponents of plasma densities around similar altitudes for these two different regions. Fig. 5 shows the scaling exponent plotted as a function of height for the valley region (left panel) and the F region (right panel). For this plot, we have used a single linear fit for valley region data. The shaded horizontal bar in the plot represents the exponent value, $\alpha = 1.33 \pm 2\%$, for the homogeneous turbulence described by the K41 theory. The range of α exponents for the F region is higher than that of the valley region, which may be due to different scaling present in these regions. Wide variations of the scaling exponent from the K41 theory are observed for both regions.
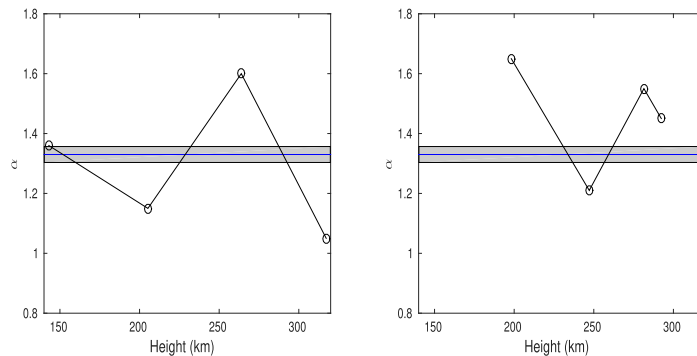
Fig. 5. Mean height vs. DFA exponent α for downleg plasma density fluctuation time series: E-F valley region (left) and F region (right). Solid line in the shaded area indicates the exponent value for homogeneous turbulence (k41 theory) with $\beta = 1.66$, i.e., $\alpha = 1.33$; shaded area shows the range of alpha value deviation $\pm 2\%$.

4. Concluding remarks

In this paper, the complementary in situ E-F valley region irregularities are studied using the DFA. This study is important as studies of the equatorial E-F valley region at nighttime are scarce. Our analysis shows that the E-F valley region electron density fluctuations exhibit long-range correlation with crossovers that are intrinsic to the data for all the chosen altitudes. The F region irregularities obtained from an earlier experiment are also analyzed using the DFA and similar results in terms of long-range correlations are obtained for all the chosen altitudes. The PSD exponent β is computed for the current data and compared with earlier similar experiments. The results show $\sigma_m \gg 50\%$. These observations along with the profile of α with respect to the height indicate that scaling exponents show wide variation from the K41 theory, for both the E-F valley and F regions. This implies that the turbulent-like ionospheric fluctuations as a whole cannot be described by the K41 homogeneous energy cascade theory.

Given this scenario and considering the different mechanisms responsible for the plasma instability along different ionospheric regions, it is necessary to investigate the model for non-homogeneous turbulence that will help to understand the observed high spectral variability. A future study that emerges naturally in this scenario is to look for multifractal signature from the data analyzed here. This investigation is in progress and will be published in an upcoming paper.

Acknowledgement

References

Chau, J.L., Hysell, D.L., 2004. High altitude large-scale plasma waves in the equatorial electrojet at twilight. Ann. Geophys. 22, 4071–4076. https://doi.org/10.5194/angeo-22-4071-2004.

Chen, Z., Ivanov, P.Ch., Hu, K., Stanley, H.E., 2002. Effect of nonstationarities on detrended fluctuation analysis. Phys. Rev. E 65, 041107. https://doi.org/10.1103/PhysRevE.65.041107.

Coronado, A.V., Carpena, P., 2005. Size effects on correlation measures. J. Biol. Phys. 31, 121–133. https://doi.org/10.1007/s10867-005-3126-8.

Fornari, G., Rosa, R., De Meneses Jr., F.C., Muralikrishna, P., 2016. Spectral fluctuation analysis of ionospheric inhomogeneities over Brazilian territory. Part I: equatorial F-region plasma bubbles. Adv. Space Res. 58, 2037–2042. https://doi.org/10.1016/j.asr.2016.03.039.

Frisch, U., 1995. Turbulence: The Legacy of A.N. Kolmogorov. Cambridge University Press, New York.

Goldberger, A.L., Amaral, L.A.N., Glass, L., Hausdorff, J.M., Ivanov, P.Ch., Mark, R.G., Mietus, J.E., Moody, G.B., Peng, Chung-Kang, Stanley, H.E., 2000. PhysioBank, physioToolkit, and physionet: components of a new research resource for complex physiologic signals. Circulation 101, e215–e220. https://doi.org/10.1161/01.CIR.101.23.e215.

Heneghan, C., McDarby, G., 2000. Establishing the relation between detrended fluctuation analysis and power spectral density analysis for stochastic processes. Phys. Rev. E 62, 6103–6110. https://doi.org/10.1103/PhysRevE.62.6103.

Kantelhardt, J.W., Koscielny-Bunde, E., Rego, H.H.A., Havlin, S., Bunde, A., 2001. Detecting long-range correlations with detrended fluctuation analysis. Phys. A 295, 441–454. https://doi.org/10.1016/S0378-4371(01)00144-3.

Kantelhardt, J.W., 2009. Fractal and multifractal time series. In: Meyers, R.A. (Ed.), Encyclopedia of Complexity and Systems Science. Springer, New York, pp. 3754–3779. https://doi.org/10.1007/978-0-387-30440-3_221.

Kelley, M.C., Pfaff, R.F., Baker, K.D., Ulwick, J.C., Livingston, R., Rino, C., Tsunoda, R., 1982. Simultaneous rocket probe and radar measurements of equatorial spread-F-transitional and short wavelength results. J. Geophys. Res. 87, 1575–1588. https://doi.org/10.1029/JA087iA03p01575.

Kelley, M.C., Hysell, D.L., 1991. Equatorial spread-F and neutral atmospheric turbulence: a review and a comparative anatomy. J. Atmos. Terr. Phys. 53, 695–708. https://doi.org/10.1016/0021-9169(91)90122-N.

Kherani, E.A., De Paula, E.R., Cueva, R.Y.C., Camargo, L.A.P., 2012. Observations of nighttime equatorial-upper-E-valley region irregular structures from São Luís radar and their occurrence statistics: a manifestation of vertical coupling between E and F regions. J. Atmos. Terr. Phys. 75–76, 64–70. https://doi.org/10.1016/j.jastp.2011.08.017.

Kiyono, K., 2015. Establishing a direct connection between detrended fluctuation analysis and Fourier analysis. Phys. Rev. E 92, 042925. https://doi.org/10.1103/PhysRevE.92.042925.

Kudeki, E., Fawcett, C.D., 1993. High resolution observations of 150 km echoes at Jicamarca. Geophys. Res. Lett. 20, 1987–1990. https://doi.org/10.1029/93GL01256.

Li, G., Ning, B., Patra, A.K., Wan, W., Hu, L., 2011. Investigation of low-latitude E and valley region irregularities: their relationship to equatorial plasma bubble bifurcation. J. Geophys. Res. 116, A11319. https://doi.org/10.1029/2011JA016895.

Muralikrishna, P., Vieira, L.P., Abdu, M.A., 2003. Electron density and electric field fluctuations associated with developing plasma bubbles. J. Atmos. Sol-Terr. Phys. 65, 1315–1327. https://doi.org/10.1016/j.jastp.2003.08.010.

Muralikrishna, P., Vieira, L.P., 2007. Equatorial F-region irregularities generated by the Rayleigh-Taylor instability mechanism – rocket observations from Brazil. Revista Brasileira de Geofsica 25, 135–149. https://doi.org/10.1590/S0102-261X2007000600016, SciELO Brasil.

Patra, A.K., 2008. Some aspects of electrostatic coupling between E and F regions relevant to plasma irregularities: a review based on recent observations. J. Atmos. Sol,-Terr. Phy. 70, 2159–2171. https://doi.org/10.1016/j.jastp.2008.05.013.

Peng, C.K., Buldyrev, S.V., Havlin, S., Simons, M., Stanley, H.E., Goldberger, A.L., 1994. Mosaic organization of DNA nucleotides. Phys. Rev. E 49, 1685–1689. https://doi.org/10.1103/PhysRevE.49.1685.

Prakash, S., Gupta, S.P., Subbaraya, B.H., 1970. A study of the irregularities in the night time equatorial E-region using a Langmuir probe and plasma noise probe. Planet. Space Sci. 18, 1307–1318. https://doi.org/10.1016/0032-0633(70)90141-8.

Prakash, S., 1999. Production of electric field perturbations by gravity wave winds in the E region suitable for initiating equatorial spread F.

J. Geophys. Res. 104, 10051–10069. https://doi.org/10.1029/1999JA900028.

Rino, C.L., Tsunoda, R.T., Petriceks, J., Livington, R.C., Kelley, M.C., Baker, K.D., 1981. Simultaneous rocket-borne beacon and in situ measurements of equatorial spread F-intermediate wavelength results. J. Geophys. Res. 86, 2411–2420. https://doi.org/10.1029/JA086iA04p02411.

Rodrigues, F.S., De Paula, E.R., Chau, J.L., 2011. On the characteristics of 150-km echoes observed in the Brazilian longitude sector by the 30 MHz São Luís radar. Ann. Geophys. 29, 1905–1916. https://doi.org/10.5194/angeo-29-1905-2011.

Savio Odriozola, S., De Meneses Jr., F.C., Muralikrishna, P., Pimenta, A., Kherani, E., 2017. Rocket in situ observation of equatorial plasma irregularities in the region between E and F layers over Brazil. Ann. Geophys. 35, 413–422. https://doi.org/10.5194/angeo-35-413-2017.

Sinha, H.S.S., Shikha, R., Misra, R.N., 1999. First simultaneous in situ measurement of electron density and electric field fluctuations during spread F in the Indian zone. Geophys. Res. Lett. 26, 1669–1672. https://doi.org/10.1029/1999GL900339.

Sinha, H.S.S., Pandey, R., Misra, R.N., 2010. In situ measurement of nighttime plasma density irregularities over an equatorial station Trivandrum. J. Geophys. Res. 115, A11308. https://doi.org/10.1029/2010JA01561.

Sinha, H.S.S., Pandey, R., Sharma, S., Misra, R.N., 2011. Nighttime E region plasma irregularities over an equatorial station Trivandrum. J. Atmos. Sol-Terr. Phys. 73, 2444–2452. https://doi.org/10.1016/j.jastp.2011.10.005.

Spicher, A., Miloch, W.J., Moen, J.I., 2014. Direct evidence of doubleslope power spectra in the highlatitude ionospheric plasma. Geophys. Res. Lett. 41, 1406–1412. https://doi.org/10.1002/2014GL059214.

Veronese, T.B., Rosa, R.R., Bolzan, M.J.A., Rocha Fernandes, F.C., Sawant, H.S., Karlický, M., 2011. Fluctuation analysis of solar radio bursts associated with geoeffective X-class flares. J. Atmos. Sol-Terr. Phys. 73, 1311–1316. https://doi.org/10.1016/j.jastp.2010.09.030.

Vickrey, J.F., Kelley, M.C., 1982. The effects of a conducting E layer on classical F region crossfield plasma diffusion. J. Geophys. Res. 87, 4461–4468. https://doi.org/10.1029/JA087iA06p04461.

Vickrey, J.F., Kelley, M.C., Pfaff, R., Goldman, S.R., 1984. Lowaltitude image striations associated with bottomside equatorial spread F: observations and theory. J. Geophys. Res. 89, 2955–2961. https://doi.org/10.1029/JA089iA05p02955.

Wakai, N., 1967. Quiet and disturbed structure and variations of the nighttime E region. J. Geophys. Res. 72, 4507–4517. https://doi.org/10.1029/JZ072i017p04507.

Yokoyama, T., Patra, A.K., Fukao, S., Yamamoto, M., 2005. Ionospheric irregularities in the low-latitude valley region observed with the equatorial atmosphere radar. J. Geophys. Res. 110, A10304. https://doi.org/10.1029/2005JA011208.

ANNEX - ARTICLE 2

This annex presents a paper published in the journal Annales Geophysicae. Part of this work was presented in "7th Brazilian meeting on space geophysics and aeronomy".

Structural characterization of the equatorial F region plasma irregularities in the multifractal context

Neelakshi Joshi, Reinaldo R. Rosa, Siomel Savio Odriozola, Esfhan Alam Kherani, Francisco Carlos de Meneses, Stephan Stephany and Polinaya Muralikrishna

National Institute for Space Research

Abstract

This article presents the MFDFA of the F region irregularities. This analysis characterizes intermittent multifractal nature of the irregularities, and is quantified with p model. The results confirm the non–homogeneous nature of the F region irregularities. The usability of the MFDFA in deciphering the morphology of the ionospheric F region irregularities is demonstrated.

Annales
Geophysicae
Open Access
EGU

Structural characterization of the equatorial F region plasma irregularities in the multifractal context

Neelakshi Joshi[1], **Reinaldo R. Rosa**[1], **Siomel Savio**[2,3], **Esfhan Alam Kherani**[2], **Francisco Carlos de Meneses**[2,4], **Stephan Stephany**[1], and **Polinaya Muralikrishna**[2]

[1]Computational Space Physics Group, Lab for Computing and Applied Math (LABAC), National Institute for Space Research (INPE), Av. dos Astronautas, 1758, São José dos Campos, São Paulo 12227-690, Brazil
[2]Aeronomy Division, National Institute for Space Research (INPE), Av. dos Astronautas, 1758, São José dos Campos, São Paulo 12227-690, Brazil
[3]China-Brazil Joint Laboratory for Space Weather, NSSC/INPE, Av. dos Astronautas, 1758, São José dos Campos, São Paulo 12227-690, Brazil
[4]School of Physics and Mathematics, Autonomous University of Nuevo León (UANL), Av. Universidad s/n, Cd. Universitaria, San Nicolás de los Garza, N.L. 66455, Mexico

Correspondence: Neelakshi Joshi (neelakshij@gmail.com)

Abstract. In the emerging ionosphere–space–weather paradigm, investigating the dynamical properties of ionospheric plasma irregularities using advanced computational nonlinear algorithms provide new insights into their turbulent-seeming nature, for instance, the evidence of energy distribution via a multiplicative cascade. In this study, we present a multifractal analysis of the equatorial F region in situ data obtained from two different experiments performed at Alcântara (2.4° S, 44.4° W), Brazil, to explore their scaling structures. The first experiment observed several medium- to large-scale plasma bubbles whereas the second experiment observed vertical uplift of the base of the F region. The multifractal detrended fluctuation analysis and the p-model fit are used to analyze the plasma density fluctuation time series. The result shows the presence of multifractality with degree of multifractality 0.53–0.93 and $0.3 \le p \le 0.4$ cascading probability for the first experiment. Other experimental data also exhibit multifractality with degree of multifractality 0.19–0.27 and $0.42 \le p \le 0.44$ cascading probability in ionospheric plasma irregularities. Our results confirm the nonhomogeneous nature of plasma irregularities and characterize the underlying nonhomogeneous multiplicative cascade hypothesis in the ionospheric medium. Differences in terms of scaling and complexity in the data belonging to different types of phenomena are also addressed.

1 Introduction

Present ionospheric research is transiting towards ionospheric space weather that goes beyond the ground- and space-based communication interruptions to influence decision-making communities on social, economical, and physical infrastructural policies. The enhancements in ionospheric plasma irregularities driven by space weather conditions demand an accurate characterization of the dynamical properties of the electron density and its complex nonlinear variation (Cander, 2019). With instruments operating over a substantial frequency domain, a study of plasma density irregularities provide insight into the underlying physical mechanism and its structural properties (Wernik et al., 2003; Muralikrishna et al., 2003). Energy dissipation is found to be an underlying process for the occurrence of electron density or electric field fluctuations in ionospheric plasma irregularities (Jahn and LaBelle, 1998; Kelley and Hysell, 1991).

Various rocket experiments and numerical simulations have been performed and contributed to our understanding of the generation and development of ionospheric irregular-

ities. Costa and Kelley (1978) showed that the Rayleigh–Taylor instability that initiates in the bottomside equatorial F-region can nonlinearly develop very sharp gradients leading to the formation of steepened structures responsible for the power-law spectra observed by a rocket experiment in Natal, Brazil. Shock waves were observed by numerical simulation performed by Zargham and Seyler (1987) of the generalized Rayleigh–Taylor instability at the bottomside and topside F-region equatorial ionosphere, which was confirmed by rocket and satellite in situ data reported by Kelley et al. (1987). Hysell et al. (1994a, b) proposed a model of plasma steepening, evolving from plasma advection that occurs on the vertical leading edges of plasma depletion wedges, to interpret shock waves detected in the equatorial ionosphere by rockets launched from Kwajalein Atoll. Jahn and LaBelle (1998) measured shock-like structures characterized by the density waveforms at the bottomside and topside F-region of the equatorial ionosphere in a rocket experiment in Alcântara, Brazil.

The spectral analysis, though widely used, falls short in characterizing nonstationary data as stationarity is assumed in the data, which is equivalent to presuming homogeneous turbulence; hence, a more robust method is necessary to analyze nonstationary data (Wernik et al., 2003). In addition, to develop a robust specification and a forecasting model, along with classical morphological, statistical, and spectral studies, a thorough understanding of nonlinearity in ionospheric irregularities is essential (Tanna and Pathak, 2014).

Recent advances in the computational algorithms based on fractal formalism, supplemented with mathematical modeling derived from probabilistic measures, have conclusively substantiated the occurrence of the energy cascading process in turbulent sites in the solar and interplanetary environment as well as in the laboratory using Kolmogorov's formalism as the basis (Grauer et al., 1994; Carbone et al., 1995; Abramenko et al., 2002; Macek, 2007; Wawrzaszek and Macek, 2010; Chian and Muñoz, 2011; Miranda et al., 2013; Wawrzaszek et al., 2019).

Various different approaches had been explored to understand nonlinear characteristics and intermittency in ionospheric irregularities, like structure function analysis (Dyrud et al., 2008; Spicher et al., 2015), fractal and multifractal analysis (Wernik et al., 2003; Alimov et al., 2008; Bolzan et al., 2013; Tanna and Pathak, 2014; Miriyala et al., 2015; Chandrasekhar et al., 2016; Fornari et al., 2016; Sivavaraprasad et al., 2018; Neelakshi et al., 2019), and multispectral optical imaging (Chian et al., 2018).

Structure function analysis performed on ionospheric high-latitude in situ data have revealed the intermittent nature of ionospheric irregularities owing to the large deviations from the Kolmogorov's K41 universal power-law index proposed for neutral fluid turbulence (Spicher et al., 2015).

In all the abovementioned studies, the main feature which gets highlighted is that the power spectra point to large deviations from the homogeneous turbulence described by the Kolmogorov spectrum ($-5/3$). Also, higher-order statistics like structure function analysis confirmed the deviation from the Kolmogorov scales, thus affirming the nonhomogeneity and intermittency in ionospheric irregularities. In the complex scenario of ionospheric turbulence, an important question that arises in the context of this paper is "is nonhomogeneity, which can be characterized by multifractal spectra, the cause for the large deviations from the $-5/3$?" To answer this question, we propose using the multifractal detrended fluctuation analysis (MFDFA) on the equatorial F region plasma irregularities.

A detrended fluctuation analysis (DFA; Peng et al., 1994) has been a proven successful method to find a power law correlation and monofractal scaling in noisy, nonstationary data. The DFA is a robust method as it can handle discontinuous and length-wise short data. In case data are more complex and have intricate scaling, various scaling exponents characterize different parts of the data. To characterize such multiple scaling behavior in the data, Kantelhardt et al. (2002) generalized DFA to MFDFA, and have shown the equivalence to standard partition-function-based multifractal method for stationary data with compact support.

The MFDFA has wide applications in many branches of science, such as medicine (Makowiec, 2011), physics (de Freitas et al., 2016), engineering (Lu et al., 2016), finance (Grech, 2016), and social sciences (Kantelhardt, 2009; Telesca and Lovallo, 2011), to understand the complexity of a system through its scaling exponents that characterize multifractal dynamics of the system. The MFDFA has been applied to study ionospheric scintillation index time series (Tanna and Pathak, 2014; Miriyala et al., 2015) and ionospheric total electron content data (Chandrasekhar et al., 2016; Sivavaraprasad et al., 2018). For example, a wavelet transform was applied to study ionospheric irregularities (Wernik et al., 2003; Bolzan et al., 2013). These analyses identified multifractality and intermittency in nonlinear ionospheric irregularities.

In this work, we explore the low-latitude equatorial F region in situ data obtained from two different experiments and performed from the same rocket launching station. In the first experiment, done on 18 December 1995, the rocket traversed through various medium- to large-scale plasma irregularities during its descent, which were associated with the generalized Rayleigh–Taylor instability (Muralikrishna et al., 2003), whereas in the second experiment, done on 8 December 2012, the base of the F region was moving upward; i.e., pre-reversal enhancement (PRE) of vertical plasma drift was observed (Savio et al., 2016; Savio Odriozola et al., 2017).

In the equatorial ionosphere, the evening PRE is considered as an important seeding mechanism for the post-sunset F region irregularities, as quick and acute uplift of the electric field escalates the rate of growth of the generalized Rayleigh–Taylor instability (Li et al., 2007; Kelley et al., 2009; Abdu et al., 2018). Knowing the relation between these two phenomena, it will be interesting to know the differences in their

scaling behavior and complexity. Investigating these plasma fluctuations may enable the study of the scaling properties of these plasma irregularities, and also knowing various characteristics along with the complexity of the data may provide important inputs to model empirical data. Hence, we apply the MFDFA method to the plasma density fluctuation data obtained from these two different in situ experiments. To corroborate our results, a multifractal spectrum obtained from the MFDFA is fitted with the p-model (Meneveau and Sreenivasan, 1987) based on the generalized two-scale Cantor set. Details on the experiments are given briefly in Sect. 2. Methods are described in Sect. 3. The results of the analyses are discussed in Sect. 4 followed by concluding remarks in Sect. 5.

2 In situ experiments

The equatorial launching station of Brazil is located at Alcântara (2.24° S, 44.4° W, dip latitude 5.5° S). The SONDA III rocket was launched at 21:17 LT on 18 December 1995 under favorable conditions for formation of a plasma bubble. During the $\sim$ 11 min flight, the plane of rocket trajectory was almost orthogonal to the geomagnetic field lines and spanned $\sim$ 589 km distance horizontally with an apogee at altitude $\sim$ 557 km. A rocket-born electric field double probe (EFP) measured electric field fluctuations related to ionospheric plasma irregularities. In the upleg profile (ascent of the rocket), the F region base is clearly observed around 300 km, but without any large-scale depletion or bubble. On the other hand, several plasma bubbles of medium–large scale were observed in the downleg profile (descent of the rocket), around the base of F region and also topside of it, but without any sharp indication of the F region base from an altitude above 240 km. The rocket traversed through regions of different altitudes separated by a few hundred kilometers during upleg and downleg, so this might elucidate the large differences observed in ascent and descent of the rocket (Muralikrishna et al., 2003; Muralikrishna and Abdu, 2006; Muralikrishna and Vieira, 2007). A detailed explanation of in situ experiment and the analysis is found in Muralikrishna et al. (2003), Muralikrishna and Abdu (2006), and Muralikrishna and Vieira (2007).

Some of the key results from the aforementioned (Muralikrishna et al., 2003; Muralikrishna and Abdu, 2006; Muralikrishna and Vieira, 2007) analyses indicate (1) the initiation of a cascade process, owing to the generalized Rayleigh–Taylor instability mechanism near the base of F region that resulted in the development of plasma bubbles or large-scale irregularities, and (2) subsequently, when energy was advected to higher altitudes, smaller-scale irregularities were observed, owing to the cross-field instability mechanism.

From the same rocket launching station, Alcântara, a two-stage VS-30 Orion sounding rocket was launched at 19:00 LT, on 8 December 2012, under favorable conditions

for strong spread F. During the $\sim$ 11 min flight, the rocket trajectory was in the north-northeast direction towards the magnetic equator, ranging $\sim$ 384 km horizontally with an apogee at $\sim$ 428 km. A conical Langmuir probe on board the rocket measured the electron density fluctuations associated with ionospheric plasma irregularities. In this experiment, the F region base was clearly observed in the downleg profile around 300 km, with some small-scale fluctuations in the F region. At the rocket launch time, the ground equipment, a digisonde, was operated from the equatorial station and reported fast uplift of the base of F layer, thus indicating the pre-reversal enhancement of the F region vertical drift (Savio et al., 2016; Savio Odriozola et al., 2017). Further explanation of the in situ experiment and data analysis is found in Savio et al. (2016); Savio Odriozola et al. (2017).

3 Methods

3.1 Multifractal detrended fluctuation analysis

Multifractal detrended fluctuation analysis (Kantelhardt et al., 2002) has been applied to investigate the multifractal properties of ionospheric irregularities in the following way.

To implement the MFDFA, a plasma density time series x_k of length N is considered. A first step is to compute the profile, $Y(i)$, by calculating the cumulative sum by subtracting its mean.

$$Y(i) = \sum_{k=1}^{i} [x_k - \langle x \rangle], \quad i = 1, \dots, N \tag{1}$$

divide the integrated profile into non-overlapping and equidistant N_s segments of s elements, referred to as scales. The length of the series may not be a multiple of all scales and a small part of the profile may be left out. To avoid it, repeat the same procedure over the profile but starting from the endpoint, in the reverse direction.

Now we have a total of $2N_s$ segments. These segments are then detrended using linear least squares. The variance is calculated over all segments:

$$F^2(s, v) = \left(\frac{1}{s} \sum_{i=1}^{s} [Y[(v-1)s+i] - y_v(i)]^2 \right)$$

for each segment v, $v = 1, 2, \dots, N_s$ \hfill (2)

and

$$F^2(s, v) = \left(\frac{1}{s} \sum_{i=1}^{s} [Y[N - (v - N_s)s + i] - y_v(i)]^2 \right)$$

for each segment v, $v = N_s + 1, \dots, 2N_s$. \hfill (3)

$y_v(i)$ is a polynomial fit obtained on a segment v. Now, averaging over all segments, the qth-order fluctuation function is

computed.

$$F_q(s) = \left(\frac{1}{2N_s} \sum_{v=1}^{2N_s} [F^2(s, v)]^{q/2} \right)^{1/q}$$

for $q \neq 0$ $\qquad(4)$

When $q = 0$, logarithmic averaging should be used to calculate fluctuation function.

$$F_0(s) = \exp \left(\frac{1}{2N_s} \sum_{v=1}^{2N_s} [\ln(F^2(s, v))] \right) \qquad(5)$$

Applying a linear fit to the fluctuation function profile on the log-log plot yields the generalized Hurst exponent, $h(q)$, for each moment q as $F_q(s) \propto s^{h(q)}$. The computed generalized Hurst exponent $h(q)$ can be related to the classical multifractal scaling (or mass) exponent as $\tau(q)$ by $\tau(q) = qh(q) - 1$. The multifractal spectrum is calculated using $h(q)$ as follows:

$$\alpha = h(q) + qh'(q) \text{ where } h'(q) = \frac{dh}{dq}, \qquad(6)$$

$$f(\alpha) = q(\alpha - h(q)) + 1, \qquad(7)$$

where α represents the multifractal strength and $f(\alpha)$ represents a set of multifractal dimensions.

3.2 The *p*-model

The *p*-model is proposed by Meneveau and Sreenivasan (1987) to model the energy cascading process in the inertial range of fully developed turbulence for the dissipation field. The *p*-model starts with a coherent structure with an assumed specific energy flux per unit length which then undergoes a binary fragmentation at each cascading step, distributing the energy flux with probabilities p_1 and p_2 among the fragments l_1 and l_2. In this cascading process, n denotes the number of generations. In each generation, the segment size is given by $l_1^m l_2^{n-m}$, where m denotes the number of left-side fragments and $n - m$ represents right-side fragments in a segment (Halsey et al., 1986). An analytical formulation for the generalized two-scale Cantor set is given by

$$\alpha = \frac{\ln(p_1) + (n/m - 1)\ln(p_2)}{\ln(l_1) + (n/m - 1)\ln(l_2)}, \qquad(8)$$

$$f(\alpha) = \frac{(n/m - 1)\ln(n/m - 1) - (n/m)\ln(n/m)}{\ln(l_1) + (n/m - 1)\ln(l_2)}. \qquad(9)$$

This is useful to determine the generalized multifractal dimensions which represent the multifractal spectrum (Halsey et al., 1986).

Based on the generalized two-scale Cantor set, the *p*-model consider equal fragment length ($l_1 = l_2$) and unequal

Table 1. Multifractal analysis measures for the first experiment: the time series at mean heights are listed in the first column, the second column shows the degree of multifractality ($\Delta\alpha$), and the third column gives the measure of asymmetry (A). Columns 4 to 6 list the *p*-model fit parameters, l_1, p_1, and dp respectively.

Mean height	Degree of multifractality	Measure of asymmetry	*p*-model fit parameters		
(km)	$\Delta\alpha$	A	l_1	p_1	dp
264.58	0.53	0.82	0.5	0.364	0.059
270.22	0.82	1.11	0.5	0.340	0.065
292.37	0.93	2.99	0.5	0.339	0.02
324.00	0.72	0.32	0.5	0.315	0.090
358.56	0.52	0.37	0.5	0.360	0.070
429.65	0.28	0.51	0.5	0.399	0.0355

weights ($p_1 \neq p_2$ and $p_1 + p_2 \leq 1$). When $p_1 + p_2 \leq 1$, loss in p parameter given by $dp = 1 - p_1 - p_2$, accounts for the direct energy dissipation in the energy cascading process in the inertial range. The proposed *p*-model claims to display all multifractal properties of one-dimensional section of the dissipation field for fully developed turbulence. The multifractality ceases to exist for $p = 0.5$.

4   Results and interpretation

Six time series of in situ observations of electric field fluctuations from the F region are selected from the first experiment performed on 18 December 1995, corresponding to the mean heights of 264.58, 270.22, 292.37, 324.00, 358.56, and 429.65 km in the downleg. Similarly, from the second experiment performed on 12 December 2012, we selected three time series of electron density fluctuations from the F region, corresponding to the mean heights of 339.94, 348.99, and 400.24 km in the downleg. These time series are subjected to the multifractal analysis. Primarily, the profile is obtained by differencing the time series, i.e., $y = x(i+1) - x(i)$, using the criterion based on the power exponent obtained in the DFA method, prescribed by Ihlen (2012) in Table 2, for biomedical time series, to yield the best results from the MFDFA method. We found the criterion to hold for ionospheric in situ data under study. Scales up to 1/10 of the length of the time series are considered. From the MFDFA, the generalized Hurst exponent $h(q)$, classical multifractal scaling exponent $\tau(q)$ and multifractal spectrum α, and $f(\alpha)$ are obtained. We show a comprehensive analysis for only one time series from each of the two experiments (Figs. 1 and 2). For the remaining time series, we show only the multifractal spectrum along with its respective time series (Figs. 3 and 4), but we report the analysis of both experiments in Tables 1 and 2, respectively.

In the MFDFA, fluctuation function $Fq(s)$ is obtained by computing the qth-order local root mean square (RMS) for multiple segment size, i.e., for scales s. A segment may
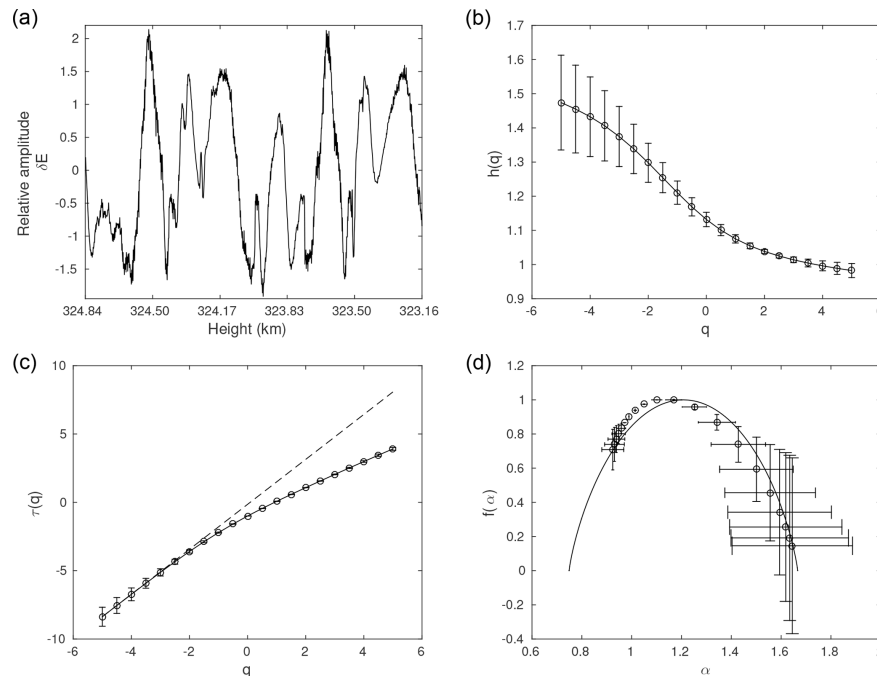
Figure 1. Comprehensive MFDFA for the first experiment: panel **(a)** shows the time series at mean height 324.00 km and panel **(b)** shows the $h(q)$ vs. q profile. Panel **(c)** shows $\tau(q)$ vs. q profile along with a dashed line which represents a linear relationship between $\tau(q)$ and q, and panel **(d)** shows the multifractal spectrum fitted with the p-model (continuous line).

Table 2. Multifractal analysis measures for the second experiment: For the time series at mean heights listed in the first column, the second column shows degree of multifractality ($\Delta\alpha$), the third column gives measure of asymmetry (A). Columns 4 to 6 lists the p-model fit parameters, l_1, p_1, dp respectively.

< height >	degree of multifractality	measure of asymmetry	p-model fit parameters		
(km)	$\Delta\alpha$	A	l_1	p_1	dp
339.94	0.27	1.34	0.5	0.4230	0.012
348.99	0.22	1.72	0.5	0.4300	0.006
400.24	0.19	0.94	0.5	0.4335	0.01

contain smaller to larger fluctuations. Rapid variation in fluctuations influence overall RMS for smaller-scale sizes, whereas slow variation in fluctuations influence overall RMS for larger-scale sizes. Negative q values characterize smaller fluctuations and positive q values characterize larger fluctuations in a segment. When $q = 0$, it behaves neutrally. $h(q)$ has dependence on q. To outline, for a multifractal time series $h(q)$ monotonically decreases with q, and $\tau(q)$ shows nonlinear dependence on q. With $q = 0$ as a center point, let us inspect how $h(q)$ varies with respect to negative and positive

values of q. If the time series is influenced by smaller fluctuations, then variation of $h(q)$ for negative q will be faster, i.e., a steeper slope can be observed with respect to negative q and vice versa (Kantelhardt et al., 2002; Ihlen, 2012).

The multifractal spectrum illustrates how segments with small and large fluctuations deviate from the average fractal structure. The shape and width of the multifractal spectrum are also important measures to quantify the nature of multifractality present in the data. For $f(\alpha) = 1$, the corresponding value of α, known as α_0, divides the spectrum into left and right sides. A shape of the spectrum (the difference between the left and right sides of the spectrum) can be quantified by measure of asymmetry, A, given by

$$A = \frac{\alpha_0 - \alpha_{\min}}{\alpha_{\max} - \alpha_0}. \tag{10}$$

When $A = 1$, the multifractal spectrum is symmetric in the sense that the time series is influenced by both larger as well as smaller fluctuations. When $A > 1$, the spectrum is left-skewed, which implies that the time series is more influenced by the larger fluctuations. When $A < 1$, the spectrum is right-skewed, which implies that the time series is more influenced by smaller fluctuations.
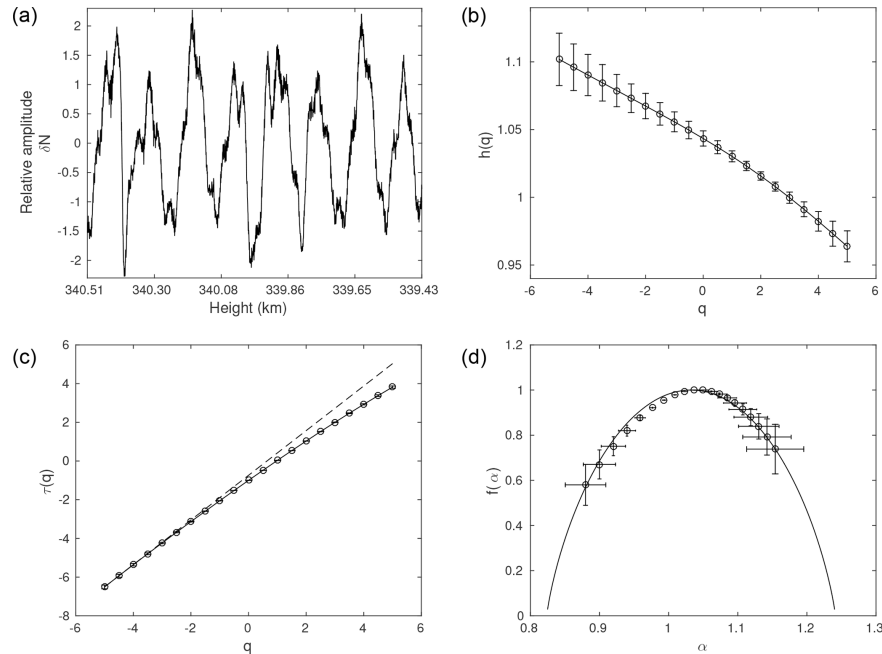
Figure 2. Comprehensive MFDFA for the second experiment: panel **(a)** shows the time series at mean height 339.94 km and panel **(b)** shows the $h(q)$ vs. q profile. Panel **(c)** shows the $\tau(q)$ vs. q profile along with a dashed line which represents a linear relationship between $\tau(q)$ and q, and panel **(d)** shows the multifractal spectrum fitted with the p-model (continuous line).

A width of the spectrum can be quantified by $\Delta\alpha$, which is the difference between maximum and minimum dimension.

$$\Delta\alpha = \alpha_{max} - \alpha_{min} \qquad (11)$$

The width of the spectrum infers the degree of multifractality and complexity of the data. It represents the deviation from the average fractal structure and directly relates to the parameters corresponding to the multiplicative cascade process. A larger (smaller) value of $\Delta\alpha$ infers stronger (weaker) multifractality in the data.

The multifractal spectrum reflects the characteristics of the $h(q)$ profile. In the spectrum, contrary to the $h(q)$ profile, the left side is characterized by positive values of q, and the right side is characterized by negative values of q. When the $h(q)$ profile shows the steeper variations on the left side, i.e., for negative q's, the right side of the spectrum shows faster variation compared to its left side.

Figure 1 shows a detailed multifractal analysis of a time series from the first experiment, corresponding to the mean height of 324.00 km (a). The profile of $h(q)$ as a function of q is shown in Fig. 1b, and of $\tau(q)$ in 1c. The corresponding multifractal spectrum is shown in Fig. 1d. The spectrum is right-skewed, indicating the influence of the negative values of q on the data. It is evident as well from the $h(q)$ pro-

file that the variation of $h(q)$ for negative q is observed to be comparatively steep. The plot for $\tau(q)$ versus q shows marked deviation from the linearity, asserting the presence of the multifractality in the time series for the chosen height. In addition to the derived inferences from the visual analysis of the multifractal spectrum reported above, multifractal measures, $\Delta\alpha$, and A can be quantified (Eqs. 11 and 10). Measure $A = 0.32$ quantifies the skewness while $\Delta\alpha = 0.72$ infers the strength of multifractality. These two measures are listed in Table 1. Lastly, the multifractal spectrum is fitted with the p-model (shown with a continuous line), where the fragment lengths are equal; i.e., $l_1 = l_2 = 0.5$ and the weights, p_1 and p_2, are varied such that $p_1 + p_2 \leq 1$. Nevertheless, the loss in p parameter had to be accounted for to obtain an optimal fit. The loss factor, dp, signifies nonconservative energy distribution, i.e., a dissipative energy cascading process in the inertial range. We have obtained a dissipative factor of 0.090, with $p_1 = 0.315$. The p-model fit parameters are listed in Table 1.

Similar to Fig. 1, Fig. 2 shows a detailed multifractal analysis of a time series from the second experiment, corresponding to the mean height of 339.94 km (a). The profile of $h(q)$ as a function of q is shown in Fig. 2b, and of $\tau(q)$ in Fig. 2c. The corresponding multifractal spectrum is shown in Fig. 2d.
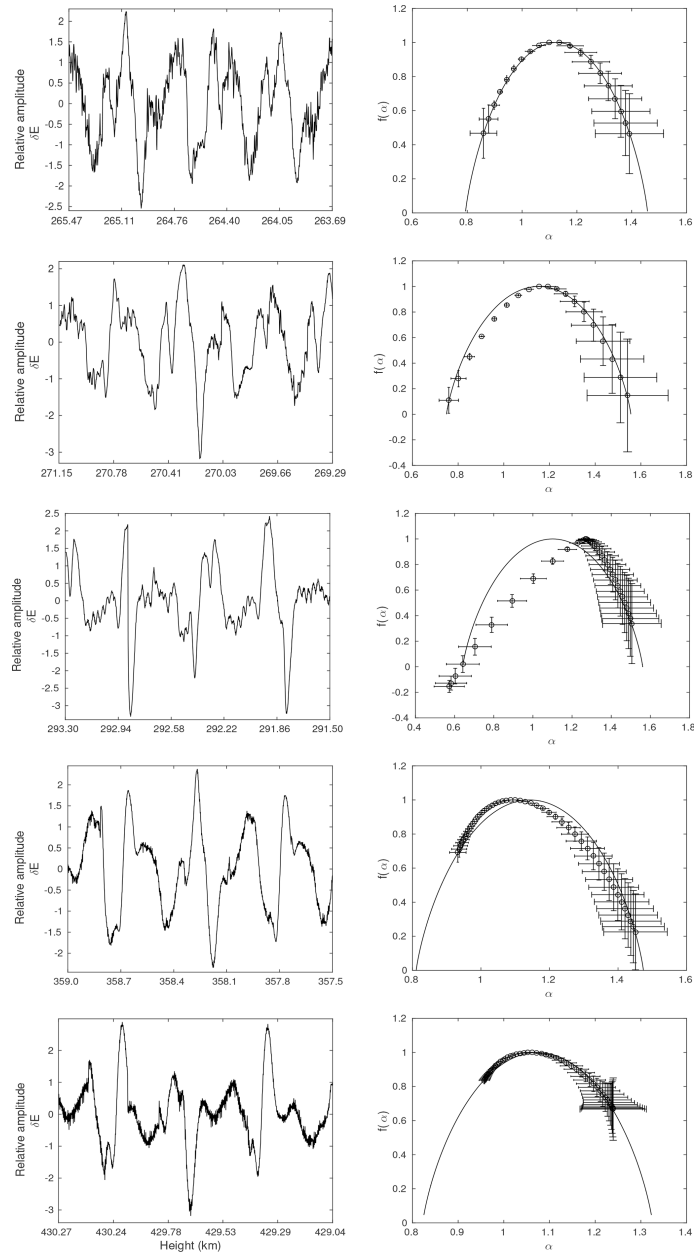
Figure 3. MFDFA for the first experiment: the time series and its corresponding multifractal spectrum with the *p*-model fit (continuous line) for the mean heights of 264.58, 270.22, 292.37, 358.56, and 429.65 km, from top to bottom, respectively.
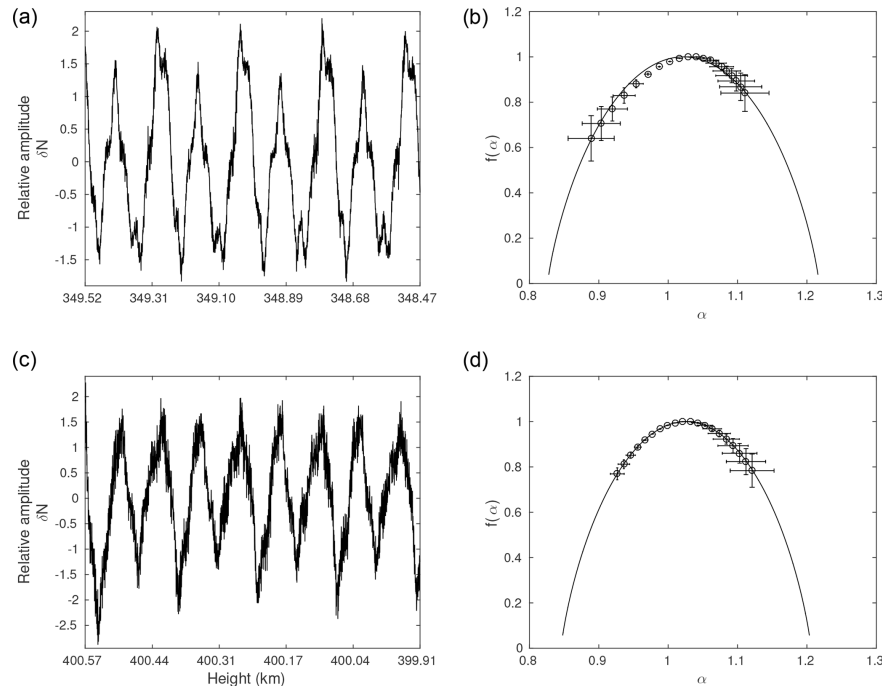
Figure 4. MFDFA for the second experiment: panels **(a, b)** show the multifractal analysis of the time series at mean height 348.99 km and panels **(c, d)** show the multifractal analysis of the time series at mean height 400.24 km. Panels **(a, c)** show the time series for given mean height and panels **(b, d)** show the multifractal spectrum fitted with the p-model (continuous line).

The spectrum is left-skewed, indicating the influence of the positive values of q on the data. The variation of $h(q)$ for positive q is observed to be comparatively steep. The plot for $\tau(q)$ versus q show a marked deviation from the linearity, asserting the presence of the multifractality in the time series for the chosen height. The multifractal measures computed, $A = 1.34$ and $\Delta\alpha = 0.27$, and listed in Table 2. Lastly, the multifractal spectrum is fitted with the p-model (shown with a continuous line). We have obtained a dissipative factor of 0.012, with $p_1 = 0.423$. The p-model fit parameters are listed in Table 2.

It is seen from the above description that the multifractal spectrum is sufficient to assess the multifractal nature; henceforth we show the time series and the corresponding multifractal spectrum for the remaining chosen heights.

Figure 3 shows the time series selected from the first experiment in the left panels and the corresponding multifractal spectrum in the right panels:

– For the time series corresponding to the mean height of 264.58 km, the multifractal spectrum is slightly right-skewed, which can be inferred from measure $A = 0.82$. It indicates the influence of negative moments, q, which characterizes the influence of smaller fluctuations than

the average. The degree of multifractality is $\Delta\alpha = 0.53$. The optimal p-model fit is obtained with parameters $p_1 = 0.364$ and $dp = 0.059$.

– For the time series corresponding to the mean height of 270.22 km, the multifractal spectrum is slightly left-skewed, which can be inferred from measure $A = 1.11$. It indicates the influence of positive moments, q, which characterize intense larger fluctuations than the average. The degree of multifractality is $\Delta\alpha = 0.82$. The optimal p-model fit is obtained with parameters $p_1 = 0.34$ and $dp = 0.065$.

– For the time series corresponding to the mean height of 292.37 km, the multifractal spectrum is left-skewed, reflected in measure $A = 2.99$. It indicates the influence of positive moments, q, which characterize intense larger fluctuations than the average. The degree of multifractality is $\Delta\alpha = 0.93$. The optimal p-model fit is obtained with parameters $p_1 = 0.339$ and $dp = 0.02$. We could fit the spectrum corresponding to positive values of q.

– For the time series corresponding to the mean height of 358.56 km, the multifractal spectrum is right-skewed,
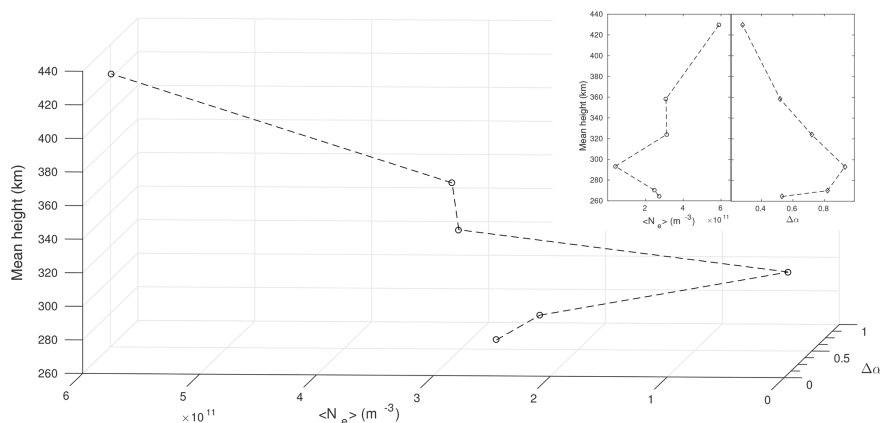
Figure 5. Variation of the mean density and the degree of multifractality with the mean height for the six selected time series from the first experiment in a 3-D plane. These variations are shown in a 2-D plane of the mean density (main image) and the degree of multifractality (inset).

reflected in measure $A = 0.37$. It indicates the influence of negative moments, q, which characterize the influence of smaller fluctuations than the average. The degree of multifractality is $\Delta\alpha = 0.52$. The optimal p-model fit is obtained with parameters $p_1 = 0.36$ and $dp = 0.07$.

– For the time series corresponding to the mean height of 429.65 km, the multifractal spectrum is right-skewed, also reflected in measure $A = 0.51$. It indicates the influence of negative moments, q, which characterize the influence of smaller fluctuations than the average. Degree of multifractality is $\Delta\alpha = 0.28$. The optimal p-model fit is obtained with parameters $p_1 = 0.399$ and $dp = 0.0355$.

Figure 4 shows the time series selected from the second experiment in Fig 4a and c and the corresponding multifractal spectrum in Fig 4b and d:

– For the time series corresponding to the mean height of 348.99 km, the multifractal spectrum is left-skewed, reflected in measure $A = 1.72$. It indicates the influence of positive moments, q, which characterize intense larger fluctuations than the average. The degree of multifractality is $\Delta\alpha = 0.22$. The optimal p-model fit is obtained with parameters $p_1 = 0.43$ and $dp = 0.006$.

– For the time series corresponding to the mean height of 400.24 km, the multifractal spectrum is almost symmetrical. This is reflected in measure $A = 0.94$, which is very close to 1. It indicates that both negative and positive moments of q characterize the influence of larger and smaller fluctuations than the average almost equally. The degree of multifractality is $\Delta\alpha = 0.19$.

The optimal p-model fit is obtained with parameters $p_1 = 0.4335$ and $dp = 0.01$.

Figure 5 shows a variation of mean density and multifractal width, $\Delta\alpha$, with mean heights for the selected six time series on a three-dimensional plane. The presence of a plasma bubble characterized by large-scale irregularities, which in turn is reflected in the low density, is observed around a mean height of 292.37 km. Contrarily, stronger multifractality is observed at this height. This inverse variation is in agreement with the turbulent-seeming multiplicative cascade process. On the other hand, as the rocket traversed higher altitudes, the mean density increased while the multifractality became weaker. This suggests that the cascading process resulted in smaller-scale irregularities due to dissipating energy. Two-dimensional plots showing the variation of mean density and $\Delta\alpha$ with mean heights are shown in Fig. 5.

5 Concluding remarks

In this work, we investigate the in situ F region electric field and electron density measurements obtained from the two experiments carried out near the equatorial sites in Brazil using the MFDFA to understand the complexity in the data and to identify the signature of multiplicative energy cascades in irregularities.

In all the time series, we obtained $0.9 < h(q) < 1.5$, which indicates a long-range correlation with persistent temporal fluctuations. In addition, we note that the $h(q)$ profile monotonically decreases with respect to q and that $\tau(q)$ shows deviation from the linearity, indicating the presence of the multifractality in all time series. Measures of multifractal spectra, A, have shown the presence of structures (both smaller

or larger) in the fluctuations, and $\Delta\alpha$ has shown weaker to stronger multifractality. The multifractal spectra were fitted with the p-model and we found weight parameter p_1 to be different from 0.5, which confirms the multifractality present in the data. The accounting nonzero dissipation factor suggests that energy distribution across the eddies is nonuniform. Our results show the nonhomogenous and intermittent nature of ionospheric irregularities are consistent with previous findings.

In the second experiment, we considered a total of six time series, out of which three time series exhibited a monofractal nature, and the remaining three showed weaker multifractality and are presented here. $\Delta\alpha$ and skewness are found to be smaller compared to the first experiment. The result for a mean height of 348.99 km is different than for the other two heights and shows evidence of some different kind of physical mechanism, which can be described by the multiplicative cascade process. Though time series are characterized by weaker multifractality, these data have fractal behavior with long-range correlation. However, we argue that more detailed study is required to reach any definite conclusion on the turbulent-seeming mechanism driving the ionospheric irregular structures.

Finally, we intend to test the potential of this algorithm in deciphering the morphology of the cascading phenomena. For this, we choose the first experiment where the rocket intercepted a plasma bubble. Muralikrishna et al. (2003) reported the presence of predominant sharp peaks in the power spectra over a wide range of heights, and they attribute these to a developing plasma bubble that subsequently dissipated energy, reaching an equilibrium which is evidenced by the absence of peaks. Our multifractal analysis has captured this sequence of events.

The presence of a plasma bubble characterized by large-scale irregularities, which in turn is reflected in the low density, is observed around a mean height of 292.37 km. Contrarily, stronger multifractality is observed at this height. This inverse variation is in agreement with the turbulent-seeming multiplicative cascade process. On the other hand, as the rocket traversed higher altitudes, the mean density increased while the multifractality became weaker. This suggests that the cascading process resulted in smaller-scale irregularities by dissipating energy.

We conclude at this point where we have presented the schematic hypothesis based on the multifractal analysis of plasma irregularities in the ionospheric F region.

Author contributions. All authors have contributed to the analysis and development of the manuscript.

References

Abdu, M. A., Nogueira, P. A. B., Santos, A. M., de Souza, J. R., Batista, I. S., and Sobral, J. H. A.: Impact of disturbance electric fields in the evening on prereversal vertical drift and spread F developments in the equatorial ionosphere, Ann. Geophys., 36, 609–620, https://doi.org/10.5194/angeo-36-609-2018, 2018.

Abramenko, V. I., Yurchyshyn, V. B., Wang, H., Spirock, T. J., and Goode, P. R.: Scaling behavior of structure functions of the longitudinal magnetic field in active regions of the Sun, Astrophys. J., 577, 487–495, https://doi.org/10.1086/342169, 2002.

Alimov, V. A., Vybornov, F. I., and Rakhlin, A. V.: Multifractal Structure of Intermittency in a Developed Ionospheric Turbulence, Radiophys. Quantum. El., 51, 438, https://doi.org/10.1007/s11141-008-9044-4, 2008.

Bolzan, M. J. A., Tardelli, A., Pillat, V. G., Fagundes, P. R., and Rosa, R. R.: Multifractal analysis of vertical total electron content (VTEC) at equatorial region and low latitude, during low solar activity, Ann. Geophys., 31, 127–133, https://doi.org/10.5194/angeo-31-127-2013, 2013.

Cander, L. R.: Ionospheric Space Weather Targets, in: Ionospheric Space Weather, Springer International Publishing, 245–264, https://doi.org/10.1007/978-3-319-99331-7_9, 2019.

Carbone, V., Bruno, R., and Veltri, P.: Scaling laws in the solar wind turbulence, in: Small-Scale Structures in Three-Dimensional Hydrodynamic and Magnetohydrodynamic Turbulence, edited by: Meneguzzi, M., Pouquet, A., and Sulem, P. L., Lect. Notes Phys., 462, 153–158, https://doi.org/10.1007/BFb0102411, 1995.

Chandrasekhar, E., Prabhudesai, S. S., Seemala, G. K., and Shenvi, N.: Multifractal detrended fluctuation analysis of ionospheric total electron content data during solar minimum and maximum, J. Atmos. Sol.-Terr. Phy., 149, 31–39, https://doi.org/10.1016/j.jastp.2016.09.007, 2016.

Chian, A. C.-L. and Muñoz, P. R.: Detection of current sheets and magnetic reconnections at the turbulent leading edge of an interplanetary coronal mass ejection, Astrophys. J. Lett., 733, L34, https://doi.org/10.1088/2041-8205/733/2/l34, 2011.

Chian, A. C.-L., Abalde, J. R., Miranda, R. A., Borotto, F. A., Hysell, D. L., Rempel, E. L., and Ruffolo, D.: Multi-spectral optical imaging of the spatiotemporal dynamics of ionospheric intermittent turbulence, Sci. Rep., 8, 10568, doi:10.1038/s41598-018-28780-5, 2018.

Costa, E. and Kelley, M. C.: On the role of steepened structures and drift waves in equatorial spread F, J. Geophys. Res., 83, 4359–4364, https://doi.org/10.1029/JA083iA09p04359, 1978.

de Freitas, D. B., Nepomuceno, M. M. F., de Moraes Junior, P. R. V., Lopes, C. E. F., Das Chagas, M. L., Bravo, J. P., Costa, A. D., Canto Martins, B. L., De Medeiros, J. R., and Leão, I. C.: New suns in the cosmos, III. Multifractal signature analysis, Astrophys. J., 831, 87, https://doi.org/10.3847/0004-637x/831/1/87, 2016.

Dyrud, L., Krane, B., Oppenheim, M., P/ˇecseli, H. L., Trulsen, J., and Wernik, A. W.: Structure functions and intermittency in ionospheric plasma turbulence, Nonlinear Proc. Geoph., 15, 847–862, 2008.

Fornari, G., Rosa, R., De Meneses, F. C., and Muralikrishna, P.: Spectral fluctuation analysis of ionospheric inhomogeneities over Brazilian territory, Part I: Equatorial F-region plasma bubbles, Adv. Space Res., 58, 2037–2042, https://doi.org/10.1016/j.asr.2016.03.039, 2016.

Grauer, R., Krug, J., and Marliani, C.: Scaling of high-order structure functions in magnetohydrodynamic turbulence, Phys. Lett. A, 195, 335–338, https://doi.org/10.1016/0375-9601(94)90038-8, 1994.

Grech, D.: Alternative measure of multifractal content and its application in finance, Chaos. Soliton. Fract., 88, 183–195, https://doi.org/10.1016/j.chaos.2016.02.017, 2016

Halsey, T., Jensen, M., Kadanoff, L., Procaccial, I., and Shraiman, B.: Fractal measures and their singularities: The characterization of strange sets, Phys. Rev. A, 33, 1141–1151, 1986.

Hysell, D. L., Kelley, M. C., Swartz, W. E., Pfaff, R. F., and Swenson, C. M.: Steepened structures in equatorial spread F: 1. New observations, J. Geophys. Res., 99, 8827–8840, https://doi.org/10.1029/93JA02961, 1994.

Hysell, D. L., Seyler, C. E., and Kelley, M. C.: Steepened structures in equatorial spread F: 2. Theory, J. Geophys. Res., 99, 8841–8850, https://doi.org/10.1029/93JA02960, 1994.

Ihlen Espen: Introduction to Multifractal Detrended Fluctuation Analysis in Matlab, Front. Physiol., 3, 141, https://doi.org/10.3389/fphys.2012.00141, 2012.

Biblioteca, National Institute for Space Research (INPE): Structural characterization of the equatorial F region plasma irregularities in the multifractal context, available at: http://urlib.net/rep/8JMKD3MGP3W34R/803U8PQA8 last access: 17 October 2019.

Jahn, J. M. and LaBelle, J.: Rocket measurements of high-altitude spread F irregularities at the magnetic dip equator, J. Geophys. Res.-Space, 103, 23427–23441, https://doi.org/10.1029/97JA02636, 1998.

Kantelhardt, J., Zschiegner, S., Koscielny-Bunde, E., Havlin, S., Bunde, A., and Stanley, H.: Multifractal detrended fluctuation analysis of nonstationary time series, Physica A, 316, 87–114, 2002.

Kantelhardt, J. W. and Meyers, R. A. (Eds.): Fractal and multifractal time series, Encyclopedia of complexity and systems science, Springer New York, 3754–3779, https://doi.org/10.1007/978-0-387-30440-3_221, 2009.

Kelley, M. C., Seyler, C. E., and Zargham, S.: Collisional interchange instability: 2. A comparison of the numerical simulations with the in situ experimental data, J. Geophys. Res., 92, 10089–10094, https://doi.org/10.1029/JA092iA09p10089, 1987.

Kelley, M. C. and Hysell, D. L.: Equatorial Spread-F and neutral atmospheric turbulence: A review and a comparative anatomy, J. Atmos. Terr. Phys., 53, 695–708 https://doi.org/10.1016/0021-9169(91)90122-N, 1991.

Kelley, M. C., Ilma, R. R., and Crowley, G.: On the origin of pre-reversal enhancement of the zonal equatorial electric field, Ann. Geophys., 27, 2053–2056, https://doi.org/10.5194/angeo-27-2053-2009, 2009.

Li, G., Ning, B., Liu, L., Ren, Z., Lei, J., and Su, S.-Y.: The correlation of longitudinal/seasonal variations of evening equatorial pre-reversal drift and of plasma bubbles, Ann. Geophys., 25, 2571–2578, https://doi.org/10.5194/angeo-25-2571-2007, 2007.

Lu, X., Zhao, H., Lin, H., and Wu, Q.: Multifractal Analysis for Soft Fault Feature Extraction of Nonlinear Analog Circuits, Math. Probl. Eng., 2016, 7305702, https://doi.org/10.1155/2016/7305702, 2016.

Macek, W. M.: Multifractality and intermittency in the solar wind, Nonlinear Proc. Geoph., 14, 695–700, 2007.

Makowiec, D., Rynkiewicz, A., Gałaska, R., Wdowczyk-Szulc, J., and Żarczyńska-Buchowiecka, M.: Reading multifractal spectra: Aging by multifractal analysis of heart rate, Europhys. Lett., 94, 68005, https://doi.org/10.1209/0295-5075/94/68005, 2011.

Meneveau, C. and Sreenivasan, K.: Simple multifractal cascade model for fully developed turbulence, Phys. Rev. Lett., 59, 1424–1427, 1987.

Miranda, R. A., Chian, A. C.-L., and Rempel, E. L.: Universal scaling laws for fully-developed magnetic field turbulence near and

far upstream of the Earth's bow shock, Adv. Space Res., 51, 1893, https://doi.org/10.1016/j.asr.2012.03.007, 2013.

Miriyala, S., Koppireddi, P. R., and Chanamallu, S. R.: Robust detection of ionospheric scintillations using MF-DFA technique, Earth Planets Space, 67, 98, https://doi.org/10.1186/s40623-015-0268-1, 2015.

Muralikrishna, P., Vieira, L. P., and Abdu, M. A.: Electron density and electric field fluctuations associated with developing plasma bubbles, J. Atmos. Sol.-Terr. Phy., 65, 1315–1327, https://doi.org/10.1016/j.jastp.2003.08.010, 2003.

Muralikrishna, P. and Abdu, M. A.: Rocket measurements of ionospheric electron density from Brazil in the last two decades, Adv. Space Res., 37, 1091–1096, https://doi.org/10.1016/j.asr.2006.02.006, 2006.

Muralikrishna, P. and Vieira, L. P.: Equatorial F-region irregularities generated by the Rayleigh-Taylor instability mechanism: rocket observations from Brazil, Rev. Bras. Geof., 25, 6, https://doi.org/10.1590/S0102-261X2007000600016, 2007.

Neelakshi, J., Rosa, R. R., Savio, S., De Meneses, F. C., Stephany, S., Fornari, G., and Muralikrishna, P.: Spectral fluctuation analysis of ionospheric inhomogeneities over Brazilian territory, Part II: E-F valley region plasma instabilities, Adv. Space Res., 64, 1592–1599, https://doi.org/10.1016/j.asr.2019.07.015, 2019.

Peng, C. K., Buldyrev, S. V., Havlin, S., Simons, M., Stanley, H. E., and Goldberger, A. L.: Mosaic organization of DNA nucleotides, Phys. Rev. E, 49, 1685–1689, https://doi.org/10.1103/PhysRevE.49.1685, 1994.

Savio, S., Muralikrishna, P., Batista, I. S., and de Meneses, F. C.: Wave structures observed in the equatorial F-region plasma density and temperature during the sunset period, Adv. Space Res., 58, 2043–2051, https://doi.org/10.1016/j.asr.2016.07.026, 2016.

Savio Odriozola, S., de Meneses Jr., F. C., Muralikrishna, P., Pimenta, A. A., and Kherani, E. A.: Rocket in situ observation of equatorial plasma irregularities in the region between E and F layers over Brazil, Ann. Geophys., 35, 413–422, https://doi.org/10.5194/angeo-35-413-2017, 2017.

Savio, S., Sousasantos, J., Pimenta, A. A., Yang, G., Kherani, E. A., Wang, C., and Liu, Z.: Quasiperiodic rising structures in the E-F valley region below the equatorial plasma bubble: A numerical study, J. Geophys. Res.-Space, 124, 7247–7255, https://doi.org/10.1029/2019JA026620, 2019.

Seuront, L., Schmitt, F., Lagadeuc, Y., Schertzer, D., and Lovejoy, S.: Universal multifractal analysis as a tool to characterize multiscale intermittent patterns: example of phytoplankton distribution in turbulent coastal waters, J. Plankton Res., 21, 877–922, 1999.

Sivavaraprasad, G., Otsuka, Y., Tripathi, N. K., Chowdhary, V. R., Ratnam, D. V., and Khan, M. A.: Spatial and temporal characteristics of ionospheric total electron content over Indian equatorial and low-latitude GNSS stations, Conference on Signal Processing And Communication Engineering Systems (SPACES), Vijayawada, 105–108, https://doi.org/10.1109/SPACES.2018.8316326, 2018.

Spicher, A., Miloch, W. J., Clausen, L. B. N., and Moen, J. I.: Plasma turbulence and coherent structures in the polar cap observed by the ICI-2 sounding rocket, J. Geophys. Res.-Space, 120, 10959–10978, https://doi.org/10.1002/2015JA021634, 2015.

Tanna, H. J. and Pathak, K. N.: Multifractal behaviour of the ionospheric scintillation index time series over an Indian low latitude station Surat, J. Atmos. Sol.-Terr. Phy., 109, 66–74, https://doi.org/10.1016/j.jastp.2014.01.009, 2014.

Telesca, L. and Lovallo, M.: Revealing competitive behaviours in music by means of the multifractal detrended fluctuation analysis: application to Bach's Sinfonias, P. Roy. Soc. A-Math. Phy., 467, 3022–3032, https://doi.org/10.1098/rspa.2011.0118, 2011.

Wawrzaszek, A. and Macek, W. M.: Observation of the multifractal spectrum in solar wind turbulence by Ulysses at high latitudes, J. Geophys. Res., 115, A07104, doi:10.1029/2009JA015176, 2010.

Wawrzaszek, A., Echim, M. and Bruno, R.: Multifractal Analysis of Heliospheric Magnetic Field Fluctuations Observed by Ulysses, Astrophys. J., 876, 153, https://doi.org/10.3847/1538-4357/ab1750, 2019.

Wernik, A. W., Secan, J. A., and Fremouw, E. J.: Ionospheric irregularities and scintillation, Adv. Space Res., 31, 971–981, https://doi.org/10.1016/S0273-1177(02)00795-0, 2003.

Zargham, S. and Seyler, C. E.: Collisional interchange instability: 1. Numerical simulations of intermediate-scale irregularities, J. Geophys. Res., 92, 10073–10088, https://doi.org/10.1029/JA092iA09p10073, 1987.